

Mechanical behaviour of tools for shearing Ultra High-Strength Steels: influence of the microstructure on fracture and fatigue micro-mechanisms of tool steels and evaluation of micro-mechanical damage in tools

Ingrid Picas

PhD Thesis

Universitat Politècnica de Catalunya



Departament de Ciència dels
Materials i Enginyeria Metal·lúrgica

UNIVERSITAT POLITÈCNICA DE CATALUNYA

Mechanical behaviour of tools for shearing Ultra High-Strength Steels: influence of the microstructure on fracture and fatigue micro-mechanisms of tool steels and evaluation of micro-mechanical damage in tools

Ingrid Picas

Supervisors: Dr. Daniel Casellas Padró
Prof. José Manuel Prado Pozuelo

A Thesis submitted for the degree of Doctor in the Universitat Politècnica de Catalunya,
Fundació CTM Centre Tecnològic.

Manresa, September 2012



Acta de qualificació de tesi doctoral

Curs acadèmic:

Nom i cognoms
INGRID PICAS ANFRUNS

DNI / NIE / Passaport
39382200J

Programa de doctorat
Ciència i Enginyeria dels Materials

Unitat estructural responsable del programa
Ciència dels Materials i Enginyeria Metal·lúrgica (CMEM)

Resolució del Tribunal

Reunit el Tribunal designat a l'efecte, el doctorand / la doctoranda exposa el tema de la seva tesi doctoral titulada

Acabada la lectura i després de donar resposta a les qüestions formulades pels membres titulars del tribunal, aquest atorga la qualificació:

APTA/E NO APTA/E

(Nom, cognoms i signatura) President/a		(Nom, cognoms i signatura) Secretari/ària
(Nom, cognoms i signatura) Vocal	(Nom, cognoms i signatura) Vocal	(Nom, cognoms i signatura) Vocal

_____, _____ d'/de _____ de _____

El resultat de l'escrutini dels vots emesos pels membres titulars del tribunal, efectuat per l'Escola de Doctorat, a instància de la Comissió de Doctorat de la UPC, atorga la MENCIÓ CUM LAUDE:

SI NO

(Nom, cognoms i signatura) Presidenta de la Comissió de Doctorat	(Nom, cognoms i signatura) Secretària de la Comissió de Doctorat
---	---

Barcelona, _____ d'/de _____ de _____

« Courage Aliena, tu vaincras »

Acknowledgments

Finally, this will be my Thesis. But this will not be the report of a work I started four years ago, but the culmination of something I began much time before. Something that has sculpted in me who I am, something that has given me a background and above all, something I ought to acknowledge all of you.

To Dr. Daniel Casellas, director of this Thesis and chief of the Materials Technology Area at CTM, for seeing-in and giving all the opportunities to that young, curious girl. For sharing her travel and making her laugh, for the never ending knowledge, motivation and attention. And for never say no. To Prof. José Manuel Prado, co-director of this Thesis and head of CTM, for opening doors ahead of me and giving always good advice. For his incontrovertible knowledge and valuable support, and for getting me entangled in this work.

My best gratitude to Prof. M.Dolors Riera, head of the Simulation and Innovative Design at CTM, for answering my first letter and encouraging me even until this day. Someone I respect and admire, a magnificent woman in world made of steel. To the members of CTM: Ricardo Hernández (for untimely shared hours at work, immeasurable help and existential discussions), Núria Cuadrado (for providing a new “nano” point of view in my work) and to Dr. Giselle Ramírez (for indispensable discussions to bring the Thesis right in the end). To all those who helped me in the laboratory: Miriam Barea, Thais Orellana and Manuela Molina (to whom I owe a complete manicure programme to heal the nails damaged in polishing), Eduard Planas, Sergi Romera, Salvador González, Eduard Vidales and Marc Pla (for helping me in the press, testing machines and for their good technical advices), Carles Abad (for making all possible in the laboratory) and Iban González (master of photography at the head of the SEM, with whom I shared long travels in the cabin of this aircraft). Finally, thanks to all administrative and service staff of CTM, as well as all internship students who have participated in some part of this work.

Thanks to Eva Martínez-González, from LEAM, for our adventure in coupling Acoustic Emission with mechanical tests of tool steels, for our long working days and nice talks. Thanks to Katrin Nothhaft, from UTG, for making me feel at home in Munich and share this unique experience with me. Thanks to Prof. Hartmut Hoffmann for accepting my stay at the institute and assisting me for everything I needed, Dr. Roland Golle and Dr. Matthias Golle for the very interesting discussions, and to all UTG members which contributed to make of this an unforgettable period for me. Special thanks to Prof. Wolfram Volk, who I had the pleasure to know some time after my stay, but to whom I have to acknowledge the culmination of this work.

I ought to thank all Forma0 members for his work within this research project, leaded by SEAT and funded by the Spanish government. Thanks to Prof. Luís Llanes, from CIEFMA, for our fruitful

discussions during the project (which followed at the end of this) and for his capacity to turn any conventional discussion into a magistral lesson of fracture mechanics and fatigue. Thanks to Alexey Goez for his so many interesting results helping to development of this Thesis. My very special gratitude to Isaac Valls, from ROVALMA, to whom I owe much more I can ever express, namely his trust on me since the very first day and my rapid immersion in the field. Thanks to Begoña Casas, for the long hours we spent in SEM and for the remembering times in conferences. Jordi Blanch, Toni Cabrera, Carlos Borrueal, Juan Luna, Gemma Prada, Máximo Villafranca, Rebeca Bueno, Agurtzane Martínez Jonathan Fernández, Francesc Montalá and Alfred Beltran, for their cooperation, without them this work could have never been possible.

My deepest thanks are to those of you who have never failed in supporting me from the distance: Prof. Jean Steinmetz, (*puisque « j'aime tout » et je n'arriverai jamais à choisir le bon port pour vendre la laine de mes moutons*). Thanks to Dr. Josiane Steinmetz, *sans les conseils de qui je n'aurais jamais arrivé à écrire un seul mot du manuscrit*. Zoubir Ayadi, Julien & Zimmermann family, Bertrand & Ihle family, Patricia, Xavier et Arthur Perez, *pour m'ouvrir vos portes un jour et ne jamais les avoir fermé*.

Finally, to you, the ones who have always been there when I knocked your door, listening to my far away calls, facing with me the ups and downs, advising me in my every new challenge: *mama, papa, iaies (i avis si poguessin tornar aquí)*. *Mil gràcies*. And still thanks, thanks to the one who ought to show the most handful of patience waiting at the end of this long and difficult travel started ten years ago: Joan.

To you, tireless companions of walk, brave knights and talented prior, for taking magnificent care of a princess and saving her time after time.

Abstract

The present PhD. Thesis (i.e., “Mechanical behaviour of tools for shearing Ultra High-Strength Steels: influence of the microstructure on fracture and fatigue micro-mechanisms of tool steels and evaluation of micro-mechanical damage in tools”) is aimed at determining the relationship between the microstructure and the mechanical behaviour of tool steels for cold forming and shearing operations of Ultra High-Strength Steels (UHSS) and Press Hardened Steels (PHS).

In this regard the Thesis has analysed the microstructure (section 3.1), the macro- and micro-mechanical properties (sections 3.2.1 and 3.2.2), crack nucleation and growth under monotonic loads and evaluation of *R*-curve behaviour (sections 3.2.3, 3.2.4 and 3.2.6) and fatigue crack nucleation and propagation mechanisms (section 3.2.5) of four different cold work tool steels: 1.2379, UNIVERSAL, K360 and HWS. The Thesis has also studied the mechanical and tribological behaviour of industrial and laboratory tools as well as the effects of shearing process parameters on the performance of tools and quality of sheet sheared edges (section 3.3). Finally, this Thesis has evaluated the suitability of LEFM based models to estimate the life of tools (section 3.4).

The Thesis has rationalised damage on tool steels from a micro-mechanical point of view in laboratory samples (section 4.1) as well as in real tools (section 4.2). It has permitted to identify the aspects that a model should consider in order to successfully predict lives of tools for shearing UHSS, as well as proposing a new approach to predict tool lives based on the reduction of tool steels mechanical properties with the increase of the number of strokes (section 4.3).

Section 3.1 shows that in 1.2379 there is only one type of primary carbide, M_7C_3 -type, rich in Fe and Cr. Carbides in 1.2379 have the highest diameters and the most irregular geometries amongst the studied steels, and they are dispersed forming bands aligned following the forging direction. In K360 there are M_7C_3 , MC and M_4C primary carbides. The chemical composition of the M_7C_3 is very similar to that of the 1.2379, with some V and Mo replacing Cr and Fe. The MC are mainly Nb carbides and the M_4C show high amounts of Mo and Fe. M_7C_3 carbides in K360 are very close in terms of size to those of 1.2379, while MC are smaller and rounder. M_4C carbides of K360 are markedly smaller than the M_7C_3 and MC.

In UNIVERSAL there are M_7C_3 and MC primary carbides. M_7C_3 carbides are also similar to those of 1.2379, except for some Cr which is replaced by V and W. MC carbides are mainly formed by V. M_7C_3 carbides of UNIVERSAL are more regular and rounded than those of 1.2379 or K360 and MC carbides are the most spherical amongst the ingot cast steels and they have also the highest sphericity. In HWS, M_7C_3 , MC and M_6C are present. These carbides are supposed to have similar chemical compositions than

those of UNIVERSAL (except for the M_6C , which is assumed to be mainly formed by Mo and/or W). HWS presents the smallest carbides amongst the studied steels and they are almost like perfect spheres.

Section 3.2 and 4.1 show that ingot cast steels (1.2379, UNIVERSAL and K360) are markedly anisotropic, especially 1.2379 and K360, while HWS (which is a powder metallurgical steel (PM)) shows an isotropic behaviour. The highest mechanical properties of ingot cast steels are obtained for D2 samples, in which primary carbides are oriented following the longest axis of samples. 1.2379 shows the lowest values of fracture strength, σ^R , and fatigue limit, $\Delta\sigma^{fat}$, although K360 presents only slightly better results. UNIVERSAL shows higher σ^R and $\Delta\sigma^{fat}$ than 1.2379 and K360, but HWS shows the highest values. Fracture and fatigue failure initiation sites are primary carbides or agglomerates of them in ingot cast steels and inclusion particles in HWS. Fracture toughness, K_{IC} , and fatigue crack propagation threshold, ΔK_{TH} , and opposite to σ^R and $\Delta\sigma^{fat}$, are the highest in 1.2379 and the lowest in HWS.

These sections also show that the nucleation of cracks in tool steels is due to the failure of primary carbides by cleavage (and inclusion particles in case of PM steels) when the matrix at their surrounding exceeds its yield stress. The yield stress of the matrix, in turn, is determined by the secondary fine carbides precipitated in the martensitic matrix during the tempering treatment. Small cracks nucleated from primary carbides in ingot cast steels are initially very shallow, but they tend to grow to semi-circular shapes as the load increases and they propagate through the matrix bands. Ingot cast tool steels present R -curve behaviour, i.e. fracture toughness depends on the crack size. This is a very important consideration that must be taken into account when designing tools made of ingot tool steels with high fracture resistance for applications under high stress levels, since small cracks nucleated in the microstructure have lower toughness values than those determined for long cracks in standard measurement tests. HWS, in turn, has very high resistance to crack nucleation at primary carbides or inclusions compared to ingot cast steels. Small cracks present semi-circular shapes and their growth is steady through the microstructure. HWS has a flat R -curve behaviour, meaning that fracture toughness is independent with regard of the crack size and that the values determined for long cracks are also valid for small ones.

Section 3.2 presents Acoustic Emission (AE) as potential technique to monitor on-line micro-mechanical damage of tool steels. Preliminary tests under monotonic loads and using laboratory specimens have shown that it is possible to correlate microstructural damage with AE signals, as well as anticipate unstable failure of specimens.

Regarding the fatigue behaviour of tool steels, section 3.2 and 4.1 show that crack propagation mechanisms of short, medium and long cracks are governed by similar mechanical properties to those determined by means of standard tests. In ingot cast steels, initial crack propagation when cracks are still

confined at the carbide cluster is rather tortuous and does not show a stable growth. The shape of the fractured carbides determines the shape of initial cracks and therefore, the condition of $\Delta K \geq \Delta K_{TH}$ necessary so that propagation starts. As long as $\Delta K < \Delta K_{TH}$, propagation does not take place. However, if the size of nucleated cracks fulfils the aforementioned condition they successfully grow through the matrix. Once they attain a certain size (usually when they propagate out from the initial cluster) the growth is more stable and steady, independently of the primary carbides ahead. Once a stable propagation rate is attained, cracks approach semi-circular shapes and keep growing in equilibrium for the rest of the fatigue cycles. In HWS, once cracks are successfully nucleated, propagation stages are rather short in fatigue since the resistance of the microstructure to the propagation of cracks is low. Given that the microstructure ahead of nucleated cracks in HWS is very homogeneous, stable propagation of these into semi-circular shapes is expected already from the initial stages.

In 1.2379 and K360, crack nucleation in fatigue is due in great extent, to primary carbides broken already at the first load cycles since the fatigue limit, in terms of the maximum applied stress, σ^{max} , is higher than the fracture strength of primary carbides, σ^{RC} . In UNIVERSAL, σ^{max} is lower than σ^{RC} . Thus, breakage of carbides cannot be understood because the applied stress is higher than σ^{RC} , but because the strain in the matrix around the primary carbide increases with the number of cycles due to the reduction of mechanical properties of the metallic counterpart. The strain in the matrix exceeds the amount of strain that the primary carbide can withstand and as a result, it breaks. As in HWS no large carbides are present, it is plausible that the matrix at the neighbourhood of inclusion particles is subject to more distortion and stresses rise with respect to the rest of the microstructure. Thus, cracks may finally nucleate due to the reduction of the matrix properties at their surroundings.

Section 3.3 and section 4.2 show that the main failure mechanism of tools for punching and slitting UHSS is chipping at the cutting edge. An analysis at the micro level has shown that different types of damage are present in tools and that they contribute to the formation of chipping at the cutting edge. Plastic deformation and nucleation of cracks at the surface of tools occurs as a result of the high frictional forces during sliding against the sheet. Due to the high contact pressures at the surface, carbides within a narrow range of depth beneath the surface are also broken. Breakage of carbides takes also place because of the tensile residual stresses that are generated after full unloading, due to plastic deformation of the matrix during the backwards movement of the punch. Cracks are also nucleated from surface asperities, ahead of which a stress state similar to that created on a notch root is generated. Chipping is then explained by the nucleation of a crack at the rake face and its propagation to the flank face, or by the coalescence of two cracks, one nucleated at the rake face and the other at the flank face.

In presence of marked grinding grooves, failure of tools is significantly accelerated in this type of applications dealing with such high strength sheet steels. Hence, the first condition to ensure the best performance of tools possible, and that tool steels show all their potential is to find and apply the optimal grinding parameters.

Section 3.3 shows that models based on LEFM seem rather insufficient to accurately predict the life of tools. These models assume that a crack is already present in the microstructure at the cycle number one, and that if it is nucleated from primary carbides or inclusion particles. However, in tools there may always be a time for nucleation and they do not exclusively nucleate from primary carbides or inclusions but from surface irregularities, wear particles, etc. Hence, the life of tools cannot be accurately predicted by means of these models.

Section 4.3 shows that some of the concerns which come in mind when trying to set up a model to predict tool lives are first, that not only one single type of micro-mechanism leading to damage and/or chipping is identified neither in punching nor slitting tools, but multiple damaging mechanisms contribute, under different degrees of implication, to the macroscopic failure of tools. Second, the acting stresses cannot be determined locally in a microstructural scale for tools. FE-simulation results are helpful determining macroscopically, the stress state of the punch and assess the severity of an operation with respect to another. However, from a micro-mechanical point of view, stresses predicted by means of macro FE-models cannot explain the type of damage observed. In this regard, as contact pressures play an important role in tools, the fact that the surface is under constant evolution due to wearing out effects is also a limiting factor for the considerations of the model. Wear and fatigue are related processes in these tools in a way that some mechanisms are explained because of the conjunction of both. That means that a proper model to predict the life of tools should not disregard the wear effects on the surface since they contribute to the nucleation of fatigue cracks. The last matter is to know how the differences observed in tests with laboratory samples between small and large cracks apply also in tools, especially to take into account *R*-curve effects on crack behaviours in tools.

A new approach to predict tool lives is proposed in section 4.3, which holds the idea that the micro-mechanical properties of the metallic matrix in tool steels decrease due to the application of repetitive load. The model basically sustains the reduction of E , which can be related to a certain applied stress and number of cycles, in a way to predict tool lives based on micro-mechanical damage. By means of this model, not only damage as a result of broken primary carbides or inclusion particles can be detected, but also wear or plastic deformation can be taken into account since they may lead to a reduction of E as well. In addition, this model avoids any consideration of crack size – toughness dependency, surface roughness, stress state and level, tool geometry, shearing parameters, etc., as it only accounts for a decrease of

mechanical properties of the metallic matrix, whatever it is the triggering effect. Future works have to progress in order to be able to develop a model which can accurately estimate the failure of tools by means of the reduction of E .

Contents

Acknowledgments.....	vii
Abstract.....	ix
Contents.....	xv
List of figures.....	xxi
List of tables.....	xxxix
List of symbols.....	xli
List of abbreviations.....	xliv
Preface.....	xlvi
Motivation: objectives.....	xlviii
1. Introduction.....	51
1.1 Tool steels for cold forming and shearing applications.....	51
1.1.1 Manufacturing methods of tool steels.....	52
1.1.2 Hardening heat treatment.....	53
<i>1.1.2.1 Austenitizing and quenching.....</i>	<i>54</i>
<i>1.1.2.2 Tempering.....</i>	<i>55</i>
1.2 Fracture resistance of tool steels.....	57
1.2.1 The stress intensity factors and the notion of fracture toughness.....	58
<i>1.2.1.1 Linear elastic fracture mechanics (LEFM).....</i>	<i>58</i>
<i>1.2.1.2 Elastic-plastic fracture mechanics.....</i>	<i>59</i>
1.2.2 The role of the tool steel microstructure in the fracture process.....	63
<i>1.2.2.1 The fracture process in tool steels.....</i>	<i>63</i>
<i>1.2.2.2 Influence of the intrinsic plasticity of the metallic matrix in the fracture toughness of tool steels.....</i>	<i>66</i>
<i>1.2.2.3 Dislocation movement and crack propagation in tool steels.....</i>	<i>69</i>
1.2.3 Crack nucleation and growth in tool steels.....	72
<i>1.2.3.1 Principles of R-curve in tool steels.....</i>	<i>72</i>
<i>1.2.3.2 The R-curve behaviour of tool steels as described by Gomes et al.....</i>	<i>74</i>
1.3 Fatigue resistance of tool steels.....	78
1.3.1 Fatigue crack initiation mechanisms in tool steels.....	78
<i>1.3.1.1 The different failure modes observed in fatigue of tool steels.....</i>	<i>78</i>
<i>1.3.1.2 Plastic damage mechanisms versus carbide fracture as fatigue crack initiators in tool steels.....</i>	<i>82</i>
1.3.2 Fatigue crack propagation mechanisms in tool steels.....	84

1.3.2.1	<i>The notion of the stress intensity factor in fatigue: stress and crack length correlations with fatigue crack propagation.....</i>	84
1.3.2.2	<i>Growth of physically short cracks.....</i>	86
1.3.2.3	<i>Microstructural aspects of fatigue crack propagation in tool steels.....</i>	87
1.4	Failure in tools for shearing Ultra High-Strength Steels.....	91
1.4.1	The shearing process.....	91
1.4.2	Ultra High-Strength Steels.....	96
1.4.3	Damaging mechanisms in tools.....	97
1.5	Methods for tool life prediction.....	103
1.5.1	Existing models for fatigue life prediction based on LEFM.....	104
1.5.2	Existing patents on methods to predict damage of tools.....	109
2.	Experimental procedure.....	111
2.1	Material.....	111
2.2	Microstructure analysis.....	112
2.3	Mechanical properties.....	114
2.3.1	Fracture strength, σ^R , and fatigue limit, $\Delta\sigma^{fat}$	114
2.3.2	Fracture toughness, K_{IC} , and fatigue crack propagation threshold, ΔK_{TH}	115
2.4	Study of crack nucleation and growth in tool steels.....	116
2.4.1	Micro-mechanical properties of the primary carbides and the metallic matrix...	116
2.4.2	Crack nucleation and growth under monotonic loading.....	116
2.4.3	Monitoring micro-damage using Acoustic Emission techniques.....	117
2.4.4	Crack nucleation and propagation in cyclic loading conditions.....	119
2.4.5	Subcritical growth of small cracks: assessment of <i>R</i> -curve behaviour.....	120
2.5	Mechanical and tribological behaviour of tools for cold forming and shearing UHSS.....	121
2.5.1	Identification of the main failure mechanisms of industrial tools.....	121
2.5.2	Characterization of the damaging processes of tools working in industrial conditions and their evolution with the number of strokes.....	121
2.5.2.1	<i>Trimming of press hardened boron steel 2 mm thick (at SEAT S.A.).....</i>	<i>122</i>
2.5.2.2	<i>Punching of MS-W1200 2 mm thick (at AUTOTECH ENG.).....</i>	<i>127</i>
2.5.2.3	<i>“Matriu de Dany Accelerat (MDA)” : forming and punching TRIP 800 and DP1000, both 2 mm thick (at TROE S.L.).....</i>	<i>129</i>
2.5.3	Conception, design and construction of a die for laboratory benchmark and tests reproducing the failure mechanisms of industrial tools.....	131
2.5.4	Instrumentation of tools: analysis of cutting loads and displacements.....	134
2.5.5	Influence of the shearing process parameters on the tool behaviour and part	135

quality.....	
2.5.6 Stress distribution in cold forming and shearing tools.....	137
3. RESULTS.....	139
3.1 Tool steels microstructure.....	139
3.1.1 Primary alloy carbides.....	139
3.1.1.1 Structure, percentage in the microstructure and chemical composition.....	139
3.1.1.2 Distributions of size and morphology.....	141
3.1.2 Metallic matrix.....	145
3.2 Influence of the microstructure on the macro- and micro-mechanical properties of tool steels.....	148
3.2.1 Macro-mechanical properties.....	148
3.2.1.1 Fracture strength, σ^R	148
3.2.1.2 Fatigue limit, $\Delta\sigma^{fat}$	152
3.2.1.3 Fracture toughness, K_{IC}	160
3.2.1.4 Fatigue crack propagation threshold, ΔK_{TH}	160
3.2.2 Micro-mechanical properties of primary carbides and metallic matrix in ingot cast steels.....	161
3.2.2.1 Mechanical properties of primary carbides.....	161
3.2.2.2 Mechanical properties of the metallic matrix.....	162
3.2.3 Crack nucleation and growth under monotonic load.....	163
3.2.3.1 Crack nucleation and growth in ingot cast steels.....	163
3.2.3.2 Crack nucleation and growth in PM tool steels.....	172
3.2.4 Monitoring micro-damage using Acoustic Emission techniques.....	174
3.2.4.1 Identification of characteristic AE signal patterns in bending tests of 1.2379 under monotonic loading.....	174
3.2.4.2 Influence of the tool steel microstructure on the acquired AE signals.....	176
3.2.5 Crack nucleation and propagation mechanisms under cyclic load.....	180
3.2.5.1 Fatigue crack propagation threshold and shapes of small cracks in ingot cast steels.....	180
3.2.5.2 Stable fatigue crack propagation and shapes of “medium” sized cracks in ingot cast steels.....	184
3.2.5.3 Fatigue crack nucleation in ingot cast steels.....	190
3.2.5.4 Fatigue crack nucleation and propagation in HWS.....	193
3.2.6 Monotonic subcritical crack growth in tool steels.....	196
3.2.6.1 Geometry of microcracks under monotonic loading.....	198
3.2.6.2 R-curve behaviour.....	204
3.3 Mechanical and tribological behaviour of tools working in industrial	216

conditions.....	
3.3.1 Main failure mechanisms of tools in forming and shearing operations.....	216
3.3.2 Characterization of the damaging processes and their evolution with the number of strokes in tools working in industrial conditions: relationship between the microstructure and the failure mechanisms of tool steels.....	218
3.3.2.1 <i>Trimming of press hardened boron steel, 2 mm thick (at SEAT S.A.).....</i>	219
3.3.2.2 <i>Punching of MS-W1200, 2 mm thick (at AUTOTECH ENG.).....</i>	224
3.3.2.3 <i>Matriu de Dany Accelerat (MDA): forming and punching TRIP 800 and DPI1000, both 2 mm thick (at TROE S.L.).....</i>	228
3.3.3 Analysis of the performance of shearing tools: relationship between the acting mechanical solicitations and damage in the microstructure.....	241
3.3.3.1 <i>Damage mechanisms in punching tools.....</i>	241
3.3.3.2 <i>Damage mechanisms in slitting tools.....</i>	260
3.3.4 Effect of the shearing process parameters on the quality of the cut edges, the performance of tools and the registered load - displacement curves.....	273
3.3.4.1 <i>Influence of the process parameters on maximum loads registered in tools and the quality of the sheared edges.....</i>	274
3.3.4.2 <i>Influence of the shearing clearance and tool edge radius on the performance of tools.....</i>	280
3.3.4.3 <i>Influence of the slitting process parameters on the registered load and displacement of tools.....</i>	284
3.4 Tool life prediction models based on LEFM.....	286
4. DISCUSSION.....	298
4.1 Fracture and fatigue micro-mechanisms of tool steels.....	298
4.1.1 <i>Crack nucleation under monotonic load.....</i>	298
4.1.2 <i>Subcritical growth of cracks under monotonic load.....</i>	302
4.1.3 <i>Fatigue crack nucleation and propagation: rationalization in basis of the mechanisms observed under monotonic load.....</i>	305
4.2 The case of real tools. An in-depth study of the failure mechanisms from a micro-mechanical point of view.....	312
4.2.1 <i>Micro-mechanical analysis of the punching tools.....</i>	313
4.2.2 <i>Micro-mechanical analysis of slitting tools.....</i>	326
4.3 Corollary.....	344
4.3.1 <i>Considerations to the development of a model for tool life prediction: can this model be a reality?</i>	344
4.3.2 <i>An application of the micro-mechanical damage based model for life prediction of industrial tools.....</i>	350

5. Conclusions.....	353
List of references.....	360
Published articles.....	366
Articles published in conferences.....	367
Articles submitted.....	369

List of figures

Figure 1.1.1	a) Primary carbides are elongated after hot working and they are dispersed forming bands oriented along with the rolling direction; b) spheroidized secondary carbides (small red arrows) coexist in the martensite matrix.....	52
Figure 1.1.2	a) Primary carbides in PM steels are dispersed in a uniform distribution even after hot working; b) carbides show spheroidized shapes and small dimensions.....	53
Figure 1.1.3	Schematic diagram of tool steel hardening heat treatment steps.....	53
Figure 1.1.4	Schematic diagram of hardness versus tempering temperature (assuming constant time at each temperature) for high-speed or high-carbon, high-chromium tool steels.....	55
Figure 1.2.1	Elliptical hole in infinitely large panel.....	58
Figure 1.2.2	Basic modes of loading involving different crack surface displacements.....	60
Figure 1.2.3	Onset of plastic deformation at the crack tip. “Effective” crack length taken to be initial crack length plus the plastic zone radius.....	61
Figure 1.2.4	Fracture in a) thin sheets under plane stress state and b) thick plates under plane strain conditions.....	62
Figure 1.2.5	Fracture toughness in function of the material thickness under plane stress and plane strain conditions.....	62
Figure 1.2.6	Accumulated effective plastic strain in the matrix of the individual layers as a function of the uniaxial tensile macro stress predicted via the micro-meso-macro layer model incorporating the MEFM (multiparticle effective field method); carbidic stringers and carbidic poor zones are denoted by CS and CP respectively; H denotes high-speed steel with a statistically homogeneous carbide distribution [RAM99].....	65
Figure 1.2.7	Maximum principal stress: a) in the carbides and b) in the matrix, in the individual layers predicted via the micro-meso-macro layer model incorporating the MEFM (multiparticle effective field method). The intersection between the horizontal line and the curve indicates initiation of a) carbide and b) matrix cracking at the corresponding macro stress; carbidic stringers and carbidic poor zones are denoted by CS and CP respectively; H denotes high-speed steel with statistically homogeneous inclusion distribution [RAM99].....	65
Figure 1.2.8	Fringes of the maximum principal stress in the carbides predicted via the Hexagonal Tiling concept at an applied overall load of $\sigma_{II} = 2900$ MPa [RAM99].	66
Figure 1.2.9	Fracture toughness, K_{IC} , at constant hardness, $HV30$, versus mean carbide diameter, d , and volume fraction of carbides, f [HOR83].....	68
Figure 1.2.10	Fracture toughness and hardness versus tempering temperature for 10x17 mm M2 bar, after quenching to room temperature and after immersion in liquid N ₂ before tempering; all samples austenitized at 1220 °C for 4 min [HOR83].....	69
Figure 1.2.11	The onset of plastic flow controlled by obstacles: plasticity requires bypassing of strong obstacles by dislocations, equivalent to the condition that dislocation loop fit between neighbouring obstacles.....	70

Figure 1.2.12	Size effect resulting from a \sqrt{r} -dependence of the cutting stress (Equation 1.2.8) and a $1/r$ -dependence of the bypassing stress (Equation 1.2.9) This causes maximum in yield stress σ_y vs particle radius R at a characteristic value r_c	71
Figure 1.2.13	Crack deflection geometries in two-phase solids: a) tilt deflections around spheres, large mode II component (crack propagation left to right); b) twist deflections around rods, large mode III component (crack propagation into plane of diagram – dashed line undisturbed crack plane).....	71
Figure 1.2.14	Division of crack along extended weak interface in tensile specimen. Driving force for extension diminishes as secondary fracture grows further from primary plane.....	72
Figure 1.2.15	Instability condition occurs in cracked solid when $dG/da = dR/da$	73
Figure 1.2.16	Experimental R -curves from stress generated crack nuclei for two T1 high-speed steel bend specimens which failed at $K < K_{IC}$. Contrast the markedly stepwise behaviour of the (b) specimen with that of (a), which involved linking up two crack nuclei along prior austenite grain boundaries, oriented nearly perpendicularly to the tensile axis [GOM97].....	75
Figure 1.2.17	Geometry of a surface crack; $2c$ is the surface major axis and a the interior semi-minor axis, the crack depth. The thickness, t , and width, $2b$, of the specimen are also shown.....	76
Figure 1.3.1	SEM observations of a) surface crack initiation sites and b) fish-eye type fracture surface [SHI01].....	79
Figure 1.3.2	Proposed model, “dispersive decohesion of spherical carbide”, for the formation of the GBF area around an inclusion (black area on the left side of the images) during a very high-cycle fatigue process [SHI06-1].....	80
Figure 1.3.3	Fracture surface of AISI D2 type tool steel specimen failed after $6,1 \cdot 10^6$ cycles at 800 MPa: a) SEM image of internal fatigue crack nucleation and propagation zones; b) SEM image of GBF (or “granular bright area (GBA) as referred in the work of Sohar et al.) in the vicinity of the carbide cluster; c) and d) BSE images revealing the granular surface morphology within the GBF [SOH08-2].....	82
Figure 1.3.4	Diagram showing three regimes of fatigue crack growth response. Region I, crack growth rate decreases rapidly with decreasing ΔK and approaches lower limit at ΔK_{TH} ; Region II, midrange of crack growth rates where “power law” dependence prevails; region III, acceleration of crack growth resulting from local fracture as K_{max} approaches K_C	85
Figure 1.3.5	Diagram showing fracture mode transition from flat to slant fracture appearance...	86
Figure 1.3.6	Effective ΔK level as a function of crack length at two load levels. At P_I , ΔK will decrease below ΔK_{TH} as a crack moves through notch root zone. Crack arrest will then occur.....	87
Figure 1.3.7	Bilinear fatigue crack growth behavior. Microstructure - sensitive behavior observed when reversed plastic zone $<$ mean grain size. Microstructure - insensitive mode occurs when reversed plastic zone $>$ mean grain size.....	88
Figure 1.3.8	SEM micrograph of the notch surface after 10 loading cycles [JES06].....	90
Figure 1.3.9	Schematic representation of the different fracture mechanisms in quenched and tempered PM steel in the: a) near threshold region and b) and c) upper Paris regime with crack propagation with cleaved carbide in the crack growth direction and normal to it respectively [JES09].....	91
Figure 1.4.1	Shearing of metal sheet.....	91

Figure 1.4.2	Shearing with: a) insufficient clearance; b) excessive clearance.....	92
Figure 1.4.3	a) Phases of the shearing process; b) schema of the sheared edge.....	93
Figure 1.4.4	a) Phases of the shearing process; b) schema of the cut edge.....	94
Figure 1.4.5	Components of the shearing force, F_S : vertical force, F_V , horizontal force, F_H , and bending moment M [adapted from LAN90].....	94
Figure 1.4.6	Shearing processes [adapted from LAN90].....	95
Figure 1.4.7	Schematic of UHSS compared to HSS [KOG09].....	96
Figure 1.4.8	Location of the two crack sites in the lower set of the backward extrusion tooling [NAG94].....	97
Figure 1.4.9	Contours of accumulated effective plastic strain, p , and damage, D , in the radius transition region after 50 subsequent load cycles: a) fillet radius A, p , prestressed die; b) fillet radius A, D , prestressed die; c) fillet radius A, p , die without prestress; d) fillet radius A, D , die without prestress; e) fillet radius B ($B>A$), p , prestressed die; f) fillet radius B ($B>A$), D , prestressed die [PED97].....	98
Figure 1.4.10	SEM-SE picture of: a) an opened specimen. In the top left corner, the part of the crack that is visible in the unopened specimen can be seen. In the lower part of the picture the crack running inside the specimen can be observed; b) fractured carbides in the bottom of the crack [VIN02].....	99
Figure 1.4.11	a) Crack morphology showing crack link up and propagation along aligned carbide stringers; b) crack propagation along angular carbides [KRI07].....	100
Figure 1.4.12	a) Example of superficial micro-chipping in presence of branching phenomena; b) Diagram of coplanar advancement of a sub-superficial crack, with a propagation towards the surface along perpendicular directions (the arrows show the direction of fatigue propagation) [BON06].....	101
Figure 1.4.13	Classification of the main damaging mechanisms observed in punching tools after piercing larger thickness plates of AISI 52100 steel: a) side wear; b) face wear; c) chipping; d) cracking; e) gross fracture [LUO99].....	102
Figure 1.5.1	a) Carbide size distribution presented as cumulative number of carbides with size larger than a certain equivalent diameter plotted vs carbide diameter; b) cumulative number of inclusions with size larger than a specific value plotted vs inclusion size. PM23, ASP2014 and VANADIS 10 were PM steels and M2 was ingot cast [MEU01].....	106
Figure 1.5.2	Model fatigue limit vs experimental fatigue strength at $2 \cdot 10^6$ cycles. *PM23 was longitudinally ground instead of hard-turned and polished as the rest of specimens [MEU01].....	107
Figure 1.5.3	a) Cluster of carbides; b) cracks at carbides in a cluster; c) crack through cluster [RAN08].....	108
Figure 1.5.4	a) Failure probabilities for the steels VANADIS10, M2, PM23 and ASP2014 with $f_c = 0,5$; b) failure probabilities for the steels VANADIS10, M2, PM23 and ASP2014 with $f_c = 0,25$ [MEL02].....	109
Figure 2.1.1	Sampling: samples perpendicular (D1), parallel (D2) and transverse (D3) to the forging direction.....	111
Figure 2.2.1	Images obtained by SEM using backscatter detection: a) 1.2379 and b) HWS.....	112

Figure 2.2.2	Studied parameters by means of image analysis: a) equivalent diameter (ECD); b) minimum diameter (D_{min}); c) maximum diameter (D_{max}); d) aspect ratio (AR); e) sphericity (ψ); f) shape factor (SP).....	113
Figure 2.3.1	a) Schema of the three point bending test with a constant span length of 40 mm; b) testing under monotonic load to determine σ^R ; c) testing under cyclic load and d) schema of the staircase method applied to calculate $\Delta\sigma^{fat}$	115
Figure 2.3.2	a) Schema of the three points bending test with a constant span length of 40 mm and using prismatic pre-notched specimens; b) fatigue pre-cracking in the resonance testing machine, crack propagation was monitored by means of strain gauges; c) fracture of the precracked specimens.....	116
Figure 2.4.1	a) Stepwise monotonic tests and surface inspections; b) schema of the inspected zone in the tensile face of samples.....	117
Figure 2.4.2	Experimental set-up for the AE monitored bending tests.....	119
Figure 2.5.1	Geometry of the remnant B-pillar flanges used for trimming at SEAT S.A. (the arrow shows the location of the trimming in the sample).....	123
Figure 2.5.2	a) Schema of the trimming process; b) real tools in the press; moving blades A and B, and stationary blade C.....	123
Figure 2.5.3	Profiles at the cutting edge and the estimation of wear.....	124
Figure 2.5.4	Translation of P2, P3 and P4 to P1 in the X-Y coordinate system.....	124
Figure 2.5.5	P1, P2, P3 and P4 rotation.....	125
Figure 2.5.6	P1, P2, P3 and P4 in the reference scale window and plotted separately in black and white.....	126
Figure 2.5.7	P1 profile in gray scale vs pixels obtained with <i>IMAGEJ</i>	126
Figure 2.5.8	a) P1, P2, P3 and P4 rescaled in microns after treatment with <i>IMAGEJ</i> ; b) calculated areas in correlation with the respective number of strokes.....	127
Figure 2.5.9	a) Schematic description of the punching operation; b) picture of one of the sets of tools employed.....	128
Figure 2.5.10	a) Identification of six different zones along the punches cutting edge, in red the polished face of each specimen; b) punch after the extraction of the specimen; c) extracted specimen and d) image of the microstructure below the cutting edge obtained after polishing the cross sectional face shown in a).....	128
Figure 2.5.11	MDA in TROE S.L.....	129
Figure 2.5.12	Description of the forming and shearing process studied in the MDA.....	130
Figure 2.5.13	Spare tools used in the MDA; step, type, material, hardness and designation of each tool.....	130
Figure 2.5.14	a) - b) Profile measurement at the tool edge; c) schema of the estimation of material lost by wear (tool radius variation).....	131
Figure 2.5.15	a) HPC; b) coil of DP1000 2 mm thick used in these tests; c) schematic description of the shearing processes studied in the HPC (punching and slitting).....	132
Figure 2.5.16	a) Punches of the HPC; b) slitting tools of the HPC.....	133
Figure 2.5.17	Transverse specimens of punches to analyse the microstructure beneath the cutting edge.....	133

Figure 2.5.18	Transverse specimens of slitting tools to analyse the microstructure beneath the cutting edge.....	134
Figure 2.5.19	Schematic description of the matrix used for the cutting tests at UTG.....	134
Figure 2.5.20	a) Test facility and sensors set-up; b) adjustable elements to vary the cutting clearance.....	135
Figure 2.5.21	a) Tensile stress-strain curve of the 22MnB5 material used for the cutting tests; b) schema of the cutting parameters used in the tests.....	135
Figure 2.5.22	a) MTEC-p for punching tests; b) MTEC-s for slitting tests.....	136
Figure 3.1.1	Microstructures of the four studied tool steels: a) 1.2379, b) K360, c) UNIVERSAL and d) HWS.....	139
Figure 3.1.2	Backscatter Diffraction images showing the carbides identified at the microstructure of a) 1.2379; b) K360; c) UNIVERSAL and d) HWS.....	141
Figure 3.1.3	Size distribution of primary carbides in terms of the cumulative number of carbides with equivalent diameter, minimum diameter and maximum diameter larger than a certain: a) - b) ECD , c) - d) D_{min} and e) - f) D_{max} , plotted vs ECD , D_{min} and D_{max} respectively. a), c) and e) M_7C_3 carbides of 1.2379, M_7C_3 and MC carbides of UNIVERSAL and M_7C_3 and MC of K360; b), d) and f) M_4C carbides of K360 and M_7C_3 , MC and M_6C carbides of HWS.....	143
Figure 3.1.4	Geometry distribution of primary carbides in terms of the cumulative number of carbides with aspect ratio, sphericity and shape factor larger than a certain a) - b) AR , c) - d) ψ and e) - f) SF , plotted vs AR , ψ and SF respectively. a), c) and e) M_7C_3 carbides of 1.2379, M_7C_3 and MC carbides of UNIVERSAL and M_7C_3 and MC of K360; b), d) and f) M_4C carbides of K360 and M_7C_3 , MC and M_6C carbides of HWS.....	144
Figure 3.1.5	TEM micrographies of the identified secondary carbides in the UNIVERSAL steel matrix: a) type A (Fe-Cr); b) type B (Cr); c) type C (V) and d) type D (W).....	146
Figure 3.1.6	Results of the EBSD local indexation of the UNIVERSAL steel matrix.....	147
Figure 3.2.1	Fracture strength, σ^R , of 1.2379, UNIVERSAL and HWS in D1, D2 and D3, and K360 D1 and D2.....	148
Figure 3.2.2	Weibull probability of failure, P , expressed in terms of $Ln((1/1-P))$ vs σ^R	149
Figure 3.2.3	Fracture initiation sites in D2 samples of a) 1.2379; b) UNIVERSAL; c) K360 and d) HWS. Red arrows indicate the presence of primary carbides at failure origins.....	151
Figure 3.2.4	Fatigue limit, $\Delta\sigma^{fat}$, of 1.2379, UNIVERSAL and HWS in D1, D2 and D3, and K360 D1 and D2.....	152
Figure 3.2.5	Fatigue initiation sites in D2 samples of a) 1.2379; b) UNIVERSAL; c) K360 and d) HWS. Red arrows indicate the presence of primary carbides and inclusions at failure origins.....	154
Figure 3.2.6	Maximum applied stress, σ_a^{max} , vs the number of cycles for the specimens tested in the staircase method to determine $\Delta\sigma^{fat}$: a) 1.2379 D1; b) 1.2379 D2; c) 1.2379 D3; d) UNIVERSAL D1; e) UNIVERSAL D2; f) UNIVERSAL D3; g) K360 D1 and h) K360 D2.....	156
Figure 3.2.7	SEM observations of the fracture initiation sites in K360 D2: a) surface crack initiation at low number of cycles and b) internal crack initiation forming fish-eye at higher number of cycles.....	158

Figure 3.2.8	Surface roughness along the red line on the fracture surface of a specimen showing subsurface failure mode.....	159
Figure 3.2.9	SEM observations of the crack initiation site at the centre of the fish-eye: a) secondary electron and b) back scatter images.....	159
Figure 3.2.10	Fracture toughness, K_{IC} , of 1.2379, UNIVERSAL and HWS in D1, D2 and D3, and K360 D2.....	160
Figure 3.2.11	Fatigue crack propagation threshold, ΔK_{TH} , of 1.2379, UNIVERSAL and HWS in D1, D2 and D3, and K360 D2.....	161
Figure 3.2.12	Broken primary carbides at the surface of D2 specimens tested under monotonic load: a), b) and c) M_7C_3 of 1.2379 at 500 MPa; d) and e) M_7C_3 of UNIVERSAL at 1300 MPa; f) MC of UNIVERSAL at 1600 MPa; g) and h) M_7C_3 of K360 at 500 MPa; i) MC of K360 at 1300 MPa.....	165
Figure 3.2.13	Broken primary carbides at the surface of D3 specimens tested under monotonic load: a), b) and c) M_7C_3 of 1.2379 at 800 MPa; d) and e) M_7C_3 of UNIVERSAL at 1200 MPa and f) MC of UNIVERSAL at 1400 MPa.....	166
Figure 3.2.14	Von Mises stress distribution in a carbide when a macroscopic tensile stress of 1000 MPa is applied: a) equivalent to D2 and b) equivalent to D3.....	166
Figure 3.2.15	Schema of the effective microstructure during a three points bending test at the zone subjected to the highest stress: a) D2 sample configuration and b) D3 sample configuration.....	167
Figure 3.2.16	Evolution of cracks at the surface of the sample 1.2379 D2 at the applied stresses of: a) 900 MPa; b) 1100 MPa; c) 1400 MPa; d) 1700 MPa; e) 2000 MPa; f) 2400 MPa and g) fracture at 2364 MPa.....	169
Figure 3.2.17	Evolution of cracks at the surface of the sample UNIVERSAL D2 at the applied stresses of : a) 2400 MPa; b) 2800 MPa; c) 3000 MPa; d) 3200 MPa; e) 3400 MPa and f) fracture at 3521 MPa.....	169
Figure 3.2.18	Evolution of cracks at the surface of the sample K360 D2 at the applied stresses of: a) zoom at 1600 MPa; b) 1600 MPa; c) 1900 MPa; d) 2200 MPa; e) 2600 MPa and f) fracture at 2964 MPa.....	170
Figure 3.2.19	Evolution of cracks at the surface of the sample 1.2379 D3 at the applied stresses of: a) 900 MPa; b) 1100 MPa; c) 1200 MPa and d) fracture 1310 MPa.....	170
Figure 3.2.20	Evolution of cracks at the surface of the sample UNIVERSAL D3 at the applied stresses of: a) 1600 MPa; b) 1800 MPa and c) 2100 MPa.....	171
Figure 3.2.21	Mechanism of crack growth and plastic deformation around the cracked carbide. Figures a) throughout e) show the steps of the process at different increasing applied stresses.....	172
Figure 3.2.22	Cracks nucleated in HWS D2 from inclusion and carbide particles: a) decohesion of an inclusion with an emanating crack at 3500 MPa; b) decohesion of an inclusion with an emanating crack at 3800 MPa; c) fracture of an inclusion and emanating crack at 3800 MPa and d) breakage and decohesion of carbides at 3800 MPa.....	172
Figure 3.2.23	Evolution of a crack nucleated at an inclusion in HWS D2: a) at 3483 MPa; b) at 3582 MPa; c) at 3781 MPa; d) at 3980 MPa; e) at 4179 MPa and f) fracture at 4319 MPa.....	173

Figure 3.2.24	a) Cumulated number of hits in function of the stress applied during the bending test and the location of the signals at the sample surface; b) cumulated number of hits vs applied stress during a monotonic bending test in which two different types of AE signals can be observed; c) cumulated number of hits vs frequency for the two signals registered.....	175
Figure 3.2.25	AE signal results of monotonic stepwise tests in 1.2379 in terms of the cumulated number of hits vs applied stress to: a) 800 MPa; b) 2200 MPa and c) 2600 MPa.....	175
Figure 3.2.26	Images of the microstructure of 1.2379 at: a) 800 MPa; b)-c) 2200 MPa and d) 2600 MPa.....	176
Figure 3.2.27	Cumulative number of AE hits for the two signal types vs the applied stress for: a), b) and c) three different 1.2379 samples.....	177
Figure 3.2.28	Micrographs of the surface of the three different 1.2379 samples whose AE results are shown in Figure 3.2.27: a) sample corresponding to the AE results of Figure 3.2.27 a), where lots of broken primary carbides are observed; b) sample corresponding to the AE results of Figure 3.2.27 b), where a lower number of broken primary carbides is present; c) and d) sample corresponding to the AE results of Figure 3.2.27 c), where practically no broken carbides are identified but a long crack is found near to the fracture surface.....	178
Figure 3.2.29	Cumulative number of AE hits vs applied stress for: a) 1.2379; b) UNIVERSAL and c) HWS.....	179
Figure 3.2.30	Images of the microstructure of HWS whose AE results are shown in Figure 3.2.29.....	179
Figure 3.2.31	Three different broken carbides (1, 2, 3) in 1.2379 D2 at $\Delta\sigma$ 720 MPa and after: a) 10000 cycles; b) 20000 cycles; c) 45000 cycles and d) 745000 cycles.....	181
Figure 3.2.32	The three broken carbides in 1.2379 D2 now at $\Delta\sigma$ 820 MPa and after 3000 cycles: a) crack number 1; b) crack number 2 and c) crack number 3.....	182
Figure 3.2.33	The three broken carbides (1, 2 and 3) in 1.2379 D2 now at $\Delta\sigma$ 855 MPa after: a) 3000 cycles and b) 13000 cycles.....	183
Figure 3.2.34	Fatigue halos observed at the fracture surface of 1.2379 D2 samples: a) $\Delta\sigma$ 810 MPa, N 11195 cycles, a 335 μm , $2c$ 690 μm and a/c 0,97; b) $\Delta\sigma$ 720 MPa, N 29375 cycles, a 841 μm , $2c$ 1740 μm and a/c 0,97 and c) $\Delta\sigma$ 630 MPa, N 83329 cycles, a 922 μm , $2c$ 1844 μm and a/c 1	185
Figure 3.2.35	Cracks developed at the surface of the 1.2379 D2 sample at $\Delta\sigma$ 855 MPa and after 13000 cycles: a) $2c_1$ 262 μm ; b) $2c_2$ 197 μm and c) $2c_3$ 83 μm and $2c_4$ 114 μm	185
Figure 3.2.36	Fracture surface of the 1.2379 D2 broken monotonically after some cracks had been nucleated in fatigue. The halo of the fatigue precrack has the following dimensions: a 122 μm and $2c$ 262 μm (a/c 0,9).....	186
Figure 3.2.37	Stable crack growth in the UNIVERSAL D2 sample at $\Delta\sigma$ 990 MPa (red arrows indicate the length of the crack, $2c$): a) 1500 cycles, $2c$ 61 μm ; b) 16000 cycles, $2c$ 69 μm ; c) 18000 cycles, $2c$ 96 μm ; d) 21000 cycles, $2c$ 169 μm ; e) 22000 cycles, $2c$ 211 μm ; f) 23000 cycles, $2c$ 247 μm ; g) 24300 cycles, $2c$ 330 μm ; h) 26300 cycles, $2c$ 566 μm and i) final fracture after 27664 cycles and $2c$ 819 μm	187
Figure 3.2.38	Evolution of the crack in the UNIVERSAL D2 sample loaded at $\Delta\sigma$ 990 MPa: a) at the last inspection of the surface (N 26300 cycles and $2c$ 566 μm) to b), c) and d) the moment when the sample broke (N 27664 cycles, $2c$ 819 μm and a 423 μm)	188

Figure 3.2.39	Crack propagation rate, da/dN , vs the stress intensity factor, ΔK , of the crack studied in the UNIVERSAL D2 sample.....	188
Figure 3.2.40	Stable crack growth in the UNIVERSAL D2 sample at $\Delta\sigma$ 990 MPa: a) 21000 cycles, $2c$ 27 μm ; b) 22000 cycles, $2c$ 29 μm ; c) 23000 cycles, $2c$ 29 μm ; d) 24300 cycles, $2c$ 32 μm ; e) 26300 cycles, $2c$ 37 μm and f) final fracture after 27664 cycles and $2c$ 44 μm	189
Figure 3.2.41	Crack propagation rate, da/dN , vs the stress intensity factor, ΔK , of the cracks studied in the UNIVERSAL D2 steel.....	190
Figure 3.2.42	Fatigue limit, in terms of σ^{max} , vs fracture strength of primary carbides, σ^{RC} , for the considered ingot cast tool steels in D2 and D3 configurations.....	191
Figure 3.2.43	Different forms of damage in the matrix of a 1.2379 D2 fatigue sample.....	192
Figure 3.2.44	Fatigue limit, in terms of σ^{max} , vs fracture strength of primary carbides and inclusions, σ^{RC} , for the ingot cast tool steels under D2 and D3 configurations and for HWS D2.....	194
Figure 3.2.45	Example of a fracture surface of an HWS fatigue sample in which an inclusion is the crack initiating site.....	194
Figure 3.2.46	Schematic description of flat and rising R-curves in terms of the driving force, K or J , vs the crack size, a [RIT08].....	197
Figure 3.2.47	Failure initiation site showing: a) “river markings”; b) the crack length at the surface delimited by a high plastically deformed zones a the fractured edge and c) the initial precracked carbide in which the final depth of the crack is difficult to be identified.....	198
Figure 3.2.48	Cracks observed at the surface of the UNIVERSAL D2 sample tested under monotonic loading and stopped before failure: a) crack number 1: $2c$ 192 μm ; b) cracks number 2 and 3: $2c$ 124 μm and 154 μm respectively, c) crack number 4: $2c$ 103 μm	199
Figure 3.2.49	Stepwise polishing results of crack number 1, from a) throughout h) sequence of crack images at increasing depths from the initial surface.....	200
Figure 3.2.50	Stepwise polishing results of cracks number 2-3, from a) throughout k) sequence of crack images at increasing depths from the initial surface.....	200
Figure 3.2.51	Stepwise polishing results of crack number 4, from a) throughout f) sequence of crack images at increasing depths from the initial surface.....	201
Figure 3.2.52	Geometry of cracks 1, 2-3 and 4 in terms of a (depth of the crack, or material removed at each polishing step) vs $2c$ (length of the crack, or measured length at each polishing step).....	201
Figure 3.2.53	Estimated geometry of cracks number 2 and number 3.....	203
Figure 3.2.54	Estimated R -curves considering different a/c ratios (0,3, 0,5 and 1) for the studied steels: a) 1.2379 D2 and b) zoom in 1.2379 D2; c) UNIVERSAL D2 and d) zoom in UNIVERSAL D2; e) K360 D2 and f) zoom in K360 D2; g) HWS D2 and h) zoom in HWS D2.....	206
Figure 3.2.55	Significance of the parameters of the Evans equation on the R -curve.....	207

Figure 3.2.56	<i>R</i> -curve plots with the experimental results of sections 3.2.3, 3.2.6.1 and 3.2.5.1 for a) 1.2379 D2, with the results of samples broken in section 3.2.3 (light grey dot with a/c 0,54) and section 3.2.5.1 (dark grey star with a/c 0,90); b) UNIVERSAL D2 with the results of samples broken in section 3.2.3 (light grey dots with a/c $0,75 \pm 0,07$) and section 3.2.6.1 (dark grey rhombi with: crack number 1 a/c 1, crack number 2-3 a/c 0,50 and crack number 4 a/c 0,41).....	208
Figure 3.2.57	Estimated <i>R</i> -curves considering different a/c ratios (0,3 – 0,5 – 1) for the studied steels: a) 1.2379 D3 and b) zoom in 1.2379 D3; c) UNIVERSAL D3 and d) zoom in UNIVERSAL D3; e) K360 D3 and f) zoom in K360 D3.....	210
Figure 3.2.58	Unstable fracture for different initial crack lengths, $2c_0$, and a/c ratios: a) 1.2379 D2 and $a/c = 0,5$; b) 1.2379 D2 and $a/c = 1$; c) UNIVERSAL D2 and $a/c = 0,5$; d) UNIVERSAL D2 and $a/c = 1$; e) K360 D2 and $a/c = 0,5$; f) K360 D2 and $a/c = 1$; g) HWS D2 and $a/c = 0,5$ and h) HWS D2 and $a/c = 1$	212
Figure 3.2.59	Unstable fracture for different initial crack lengths, $2c_0$, and a/c ratios: a) 1.2379 D3 and $a/c = 0,5$; b) 1.2379 D3 and $a/c = 1$; c) UNIVERSAL D3 and $a/c = 0,5$; d) UNIVERSAL D3 and $a/c = 1$; e) K360 D3 and $a/c = 0,5$; f) K360 D3 and $a/c = 1$..	213
Figure 3.2.60	Applied stress intensity factors for unstable fracture, K_R , vs the corresponding applied stresses, σ_r , considering different $2c_0$ values: a) for a/c 0,5 and b) for a/c 1	214
Figure 3.2.61	K_{IC} (E 399-90) in function of the <i>A</i> parameter: a) for a/c 0,5 and b) for a/c 1 (note that the K_{IC} value of K360 D3 was not calculated, in these diagrams it was assumed that it had the same value than in 1.2379 D3).....	215
Figure 3.3.1	Fracture by fatigue: a) when cracks are nucleated at the subsurface and grow to come to the surface and b) cracks initiated at surface flaws propagate inwards.....	216
Figure 3.3.2	Micro-chipping in PM steels: many cracks nucleate from broken carbides, decohesion at the carbide-matrix interface and in the metallic matrix; the cracks coalesce and grow to final fracture.....	217
Figure 3.3.3	a) Chipping; b) plastic deformation at the cutting edge and sinking in.....	217
Figure 3.3.4	a) Fracture due to the presence of threads; b) fracture due to machining grooves....	218
Figure 3.3.5	Wear related phenomena in tools: a) abrasive wear; b) adhesive wear; c) severe wear (abrasive + adhesive).....	218
Figure 3.3.6	Damage at the cutting edge: a) fracture and b) wear (adhesion of sheet metal and Al-Si material) in HS6-5-4 tools; c) cracks and d) abrasive wear at the surface of 1.3202 tools.....	219
Figure 3.3.7	Damage at the cutting edge: plastic deformation at a) VANADIS 4 EXTRA and b) HWS; c) breakage of VANADIS 4 B tool and d) loss of sharpness of HWS tools.....	220
Figure 3.3.8	a) Von Mises stresses determined by means of FE-simulation; corner of the B tool b) HS6-5-4, c) HWS, d) VANADIS 4 EXTRA and e) 1.3202.....	221
Figure 3.3.9	Broken carbides observed in the surface near the cutting edge: a) HS6-5-4 and b) 1.3202 tools.....	223
Figure 3.3.10	a) Schema of the studied zones at the B tool; b) variation of the area under the cutting edge for each zone after 2500 and 5000 strokes in HS6-5-4 and c) HWS...	224
Figure 3.3.11	Damage at the flank face of the HWS 62 HRC punch after 15000 strokes: a) zone 1; b) zone 2; c) zone 3; d) zone 4; e) zone 5 and f) zone 6.....	225

Figure 3.3.12	Damage at the flank face of the HWS 62 HRC punch after 9800 strokes: a) zone 1; b) zone 2; c) zone 3; d) zone 4; e) zone 5 and f) zone 6.....	225
Figure 3.3.13	Damage at the flank face of the HWS 62 HRC punch at its initial state: a) zone 1; b) zone 5 and c) zone 6.....	225
Figure 3.3.14	Damage at the flank face of the HWS 62 HRC punch after 40000 strokes: a) zone 4; b) zone 5 and c) zone 6.....	226
Figure 3.3.15	Damage at the flank face of the HWS 62 HRC punch after 65000 strokes: a) zone 1; b) zone 2; c) zone 3; d) zone 4; e) zone 5 and f) zone 6.....	226
Figure 3.3.16	Damage at the flank face of the HWS 62 HRC punch after 100000 strokes: a) zone 1; b) zone 2; c) zone 3; d) zone 4; e) zone 5 and f) zone 6.....	226
Figure 3.3.17	Damage at the flank face of the coated CrN-AlCrN HWS 62 HRC punch after 10000 strokes: a) zone 1; b) zone 2 (arrow number 1 shows adhered material and arrow number 2 shows the substrate tool steel); c) zone 3; d) zone 4; e) zone 5 and f) zone 6.....	227
Figure 3.3.18	Damage at the flank face of the coated CrN-AlCrN HWS 62 HRC punch after 30000 strokes: a) zone 1; b) zone 2; c) zone 3; d) zone 4; e) zone 5 and f) zone 6...	227
Figure 3.3.19	Von Mises stresses estimated in the punch by means of FE-simulation.....	228
Figure 3.3.20	Von Mises stresses at drawing tools determined by means of FE-simulation.....	229
Figure 3.3.21	Measured profiles in the drawing 240H tools radii after different numbers of strokes with TRIP800 and DP1000 2 mm thick.....	229
Figure 3.3.22	Measured profiles in the drawing 240A tools radii after different numbers of strokes with TRIP800 and DP1000 2 mm thick.....	230
Figure 3.3.23	Radius of the drawing tool at the initial state (blue line) and after 80000 strokes with TRIP800: HWS (yellow line) and 1.2379 (red line).....	230
Figure 3.3.24	Von Mises stresses registered in bending tools determined by FE-simulation.....	231
Figure 3.3.25	Tool radii profiles and deviation from the initial radius for 1.2379 (250A) and UNIVERSAL (250U): a) 250A tool 1; b) 250A tool 2; c) 250U tool 1; d) 250U tool 2.....	232
Figure 3.3.26	Adhesion of sheet material at the surface of the 250U tool number 2 after 4300 strokes with TRIP800 and 1500 with DP1000.....	233
Figure 3.3.27	Schema of the two types of punching tools: type 1 “922” punch, and type 2 “917” punches.....	233
Figure 3.3.28	Chipping evolution at the cutting edge of a 917A punch after: a) 200 strokes; b) 700 strokes (image of the flank face); c) 1500 strokes; d) 3100 strokes and e) 6100 strokes with TRIP800 2 mm thick.....	234
Figure 3.3.29	Damage observed in punches of different tool steels: plastic deformation in 917B after 4500 strokes; b) chipping in 917U after 4400 strokes and c) chipping in 917H after 4000 strokes with TRIP800 2 mm thick.....	234
Figure 3.3.30	Fatigue cracks (red arrows) observed in the flank face of a 917H punch. These cracks could have been nucleated from surface defects (shown by the blue arrow).	235
Figure 3.3.31	Damaging mechanisms observed in “922” punches: a) one of the semi-circular areas is almost fractured; b) and c) fractures by chipping and cracks at straight areas and d) plastic deformation and then chipping at the other semi-circular area of the punch.....	236

Figure 3.3.32	Cracks and fractures at “922” punches: a) and b) secondary and backscatter electron images of a 922A punch after 4600 strokes; c) and d) backscatter and secondary images of a 922B punch before and after fracture at 2000 and 4000 strokes respectively. All the images correspond to punching TRIP800 2 mm thick.	237
Figure 3.3.33	Fractures at a “917A” punch when punching DP1000 2 mm thick: a) after 500 strokes; b) after 1500 strokes and c) after 3500 strokes.....	237
Figure 3.3.34	Cracks identified after 1500 strokes near the cutting edge of: a) and b) a 917A punch; c) and d) a 917U punch and e), f) and g) 917H punch when punching DP1000 2 mm thick.....	239
Figure 3.3.35	Fractography of different punches: a) 922A at 1500 strokes; b) 922A at 3500 strokes; c) 922U at 3500 strokes; d) 922H at 500 strokes; e) 922H at 1500 strokes and f) 922H at 3500 strokes when punching DP1000 2 mm thick.....	240
Figure 3.3.36	Fracture mechanisms in punching DP1000 2 mm thick: a) 922A punch at 1500 strokes; b) 922U at 3500 strokes; c); d) and f) 922H at 3500strokes. The red arrows indicate the presence of cracks.....	241
Figure 3.3.37	Von Mises stress distribution and level in the punch. Stresses are confined in a narrow area near the cutting edge (600 μm) and the highest stresses are found below the surface.....	242
Figure 3.3.38	Von Mises stress distribution and level in the punch at the cutting edge.....	242
Figure 3.3.39	Fractography after 50 strokes: a) 1.2379A (fracture); b) 1.2379B (sinking); c) K360 (deformation and sinking); d) UNIVERSAL (-); e) HWS (deformation and sinking).....	243
Figure 3.3.40	Fractography of 1.2379A punch after: a) 50 strokes; b) 3000 strokes; c) 17000 strokes; d) 26000 strokes and e) 31000 strokes.....	244
Figure 3.3.41	a) Topographic image of the fracture at the cutting edge of the 1.2379A punch; b) FE-simulation results of von Mises stresses assuming a slant fractured edge and von Mises stress evolution with the penetration of the punch at points “1” and “2”; c) the same than b) but assuming a flat step fractured edge.....	245
Figure 3.3.42	a) Chipping of 1.2379 A punch along the machining grooves after 31000 strokes; b) wear at the flank face of the punch after 31000 strokes and c) cracks at the flank face of the punch after 31000 strokes.....	245
Figure 3.3.43	Cross sectional images of the punch cutting edge: 1.2379A after 31000 strokes; a) and b) carbides are broken at the subsurface of the cutting edge; c) cracks nucleated at the surface and propagating inwards and d) cracks nucleated at the subsurface from broken carbides and propagating outwards.....	246
Figure 3.3.44	Cross sectional images of the punch cutting edge: 1.2379A after 31000 strokes at different positions of the punch; a) cutting edge; b) rake face at the middle of the punch; c) flank face and d) punch inner position.....	247
Figure 3.3.45	Cracks in 1.2379B punch nucleated in broken carbides in the plastically deformed zone near the cutting edge after 3000 strokes.....	247
Figure 3.3.46	Fractography of 1.2379B punch after: a) 3000; b) 17000; c) 26000 and d) 31000 strokes.....	248
Figure 3.3.47	Fractography of 1.2379B punch: a), b) and c) cracks at the rake face after 2600 strokes; d) and e) wear, deformation and cracks at the flank face after 31000 strokes.....	248

Figure 3.3.48	Cross sectional images of the punch cutting edge: 1.2379B after 31000 strokes; a) carbides are broken at the subsurface of the cutting edge and a crack propagates through the microstructure; b) zoom of this crack; c) cracks and broken carbides below the rake face and d) shallow cracks nucleated at the flank face.....	249
Figure 3.3.49	Fractography of a K360 punch after 5000 strokes: a) wear at the cutting edge; b) and c) chipping at the highly worn areas and fracture following machining grooves.....	250
Figure 3.3.50	Fractography of an UNIVERSAL punch: a) wear after 3000 strokes; b) microcracks after 17000 strokes; c) small fractured area after 17000 strokes; d) chipping after 26000 strokes; e) wear at the flank face after 26000 strokes and f) cracks at the flank face parallel to the cutting edge.....	251
Figure 3.3.51	Cross sectional images of a UNIVERSAL punch after 26000 strokes; a) a few carbides are broken below the cutting edge; b) subsurface cracks at the flank face and material about to detach; c) subsurface cracks and broken carbides at the rake face and d) shallow cracks nucleated at the flank face.....	252
Figure 3.3.52	Fractography of an HWS punch: a) rounding of the cutting edge after 17000 strokes; b) wear at the surface after 17000 strokes; c) fractures by chippings at a previously sunk zone after 17000 strokes; d) the same zone than (c) but at 26000 strokes and e) new chipping at 26000 strokes.....	253
Figure 3.3.53	Fractography of the UNIVERSAL punch coated with W:C-H; flank face at 1500 strokes.....	253
Figure 3.3.54	Fractography of the HWS punch coated with W:C-H; flank face at 1500 strokes.....	254
Figure 3.3.55	Fractography of the UNIVERSAL (a, b) and c)) and HWS (d, e) and f)) punches coated with W:C-H; rake faces at 1500 strokes.....	254
Figure 3.3.56	Fractography of the UNIVERSAL punch coated with AlTiN; flank face after 5000 strokes.....	255
Figure 3.3.57	Fractography of the HWS punch coated with AlTiN; flank face after 5000 strokes.	256
Figure 3.3.58	Fractography of the a) UNIVERSAL; b) and c) HWS punches coated with AlTiN; rake face after 5000 strokes.....	256
Figure 3.3.59	Fractography of the UNIVERSAL punch coated with W:C-H; flank face after 5000 strokes.....	257
Figure 3.3.60	Fractography of the UNIVERSAL punch coated with W:C-H; rake face after 5000 strokes.....	257
Figure 3.3.61	Fractography of the HWS punch coated with W:C-H; flank face after 5000 strokes.....	258
Figure 3.3.62	Fractography of the HWS punch coated with W:C-H; rake face after 5000 strokes.....	258
Figure 3.3.63	Fractography of the rake face in UNIVERSAL W:C-H punch (a) throughout c)) and HWS – AlTiN punch (d) throughout f)) at 12000 strokes.....	259
Figure 3.3.64	The lateral compressive stresses state σ present in most PVD coatings generates interfacial stresses S . At the top of e.g. grinding ridges this stress is a tensile “lift off” stress that may reach the same order of magnitude as the residual stress σ	259
Figure 3.3.65	Von Mises stresses determined by means of FE-simulation in the HPC slitting tools. Slitting DP1000 2 mm thick with a clearance of 10 %.....	260

Figure 3.3.66	Location of the maximum stress in the upper blade during the slitting process of 22MnB5 1,75 mm thick with a cutting clearance of 15 %. Comparison between stress (dashed line) and load (solid line) in function of displacement [NOT10]...	261
Figure 3.3.67	Fractographic inspection of the 12379 upper and lower slitting tools.....	262
Figure 3.3.68	Fractographic images of the 1.2379 lower tool observed using SEM after a) 0 strokes; b) 8000 strokes and c) 22000 strokes.....	262
Figure 3.3.69	Fractography of the 1.2379 upper tool at increasing number of strokes: a) 16000; b) 22000; c) 26000; d) 31000 and e) 36000.....	263
Figure 3.3.70	Microstructural inspection of the cross section of 1.2379 slitting tools: a) lower tool at 22000 strokes; b) upper tool at 22000 strokes; c) lower tool at 36000 strokes and d) upper tool at 36000 strokes.....	264
Figure 3.3.71	Images of the flank face of the lower tool at 10000 strokes: a) 1.2379 and b) UNIVERSAL.....	265
Figure 3.3.72	Images of the flank face of the UNIVERSAL lower tool at 10000 strokes: a) low magnification image; b) zoom in the zone indicated in a) and c) backscattered image of b).....	265
Figure 3.3.73	Images of the flank face of the UNIVERSAL lower tool at 15000 strokes: a) to c) different increasing zooms of the same crack.....	265
Figure 3.3.74	Images of the rake face of the UNIVERSAL lower tool at 5000 strokes: a) general overview; b) and c) crack observed at the surface in a primary carbide.....	266
Figure 3.3.75	Images of the rake face of the UNIVERSAL lower tool at: a) 10000 strokes and b) 15000 strokes.....	266
Figure 3.3.76	Images of the flank face of the UNIVERSAL upper tool at: a) 0 strokes; b) 10000 strokes and c) 15000 strokes.....	266
Figure 3.3.77	Microstructural inspection of the cross section of UNIVERSAL slitting tools: a) lower tool at 15000 strokes and b) upper tool at 15000 strokes.....	267
Figure 3.3.78	Images of the flank face of the lower HWS tool at: a) 0 strokes; b) 10000 strokes and c) 15000 strokes.....	267
Figure 3.3.79	Images of the rake face of the lower HWS tool at: a) 10000 strokes and b) 15000 strokes.....	268
Figure 3.3.80	Microcracks at the flank face of the lower HWS tool at 10000 strokes.....	268
Figure 3.3.81	Microstructural inspection of the cross section of HWS lower tools at 15000 strokes.....	268
Figure 3.3.82	Images of the rake face of the UNIVERSAL lower tool with carbides aligned following the stroke direction at: a) 0 strokes; b) 5000 strokes and c) 15000 strokes.....	269
Figure 3.3.83	Microcracks at the flank face of the UNIVERSAL lower tool with carbides aligned following the stroke direction at: a) 10000 strokes and b) and c) 15000 strokes.....	269
Figure 3.3.84	Microcrack at the flank face of the UNIVERSAL lower tool with carbides aligned following the stroke direction at: a) 10000 strokes and b) 15000 strokes.....	270
Figure 3.3.85	Microstructural inspection of the cross section of UNIVERSAL lower tool with carbides aligned following the stroke direction at 15000 strokes.....	270

Figure 3.3.86	Topographic images obtained in CM of the flank face and R_a values of: a) 1.2379 tool; b) HWS tool; c) polished part of the new UNIVERSAL tool and d) as-grinded part of the new UNIVERSAL tool.....	271
Figure 3.3.87	SEM micrographies of the tools surface: a) and d) new UNIVERSAL as-grinded, after 5000 strokes; b) and e) new UNIVERSAL polished, after 5000 strokes and c) and f) 1.2379, after 8000 strokes.....	272
Figure 3.3.88	SEM micrographies of the tools surface: a) and d) new UNIVERSAL as-grinded, after 15000 strokes; b) and e) new UNIVERSAL polished, after 15000 strokes and c) and f) 1.2379, after 16000 strokes.....	273
Figure 3.3.89	Load – displacement curves of the punching processes using different clearances ranging between 2,5 % and 27,7 % of a) DP1000 2 mm thick; b) MS-W1200 2 mm thick and c) BORON-02 1,8 mm thick; d) maximum punching load plotted in function of the clearance for each of the studied steels.....	274
Figure 3.3.90	Schema of the punched sheet edge morphology of: a) DP1000 2 mm thick; b) MS-W1200 2 mm thick and c) BORON-02 1,8 mm thick for clearances between 2,5 % and 27,7 %.....	275
Figure 3.3.91	Load – displacement curves of the punching process of DP1000 2 mm thick with punch radii 10 and 100 μm and clearances: a) 2 %; b) 5%; c) 7,5 %; d) 10 %; e) 12,5 %; f) 15 %; g) 20 % and h) 25 %.....	277
Figure 3.3.92	Maximum von Mises stresses estimated by means of FE-simulation for 10 and 20 % clearance values, punch edge radii from 10 to 100 μm and considering BORON-02 1,8 mm thick, MS-W1200 and DP1000 2 mm thick.....	277
Figure 3.3.93	Comparison between the contact lengths at 15 % (SSP15) and 5 % (SSP5) clearance values and the effect on maximum von Mises stresses [NOT10].....	278
Figure 3.3.94	a) Comparison of sheet sheared edges obtained in punching BORON-02 1,8 mm thick, MS-W1200 and DP1000 2 mm thick, at clearances of 10, 15 and 20 % using sharp, rounded and damaged punch edges; b) damaged punch.....	279
Figure 3.3.95	Schema of the sheet edge after slitting: a) DP1000 2 mm thick; b) BORON-02 1,8 mm thick for ranging clearances between 5 and 20 %.....	280
Figure 3.3.96	Fractography of the 1.2379A punches after 3000 strokes: a) and b) sharp edge (radius 10 μm); c) and d) rounded edge (radius 100 μm).....	280
Figure 3.3.97	Fractography of the 1.2379A punches with 100 μm radius: a) and b) after 17000 strokes; c) and d) after 26000 strokes.....	281
Figure 3.3.98	Von Mises stress distribution and level near the cutting edge in the punch with 100 μm edge radius.....	282
Figure 3.3.99	Fractography of the lower 1.2379 tools: a) flank face of the tool with radius 500 μm after 22000 strokes; b) flank face of the tool with radius 10 μm after 8000 strokes; c) flank face of the tool with radius 10 μm after 22000 strokes; d) rake face of the tool with radius 500 μm after 22000 strokes; e) rake face of the tool with radius 10 μm after 8000 strokes and f) rake face of the tool with radius 10 μm after 22000 strokes.....	283
Figure 3.3.100	Fractography of the upper 1.2379 tools: a) and d) flank face of the tool with radius 500 μm after 22000 strokes; b) and e) flank face of the tool with radius 10 μm after 8000 strokes and c) and f) flank face of the tool with radius 10 μm after 22000 strokes.....	281

Figure 3.3.101	Load – displacement curves registered during tests in the instrumented slitting die using hardened 22MnB5 steel 1,5 mm thick. Loads in X and Z directions are plotted for cutting angles of 0° (red), 2° (blue), 7° (green) and 20° (orange) and cutting clearances of: a) 5% of the sheet thickness; b) 10 % and c) 15 %. Loads are normalised taking the sheet width into account (50 mm).....	285
Figure 3.3.102	Load – displacement curves registered during tests in the instrumented slitting die using hardened 22MnB5 steel 1,5 mm thick. Loads in X and Z directions are plotted for cutting angles of 0° (red), 2° (blue), 7° (green) and 20° (orange) and cutting clearances of: a) 5% of the sheet thickness; b) 10 % and c) 15 %. Loads are normalised taking the sheet width into account (50 mm).....	286
Figure 3.4.1	Comparison between the number of cycles, N , estimated through Equation 1.5.3 and the N determined experimentally for the fatigue samples: a) 1.2379, UNIVERSAL, K360 and HWS, all in D2; b) zoom in a) with 1.2379, UNIVERSAL and K360 results.....	287
Figure 3.4.2	Fracture initiating sites of the samples considered for this study, and in which the sizes of the initial carbide particles (dashed lines) are compared to the sizes of the clusters in which they are embedded (solid lines): a) to c) 1.2379; d) K360 and e) and f) UNIVERSAL.....	288
Figure 3.4.3	Comparison between the number of cycles, N , estimated through Equation 1.5.3 and the N determined experimentally for the fatigue samples: a) 1.2379, UNIVERSAL, K360 and HWS, all in D2; b) zoom of the squared region in a) with 1.2379, UNIVERSAL and K360.....	289
Figure 3.4.4	Comparison between the number of estimated cycles, N , both for nucleation and propagation of the crack observed in the UNIVERSAL sample analysed in section 3.2.5.2, considering the parameters of the Paris law determined for long cracks, and the parameters determined for this crack and shown in Table 3.2.12.....	290
Figure 3.4.5	Comparison between the number of estimated cycles, N , both for nucleation and propagation of the samples studied.....	291
Figure 3.4.6	Cumulative carbide size distribution and regression to $N_A(D)$ equation of the considered steels.....	292
Figure 3.4.7	a) Fracture probability, P_f , in function of the applied stress range, $\Delta\sigma$, estimated using the method developed by Meurling et al. and applied to 1.2379, UNIVERSAL, K360 and HWS; b) model fatigue limit vs experimental fatigue limit at $2 \cdot 10^6$ cycles.....	293
Figure 3.4.8	Cumulative inclusion size distribution and regression to $N_A(D)$ equation of inclusions in HWS.....	294
Figure 3.4.9	a) Fracture probability, P_f , in function of the applied stress range, $\Delta\sigma$, estimated using the method developed by Meurling et al. and applied to 1.2379, UNIVERSAL, K360 and HWS (green and orange curves considering carbides and inclusions as initiating particles in fatigue fracture); b) model fatigue limit vs experimental fatigue strength at $2 \cdot 10^6$ cycles (green triangle and orange star considering respectively carbides and inclusions as initiating particles in fatigue fracture).....	295
Figure 3.4.10	FE-simulation model for the punching process of the HPC in case of DP1000 2 mm thick: a) schema of the half cross sectional view of the punch in which the von Mises stresses at the moment when they are maximal are shown. Probability of failure determined at the same area and moment for a punch of b) 1.2379; c) UNIVERSAL; d) K360; e) HWS considering the particle distribution of carbides; f) zoom in image e); g) HWS considering the particle distribution of inclusions....	296

Figure 4.1.1	Examples of different types of defects observed in primary carbides: a)-b) holes in M_7C_3 carbides of 1.2379; c)-d) holes in M_7C_3 carbides of K360 and e)-f) non metallic particle at MC carbides of UNIVERSAL.....	300
Figure 4.1.2	Applied stress intensity factors for unstable fracture, K_R , vs the corresponding applied stresses, σ_r , considering the different $2c_0$ values: a) for a/c 0,5 and b) for a/c 1. Dashed lines indicate the estimated stress level in tools of 1500 MPa.....	304
Figure 4.1.3	Plot of σ^R , σ^{max} and σ^{RC} for the steels considered in this Thesis. The green and orange arrows indicate the nucleation and propagation stages of cracks under monotonic loading.....	306
Figure 4.1.4	Micro-mechanical properties of the metallic matrix: a) and c) Young's modulus and b) and d) hardness values.....	307
Figure 4.1.5	Schema of the stress-strain curves of carbides (red line), the matrix (black line) and to cases in which the properties of the matrix are reduced as a result of fatigue	309
Figure 4.2.1	Schema of the two processes studied in the HPC: punching and slitting, and the failure mechanism observed, i.e. fracture by chipping and micro-chipping.....	313
Figure 4.2.2	Main failure mechanisms observed in punching tools: a) schema of the punch to show that the image presented in Figures b) and c) corresponds to a view of the rake face; b) fractured cutting edge of a 1.2379A punch; c) topographic image of the fracture in the 1.2379A punch; d) cross sectional cut of the punch where many broken primary carbides are observed below the cutting edge.....	313
Figure 4.2.3	Damage observed at the microstructure of the punch through cross sectional cut, at the rake face and at distant positions from the cutting edge in direction to the centre. In a), b) c) and d) images, the existence of broken primary carbides is denoted with red arrows while blue arrows indicate cracks nucleated inside the material and propagating parallel to the surface.....	314
Figure 4.2.4	Damage observed at the microstructure of the punch through cross sectional cut, at the flank face and at distant positions from the cutting edge (around 1 mm). In a), b) c) and d) images, the existence of broken primary carbides is denoted with red arrows while blue arrows indicate cracks nucleated inside the material and propagating parallel to the surface.....	315
Figure 4.2.5	Strain levels in a deformed surface [STA05].....	316
Figure 4.2.6	Strain levels in a deformed surface and formation of a crack in the flank face of a 1.2379A punch. 1: very highly deformed material, 2: moderately deformed material and 3: bulk material, undeformed.....	316
Figure 4.2.7	Schematic illustration of the mechanism of material particle release due to growth of surface initiated cracks [STA05].....	317
Figure 4.2.8	Mechanism of material particle release in a 1.2379B punch: a) flank side and b) rake side of the punch.....	317
Figure 4.2.9	a) and b) cracks at the surface of a 1.2379A punch; c) example of fatigue wear reported by Stachowiak and Batchelor [STA05].....	317
Figure 4.2.10	Examples of fatigue cracks in a 1.2379B punch nucleated from surface released particles and propagating in direction to the interior of the tool.....	318
Figure 4.2.11	Examples of fatigue cracks in a UNIVERSAL punch nucleated from surface released particles and propagating in direction to the interior of the tool.....	318
Figure 4.2.12	Illustration of a process of subsurface crack formation by growth and link up of voids [STA05].....	319

Figure 4.2.13	Cohesion of cracks number 1 and 3 (nucleated at the surface) to a crack nucleated below the surface from a broken primary carbide (number 2) in a 1.2379B punch..	319
Figure 4.2.14	Schematic illustration of the process of surface crack initiation and propagation [STA05].....	320
Figure 4.2.15	Process of surface crack initiation and propagation observed in the 1.2379B punch.....	320
Figure 4.2.16	Schematic description of the different stress sates acting at the punch cutting edge.....	321
Figure 4.2.17	Image of the flank face in a 1.2379B punch where fractures at the cutting edge can be observed, as well as cracks propagating parallel to the surface (indicated by red arrows).....	322
Figure 4.2.18	Summary of the different types of damage observed in punching tools of the HPC.	323
Figure 4.2.19	Cracks at the microstructure of the 1.2379 lower tool in a cross sectional analysis..	326
Figure 4.2.20	Crack parallel to the flank face due to “wave” formation (mechanism 1A in previous Figure 4.2.18); b) broken carbides present cracks in vertical direction, also below the rake face (in contrast to mechanism 1B in Figure 4.2.18).....	327
Figure 4.2.21	Schematic illustration of the FE-model to characterise residual stresses in the microstructure at the micro scale.....	329
Figure 4.2.22	Stress distribution in the upper and lower tools in X- direction.....	330
Figure 4.2.23	Stress distribution in the upper and lower tools in Y- direction.....	330
Figure 4.2.24	Von Mises stresses registered once the compressive loads defined in Figure 4.2.21 are released: a) corresponds to the results obtained with the configuration shown in Figure 4.2.21 a); b) corresponds to the results obtained with the configuration shown in Figure 4.2.21 b); c) corresponds to the results obtained with the configuration shown in Figure 4.2.21 c); d) corresponds to the results obtained with the configuration shown in Figure 4.2.21 a); e) von Mises stresses during the application of a tensile stress of 1000 MPa (Figure 4.2.21 e)).....	331
Figure 4.2.25	Stresses registered once the compressive loads defined in Figure 4.2.21 b) and c) are released: a) corresponds to the stresses in X- direction (S11) obtained with the configuration shown in Figure 4.2.21 c); b) corresponds to the stresses in Y- direction (S22) obtained with the configuration shown in Figure 4.2.21 c); c) corresponds to the stresses in X- direction (S11) obtained with the configuration shown in Figure 4.2.21 d); d) corresponds to the stresses in Y- direction (S22) obtained with the configuration shown in Figure 4.2.21 d).....	332
Figure 4.2.26	Detail of Figure 4.2.24 c) in which directions of maximum stresses are illustrated, and they correlate to the direction of the cracks nucleated at primary carbides in lower tools.....	332
Figure 4.2.27	Broken primary carbides near the cutting edge of the upper 1.2379 tool, red arrows denote cracks nucleated because carbides present defects (encircled in red)	333
Figure 4.2.28	Schema of the parameters assumed to estimate ΔK at broken primary carbides of lower tools according to the carbide configuration.....	334
Figure 4.2.29	Cracks nucleated at the rake face of the upper tools.....	335
Figure 4.2.30	Cracks nucleated at the flank face of a lower 1.2379 tool at 8000 strokes.....	335
Figure 4.2.31	Cracks nucleated at the flank face of a lower 1.2379 tool at 36000 strokes.....	336

Figure 4.2.32	Fractures at the cutting edge in views from: a) and b) the rake face of the tool; c) and d) the flank side of the tool and e) cross sectional image.....	336
Figure 4.2.33	Cracks at the rake face of a 1.2379 lower tool near the cutting edge.....	337
Figure 4.2.34	Cross sectional images of the cutting edge of two 1.2379 lower tools, dashed white lines denote the location of cracks nucleated at the flank face: a) after 36000 strokes and b) after 22000 strokes.....	337
Figure 4.2.35	SCF crack results: a) top view of first ring/cone crack; b) top view of second ring/cone crack; c) initial ring/cone cracks formation and d) cut view of lateral crack [ALF01].....	338
Figure 4.2.36	Several circumferential cracks are observed near fractures at the cutting edge of 1.2379 lower tools (in correspondence with Figure 4.2.34 b)).....	339
Figure 4.2.37	Lateral cracks in SCF samples resemble cracks nucleated at the flank face of tools: a) Figure 4.2.34 d) from Alfredsson and Olson [ALF01] and b) cut view of an HWS tool.....	339
Figure 4.2.38	Principal stress distribution at $P = 13,4$ kN and after unloading: a) σ_{zz} and $\sigma_{\varphi\varphi}$ along the symmetry line and b) σ_{rr} and $\sigma_{\varphi\varphi}$ along the surface [ALF01].....	340
Figure 4.2.39	a) A small crack emanating from the root of a notch [FET08]; b) small crack emanating from a grinding groove in an HWS lower tool.....	340
Figure 4.2.40	Summary of the different types of damage observed in the slitting tools of the HPC.....	342
Figure 4.3.1	Schematic illustration of the different types of chippings registered empirically in basis of the long experience of the tool steel manufacturer (adapted from knowledge given by ROVALMA.....	346
Figure 4.3.2	An example of fracture at the cutting edge of punches where similarities to Figure 4.3.1 a) can be observed: a) at the rake face and b) at the flank face.....	348
Figure 4.3.3	An example of fracture at the cutting edge of slitting tools where similarities to Figure 4.3.1 b) can be observed: a) at the rake face; b) at the flank face and c) in cross section.....	348
Figure 4.3.4	Evolution of E in HWS punches after: a) 0; b) 15000; c) 40000 and d) 10000 strokes.....	351
Figure 4.3.5	Indentations in HWS punch samples after 40000 strokes: a), b) and c) near from the cutting edge where E shows the lowest values (plastic deformation and decohesion of carbides is shown in red arrows); d) far from the cutting edge where E is higher (no damage is observed).....	352

List of tables

Table 2.1.1	Main alloying elements in the chemical composition of the studied steels (in wt %).	111
Table 2.1.2	Heat treatment applied to the studied materials and obtained hardness level.	112
Table 2.5.1	Summary of the shearing tests studied in industrial conditions.	122
Table 2.5.2	Chemical composition of the tool materials (in wt %).	122
Table 2.5.3	Heat treatment applied to the studied materials and obtained hardness.	122
Table 2.5.4	Mechanical properties of MS-W1200 determined by means of tensile tests.	127
Table 2.5.5	Heat treatment applied to the punches and attained hardness level.	130
Table 2.5.6	Mechanical properties of TRIP800 and DP1000 determined by means of tensile tests.	131
Table 2.5.7	Heat treatment applied to the studied materials and obtained hardness.	132
Table 2.5.8	Name, material, coating type and total number of strokes of the coated punches used in the HPC.	133
Table 2.5.9	Summary of the system conditions and parameters used in the FE-simulations.	138
Table 3.1.1	Structure, amount in the microstructure and chemical composition (in wt %) of the primary alloy carbides in 1.2379, K360, UNIVERSAL and HWS.	140
Table 3.1.2	Mean carbides size and geometry in terms of ECD , D_{min} , D_{max} , AR , ψ and SF in 1.2379, K360, UNIVERSAL and HWS.	142
Table 3.1.3	Classification of secondary carbides in UNIVERSAL steel.	146
Table 3.1.4	Chemical composition (in wt %) of the matrix in 1.2379, K360, UNIVERSAL and HWS.	147
Table 3.2.1	Weibull parameters, m and σ_0 .	149
Table 3.2.2	Fatigue sensitivity expressed in terms of the ratio between $\Delta\sigma^{fat}/\sigma^R$.	152
Table 3.2.3	Fitting parameters of the Paris curve A and m .	161
Table 3.2.4	Mechanical properties of the primary carbides in 1.2379, UNIVERSAL and K360: Young's modulus, E , hardness, H , and fracture toughness, K_C .	162
Table 3.2.5	Mechanical properties of the metallic matrix in 1.2379, UNIVERSAL and K360: Young's modulus, E , hardness, H .	163
Table 3.2.6	Fracture strength of the primary carbides, σ^{RC} , in 1.2379, UNIVERSAL and K360 D2 and D3.	164
Table 3.2.7	Fracture strength of inclusions and primary carbides, σ^{RC} , in HWS D2.	173
Table 3.2.8	ΔK of the three cracks in Figure 3.2.31, assuming a/c ratios of 1, 0,5 and 0,3.	182
Table 3.2.9	ΔK of the three cracks in Figure 3.2.32, assuming a/c ratios of 1, 0,5 and 0,3.	183
Table 3.2.10	ΔK of the three cracks in Figure 3.2.33, assuming a/c ratios of 1, 0,5 and 0,3.	183
Table 3.2.11	Shape of carbides at the failure initiation sites of fatigue samples and corresponding ΔK values.	184

Table 3.2.12	Fitting parameters of the Paris curve A and m for the different cracks studied.....	190
Table 3.2.13	Shape of initiating inclusion particles and corresponding ΔK values in HWS fatigue samples.....	195
Table 3.2.14	Local applied stress, σ_a , length of the crack at the surface, $2c$, its total depth, a , the corresponding a/c ratio and the calculated applied stress intensity factor, K_a , for each one of the cracks studied.....	202
Table 3.2.15	Length of the crack at the surface, $2c$, its total depth, a , the corresponding a/c ratio for cracks number 2 and 3.....	202
Table 3.2.16	Parameters of the Evans equation, K_0 , C_1 and C_2 , for the four considered steels in D2 configuration and for a/c equal to 0,3, 0,5 and 1.....	206
Table 3.2.17	Parameters of the Evans equation: K_0 , C_1 and C_2 , for the considered ingot steels in D3 configuration and for $a/c = 0,3, 0,5$ and 1.....	201
Table 3.4.1	Applied stress, $\Delta\sigma$, and initial, a_0 , and final, a_f , crack sizes measured at the fracture surfaces of some of the samples tested in fatigue ($\Delta\sigma$ in MPa, a_0 and a_f in μm).....	287
Table 3.4.2	$N_A(D)$ fitting constants (Equation 1.5.7) of the cumulative carbide size distribution.....	292
Table 4.1.1	K_{IC} (E 399-90), estimated K_R at 1500 MPa and the difference calculated between these two for the studied steels under D2 and D3 configurations and for a/c 0,5 and 1.....	304
Table 4.1.2	Monotonic and cyclic properties of selected engineering alloys [HER83], page 499.....	309
Table 4.1.3	Applied stress amplitude, $\Delta\sigma$, number of cycles to failure, N , initial carbide size, a , and corresponding applied stress intensity factor, ΔK , of the samples of K360 D2 broken in fatigue.....	312
Table 4.2.1	Estimated ΔK of cracks at broken primary carbides.....	334

List of symbols

a	Depth of a crack below the surface.
a_0	Initial depth of a crack below the surface.
a_f	Final depth of a crack below the surface.
A	Material constant in the Paris equation.
$A_{Carbides}$	Area occupied by carbides.
ACP	Average Carbide Percentage.
AR	Aspect ratio.
A_{Total}	Total area.
c	Half length of a crack at the surface.
c_0	Initial half length of a crack at the surface.
d	Characteristic length of dislocations.
da/dN	Fatigue crack growth rate.
D	Equivalent particle diameter in the model of Meurling et al.
D_c	Critical equivalent particle diameter.
DCR	Diameter of the crack in the cluster.
D_{max}	Maximum carbide diameter.
D_{min}	Minimum carbide diameter.
E	Young's modulus.
E_{max}	Maximum Young's modulus.
E_{min}	Minimum Young's modulus.
ECD	Equivalent carbide diameter.
f	Fitting constant of N_A equation.
f_c	Critical volume fraction of carbide phase.
F_H	Horizontal resulting force in the cutting edge.
F_{RS}	Lateral force.
F_S	Shearing force.
F_{Smax}	Maximum force to shear a metal.
F_V	Vertical resulting force in the cutting edge.
H	Hardness.
H_{max}	Maximum hardness value.
H_{min}	Minimum hardness value.
i	Number of image.
k	Fitting constant of N_A equation.
K	Stress intensity factor.

K_a	Applied stress intensity factor.
K_C	Fracture toughness.
K_{IC}	Plane strain fracture toughness in mode I.
K_{max}	Maximum applied stress intensity factor.
K_{min}	Minimum applied stress intensity factor.
K_{op}	Crack opening stress intensity factor.
K_R	Stress intensity factor at which unstable fracture takes place.
K^{0°	Stress intensity factor at 0° with respect to the sample surface.
K^{90°	Stress intensity factor at 90° with respect to the sample surface.
L	Dislocation obstacle spacing.
m	Material constant in the Paris equation.
m	Weibull modulus.
M	Bending moment in the cutting edge.
n	Number of critical defects.
N	Number of fatigue cycles.
N_A	Cumulative size distribution of carbides or inclusions.
p	Probability of finding a certain number of critical defects in a volume of material.
P	Weibull probability of failure.
P_f	Fracture probability.
r	Distance from the crack tip.
r_p	Radius of dislocation shearable particles.
r_{pc}	Critical radius of dislocation shearable particles.
r_y	Plastic zone size.
R	Material resistance to fracture.
R	Ratio between the minimum to the maximum stress or load.
R_a	Roughness.
s	Size of carbides in a cluster.
SF	Shape factor.
$S11$	Stress in X-direction.
$S22$	Stress in Y-direction.
V	Volume of material.
Y	Geometrical correction factor.
α	Cutting angle.
Δa	Stable crack growth increment.
ΔK	Stress intensity factor range.
ΔK_{TH}	Fatigue crack propagation threshold.
$\Delta\sigma$	Stress amplitude.

$\Delta\sigma^{fat}$	Fatigue limit.
ε^{msoft}	Strain value of the softened matrix at σ^{max} .
ε^{RC}	Strain at which carbides fail.
λ_C	Critical defects in a volume of stressed material.
ν	Poisson's ratio.
σ	Stress.
σ_a	Applied stress.
σ_a^{max}	Maximum applied stress.
σ^{max}	Fatigue limit in terms of the maximum stress.
σ^r	Stress corresponding to unstable failure.
σ^R	Fracture strength.
σ^{RC}	Fracture strength of primary carbides.
σ_y	Yield stress.
σ_0	Weibull reference strength.
τ	Shearable particle cutting stress.
ψ	Sphericity.

List of abbreviations

AE	Acoustic Emission.
AHSS	Advanced High-Strength Steels.
AIN	Asociación de la Industria Navarra.
AISI	American Iron and Steel Institute.
AlTiN	Aluminium titanium nitride coating.
ASTM	American Society for Testing Materials.
at. %	Atomic percentage.
CM	Confocal Microscope.
CNRS	Centre National de la Recherche Scientifiques.
CP	Complex Phase.
CTM	Fundació CTM Centre Tecnològic.
CVD	Chemical Vapour Deposition.
DIN	Deutsches Institut für Normung.
DP	Dual-Phase.
D1	Sample with the major axis oriented perpendicular to the forging direction.
D2	Sample with the major axis oriented parallel to the forging direction.
D3	Sample with the major axis oriented transverse to the forging direction.
EAF	Electric Arc Furnace.
EBS	Electron Back Scatter Diffraction.
EDS	Energy Dispersive X-ray Spectrometry.
EDM	Electro Discharge Machining.
EDX	Energy Dispersive X-ray Spectrometry.
ESR	Electroslag Remelting.
EURO NCAP	European New Car Assessment Programme.
FE	Finite Element.
FEM	Finite Element Modelling.
FE-SEM	Field Emission Scanning Electron Microscope.
FORMA0	Nuevos procesos de conformado y desarrollo de materiales avanzados para la transformación de aceros de alta resistencia mecánica.
GBA	Granular Bright Area.
GBF	Granular Bright Facet.
HIP	Hot Isostatic Pressing.
HPC	Herramienta de Punzonado Continuo.
LCF	Low Cycle Fatigue.

JIS	Japanese Industrial Standards.
LEAM	Laboratory d'Enginyeria Acústica i Mecànica.
LEFM	Linear Elastic Fracture Mechanics.
LOM	Light Optical Microscope.
MDA	Matriu de Dany Accelerat.
MS	Martensitic Steels.
M-steels	Molybdenum high-speed tool steels.
MTEC	Matriz de Tolerancia y Esfuerzos de Corte.
MTEC-p	Matriz de Tolerancia y Esfuerzos de Corte (for punching).
MTEC-s	Matriz de Tolerancia y Esfuerzos de Corte (for slitting).
PHS	Press Hardened Steels.
PM	Powder Metallurgy.
PSB	Persistent Slip Band.
PVD	Physical Vapour Deposition.
SCF	Standing Contact Fatigue.
SEM	Scanning Electron Microscope.
S-N	Stress - number of cycles.
TEM	Transmission Electron Microscopy.
TUM	Technische Universität München.
TRIP	Transformation Induced Plasticity.
T-steels	Tungsten high-speed tool steels.
UHSS	Ultra High-Strength Steels.
UMR	Unité Mixte de Recherche.
UTG	Lehrstuhl für Umformtechnik und Gießereiwesen.
VAR	Vacuum Arc Remelting.
VHCF	Very High Cycle Fatigue.
W:C-H	Carbonic hydrogenated doped with tungsten coating.
WDS	Wavelength Dispersive X-ray Spectroscopy.
wt. %	Weight percentage.

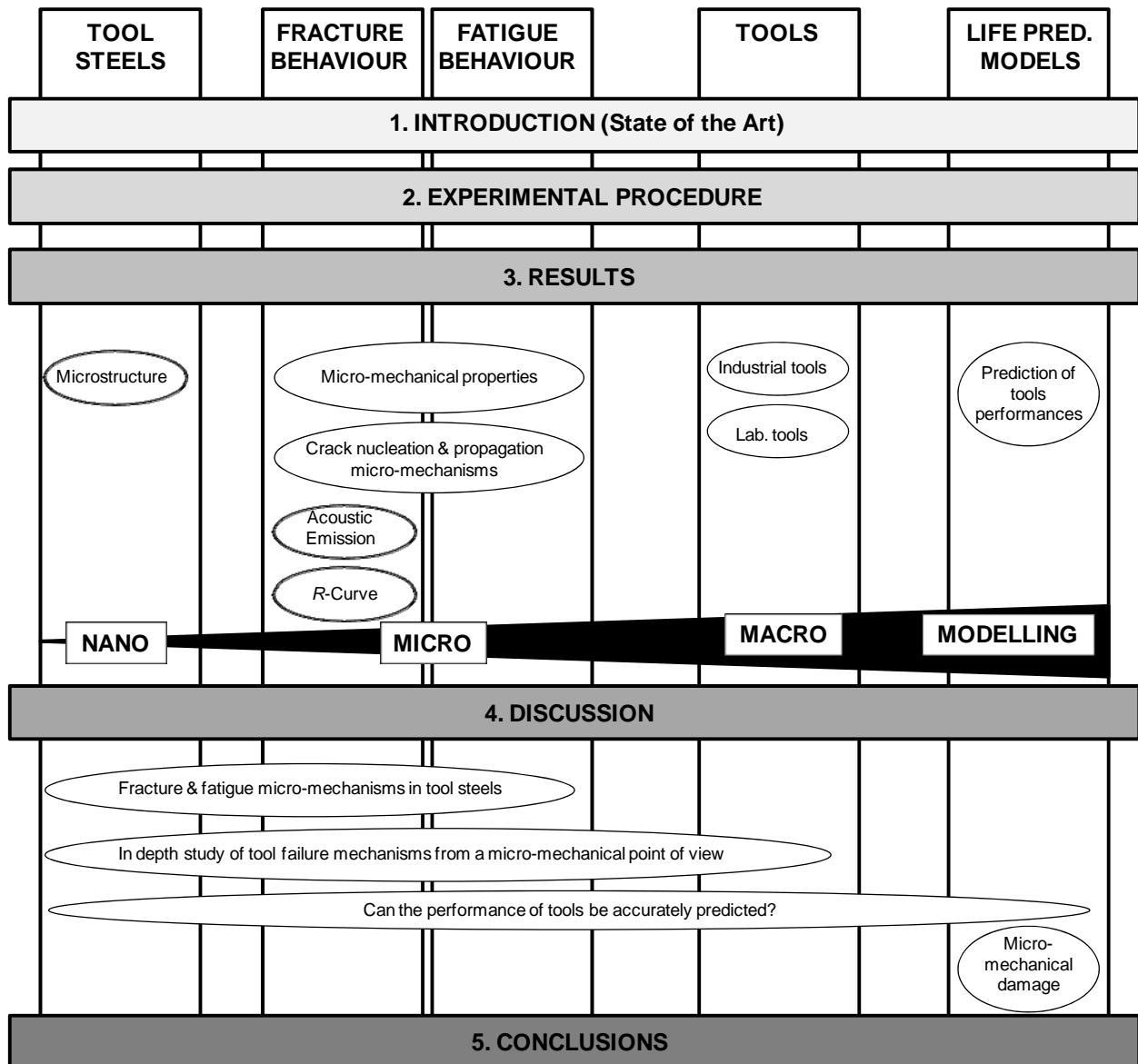
Preface

The structure of this Thesis has been organised in five main topics: tool steels, fracture behaviour, fatigue behaviour, tools and life prediction models. The information is presented in the classical form, i.e. “Introduction” (containing the state of the art), “Experimental Procedure” (describing the experimental materials, equipments and protocols), “Results” (presenting the main results of the study), “Discussion” (discussing the results obtained and relating each of the five aforementioned topics to each other and to relevant literature) and “Conclusions” (concluding the most important findings of the investigation).

The first of the main pillars of the Thesis, tool steels, concerns an in-depth study of their microstructure. The second and the third consist in fracture and fatigue behaviours and in them the macro-mechanical properties of tool steels are determined, as well as the crack nucleation and propagation processes from a micro-mechanical point of view, including *R*-curve behaviour. To help characterising the fracture behaviour of tool steels, Acoustic Emission (AE) tests are performed as well. Regarding the topic of tools, an exhaustive analysis of tools has been done in the industry and at laboratory scale. Finally the last of the topics consists in the evaluation of LEFM based models to predict the life of tools.

These five main pillars of the Thesis permit to study tool steels from the nano- to the micro- and macro-points of view, studying the intrinsic properties and microstructural constituents of different tool steels, the interrelations amongst them under monotonic and cyclic loads to explain the nucleation and propagation of microcracks, and finally to rationalise their performance in tools. At the end of this increasing scale pyramid, it is aimed at relying and rationalising the behaviours of tool steels at the three levels as an approach to a model to predict tool lives. Hence, based on the fracture and fatigue micro-mechanisms of tool steels, the study of the failure mechanisms of tools from a micro-mechanical point of view, and the evaluation of the adequacy of existing methods to predict tool lives, a model based on micro-mechanical damage is introduced in this Thesis.

A summary of the content of the Thesis is given below:



Finally, I would like to say that the present Thesis should be understood as forming part of a well established research initiated at Fundació CTM Centre Tecnològic and the department of Ciència dels Materials i Enginyeria Metal·lúrgica de la Universitat Politècnica de Catalunya, in which multiple national and European projects as well as PhD. Thesis are inscribed.

Ingrid Picas

Manresa, September 2012

Motivation: objectives

Moving towards a more sustainable society is one of the main challenges to be overcome by the automotive industry. The European Commission has already outlined its plans for a new Community Strategy that enables to reach the EU objective of reducing CO₂ emissions from new passenger cars to 120 g/km in 2012. Nevertheless, a long term target of 95 g/km is specified for the year 2020. To bridge the gap between the current average new car fleet and the 120 g/km goal, an integrated approach includes setting minimum efficiency requirements in vehicles. Several options are identified as contributing to the potential decrease of CO₂ emissions or providing alternative reduction routes. These options are the advanced reduction of engine friction losses, the extra strong downsizing with turbo charging (the same power is generated with a smaller swept volume engine), the heat recovery (heat conversion into mechanical or electrical power) and the application of advanced lightweight materials within vehicles [SHA09].

Besides the environmental regulation towards low CO₂ emission targets, the design and manufacture of new vehicles must also be done in regard to a safety performance enhancement. The EURO NCAP (European New Car Assessment Programme) is steadily implementing new and more rigorous crash tests to preserve the driving force on the market for future improvements, and protecting the consumer interest according to the real world and societal priorities, legislative developments, technical feasibility of new protocols and costs of implementation [VAN08].

Thus, on account of the environmental and safety related requirements, the majority of the most popular automotive manufacturers convey to introduce Ultra High Strength Steels (UHSS) and Press Hardened Steels (PHS) in the vehicle body-in-white. UHSS and PHS owe a steady broadening in automotive applications to the fact that parts made of these steels bring together high rigidity, high energy absorption capacity and light weight. UHSS and PHS include several families of steels whose main peculiarity lies in their multiphase microstructure, in which ferrite, martensite, bainite and/or retained austenite are combined to provide unique mechanical properties; i.e. extremely high strength and relative good ductility and elongation.

Nevertheless, the real success of UHSS and PHS parts implementation into the upcoming automobiles is being so far restricted by their harsh cold forming and post forming operations, e.g. shearing. On the one hand, UHSS show critical elastic recovery phenomena after being shaped and complex geometries are difficult to be obtained. In addition, their high yield stress leads to accelerated damage in forming tools. On the other hand and although press hardening emerged to produce high functional and performance parts with good dimensional stability and more complex shapes, hard cutting of PHS parts stands as great handicap of their manufacturing process. Hard cutting using conventional mechanical means is extremely

arduous indeed to be applied in such high strength steels. However and despite the major improvement of the laser cutting technology, it stays as an alternative but rather unattractive procedure involving larger time at more elevated cost expenses for mass production manufacturing.

In the frame that typical cold forming and post forming strategies and tool materials are no longer able to provide solutions to the formerly explained awkwardness, a new approach needs to be undertaken. For this purpose, the ongoing investigations are focused on adjusting the process parameters and developing new and high performance tool steels. Previous to the introduction of UHSS and PHS, cold forming and post forming tools failure was usually attributable to wear after high number of strokes. However, the high loads required in case of UHSS and PHS do not only accelerate wear mechanisms, but also generate elevated stresses which lead to plastic deformation or premature fracture of tools. Wear phenomena can be reduced using high hardened tools, applying special surface treatments and/or hard coatings; but a further increase of hardness brings about drastic decrease in toughness and detrimental brittleness. Therefore, tool materials require the maximum hardness – toughness relationship so as to face up to such severe mechanical solicitations.

High-speed steels and high-carbon, high-chromium steels are traditionally employed in forming or cutting tools due to their high wear resistance. The high carbon and alloy content produce large volume fractions of high hardness alloy carbides (primary carbides), which are the responsible for such high wear resistance. However, their highly alloyed chemical composition gives these carbides relatively low toughness [ROB98]. The hardening of such tool steels is based on a martensitic phase transformation, achieved by subsequent multiple tempering. During tempering, several structural changes take place, in particular the precipitation of fine nanometer-sized alloy carbides (secondary hardening carbides) [EBN01]. Therefore, the performance of tool steels during cold forming and shearing applications depends on the mechanical properties resulting from the complex interaction between the hard particles and the tempered martensite matrix where they are embedded.

From this standpoint, the aim of the present Thesis is to determine the relationship between the microstructure and the mechanical behaviour of tool steels for cold forming and shearing operations of UHSS and PHS. In order to reach this goal, the following objectives arise:

- 1- Improve the microstructural design of tool steels as well as the performance of tools.
- 2- Scrutinise the microstructure of tool steels and ascertain the micro-mechanical properties of each microstructural constituent, as well as their role in crack nucleation and propagation processes under monotonic and cyclic loading conditions. Evaluate *R*-curve behaviours in tool steels.
- 3- Determine the relationship between tool steel microstructures and damaging mechanisms.

- 4- Assess the mechanical behaviour of tool steels and rationalise their performance in basis of a micro-mechanical point of view.
- 5- Characterise the damaging mechanisms acting in tools during cold forming and shearing processes of UHSS and PHS. Identify and quantify different types of damage and understand the micro-mechanical processes involved in the failure events taking place in tool steels. Rationalise the results in view of different operational features such as the level of applied loads, contact pressures, surface conditions, clearances, etc.
- 6- Determine the adequacy of existing models based on Linear Elastic Fracture Mechanics (LEFM) to predict tool performances. Detect their limits of application and the requirements to estimate the life of tools with increased accuracy.
- 7- Introduce a new approach to predict tool lives based on micro-mechanical damage.

1. Introduction

1.1 Tool steels for cold forming and shearing applications

Tool steels for cold forming and shearing applications include high-speed and high-carbon, high-chromium steels. High-speed tool steels were developed for high speed cutting and machining processes where high hardness levels were required at high temperatures. They can be divided into two main categories: T-steels and M-steels, depending on their content in tungsten and molybdenum respectively. Due to their relatively high carbon and very high alloy contents, they have high hardenability and are processed to develop microstructures with large volume fractions of high-temperature stable carbides, which create excellent wear resistance and red hardness. Despite in M-steels molybdenum replaces some of the tungsten of the T-steels, they have similar performance characteristics; except for the slightly higher toughness of the molybdenum steels.

High-carbon, high-chromium cold-work tool steels in turn, have extremely high wear and abrasion resistance. Not only is tempered high-carbon martensite an important component of the microstructure, but large volume fractions of alloy carbides also play an important role in achieving high wear resistance. Some of the alloy carbides are produced by solidification and coexist with austenite during hot working and austenitizing, and some are produced by tempering. Chromium, at a nominal concentration of 12 % is the major alloying element, but molybdenum, vanadium, nickel, manganese, tungsten and cobalt may be added in significant amounts to this type of steels.

Solidification of the high-chromium cold-work tool steels causes considerable segregation of alloying elements. The first crystals to solidify are richest in iron, and carbon, chromium, and other elements are rejected to interdendritic or intercellular liquid regions where the alloy carbides eventually form. Hot work breaks up the segregated solidification structure, but because the alloy carbides are stable during high-temperature hot working, they are elongated by the hot work, and they are dispersed forming bands oriented along with the forging direction (Figure 1.1.1 a)). Dispersion of finer spheroidized secondary carbides also exists as a result of the tempering heat treatment after quenching (Figure 1.1.1 b)). The matrix consists, in turn, of tempered martensite and some retained austenite.

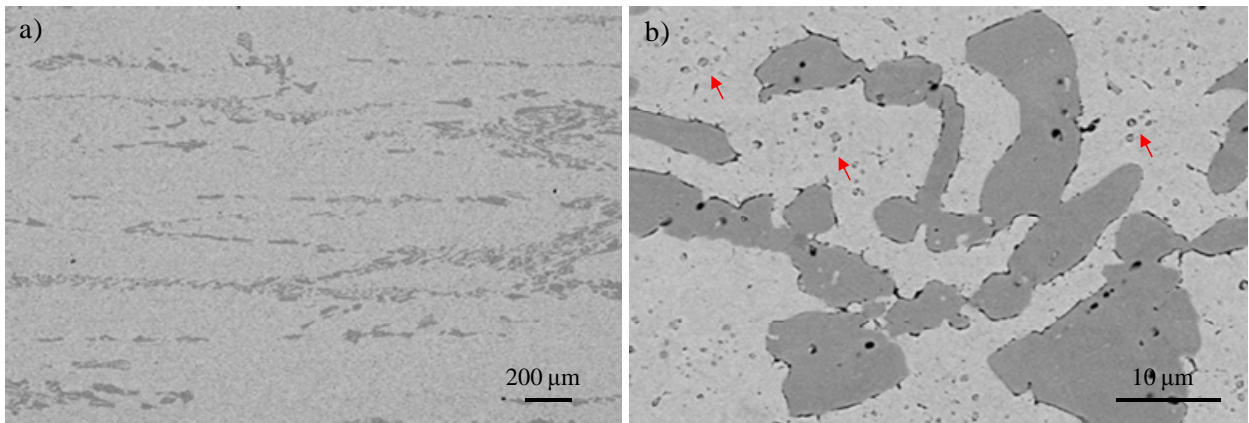


Figure 1.1.1 a) Primary carbides are elongated after hot working and they are dispersed forming bands oriented along with the rolling direction; b) spheroidized secondary carbides (small red arrows) coexist in the martensite matrix

The toughness and fracture resistance of hardened high-carbon, high-chromium cold-work tool steels is relatively low (around $15 - 30 \text{ MPa}\cdot\text{m}^{1/2}$). In the as-quenched condition, low toughness is caused by a microstructure consisting of high-carbon martensite and a high density of coarse, undissolved carbides, which serve as fracture initiation sites. Tempering increases toughness and plasticity of the martensite. However, tempering causes the transformation of retained austenite, which introduces additional carbides at various stages of tempering and may increase the sensitivity to fracture.

1.1.1 Manufacturing methods of tool steels

The manufacturing process dictates important aspects of the microstructure of tool steels, which controls, in turn, the performance characteristics. Some of the most employed manufacturing techniques include conventional ingot metallurgy routes, electric arc furnace (EAF), electroslag remelting (ESR) or vacuum arc remelting (VAR) amongst others [ROB98]. The use of ESR or VAR techniques has substantially improved the as-cast structures by producing more uniform macrostructures with less segregation tendency, increased cleanliness and no porosity. Hot working, forging or rolling, are then followed not only to achieve the required final shape and dimensions but also to improve the properties of the alloy and thus, the performance of the final tool. That is accomplished by refining the grain size and carbide distribution. After hot working, forged or rolled bars usually must be annealed to avoid the danger of cracking in machining, grinding or reheating for further work.

However, perhaps the most significant improvement in the manufacturing methods has been the application of powder metallurgy (PM) for production of the most highly alloyed steels. The slow cooling of the conventional static cast ingot allows the formation of coarse eutectic carbide structures, which are difficult to break down during hot working and produce nonuniform microstructures with marked

anisotropy (as shown in Figure 1.1.1 a). Contrarily, PM tool steels show fine and uniform distribution of carbides as a result of rapid solidification during atomization (Figure 1.1.2). Hot isostatic pressing (HIP) is the most common consolidation technique applied in PM tool steels. Since full density can be achieved by HIP, following working is not necessary even though billets produced by HIP are often hot worked by a combination of forging and rolling, depending on final product size.

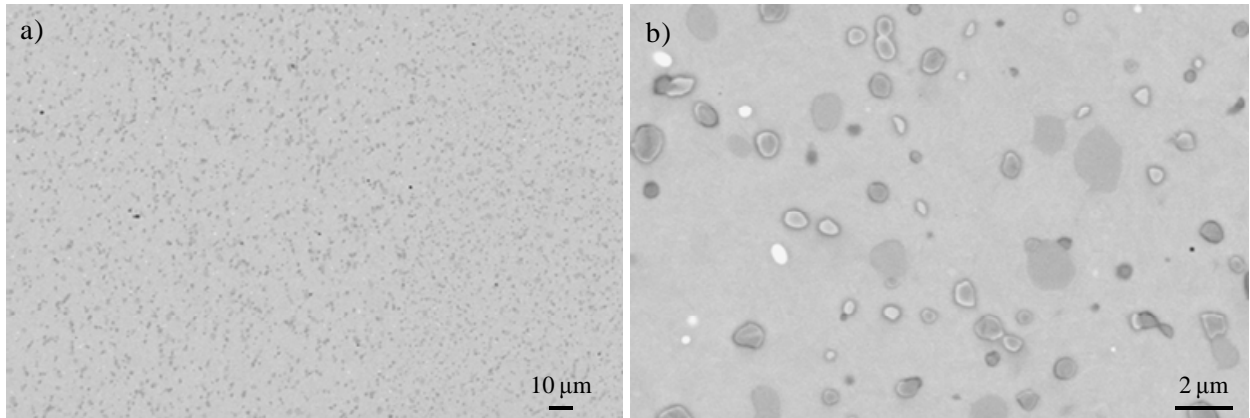


**Figure 1.1.2 a) Primary carbides in PM steels are dispersed in a uniform distribution even after hot working;
b) carbides show spheroidized shapes and small dimensions**

1.1.2 Hardening heat treatment

Besides the primary processing associated with the melting, solidification and breakdown stages of hot work, tool steels must also be hardened by heat treatment to produce the desired microstructures. Machining operations are performed before hardening heat treatment, since very high hardness of tool steels makes them essentially unworkable. Hardening is mainly accomplished by three heat treating steps: austenitizing, cooling or quenching and tempering (Figure 1.1.3).

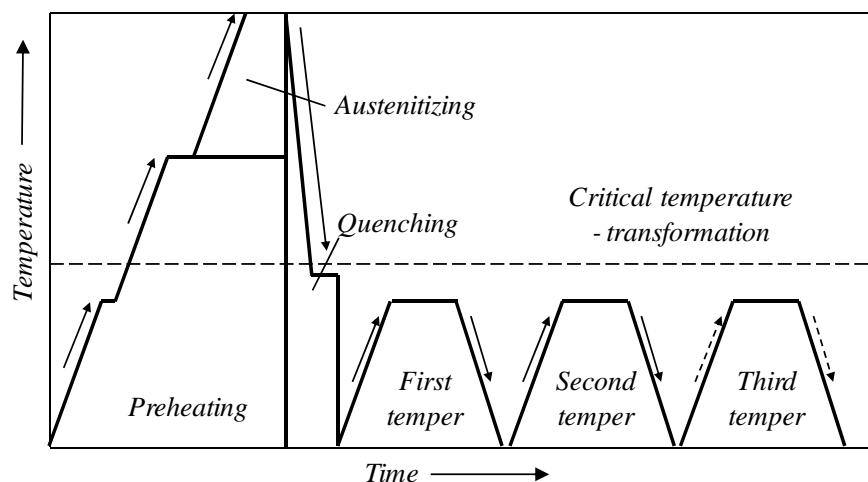


Figure 1.1.3 Schematic diagram of tool steel hardening heat treatment steps

1.1.2.1 Austenitizing and quenching

Austenitizing must accomplish several critical functions for the subsequent quenching and tempering stages: control the austenitic grain size to prevent coarsening and control the extent of alloy carbide dissolution as the tool steel composition approaches equilibrium at high temperatures. As alloy carbides dissolve, the austenite composition is enriched with the alloying elements and carbon, which once made up the carbides. Thus, not only the volume fraction of the carbides is controlled, but also the chemistry of the austenite, which controls hardenability, Ms temperatures, retained austenite content and secondary hardening potential (by supersaturation of the alloying elements in the martensite and thus, available to diffuse and precipitate as fine alloy carbides during tempering).

In addition to carbon content, the higher the alloying element content of austenite, the lower the Ms temperatures and the greater amount of retained austenite at room temperature. Thus, austenitizing temperatures must be well established and relatively low, in order to guarantee that at such temperatures, significant amounts of carbon and chromium are still combined in the form of carbides, and almost complete transformation to martensite occurs on cooling to room temperature.

As austenitizing temperatures increase, austenite grain sizes increase. Although the austenite transforms to martensite on quenching, features of the austenite grain structure are carried over into tempered martensite. In particular, the segregation of impurity elements and carbide formation at coarse austenite grain boundaries may cause intergranular fracture and lower toughness of hardened steels. However, in microstructures that contain second phase particle distributions, such as that of tool steels, grain growth is retarded by the particles.

Hardness is related to chemical composition, crystal structure and perfection, and the size and distribution of the various phases that make up the microstructure. High hardness correlates with high resistance to slip and dislocation motion, high work-hardening rates and high strengths. In martensite, the carbon-dependence of the high hardness martensite is attributed to carbon atoms trapped in the octahedral interstitial sites of the martensitic crystal structure. Other contributing factors to the strength of martensite are the dislocation substructure of the martensite, dynamic interactions of carbon atoms with dislocations during strain hardening, and in martensite tempered at low temperatures, the effect of fine transition carbide particles that precipitate from martensite supersaturated with carbon. Carbon, therefore, by its interaction with other structural elements of a martensitic microstructure, is the dominant factor controlling the strength of martensite. Substitutional alloying elements have a relatively small effect on the martensite strength.

1.1.2.2 Tempering

As-quenched microstructures consist of martensite and retained austenite, produced by cooling through the M_s from the austenitizing temperature, and alloy carbides retained during austenitizing. The martensite is unstable, in view of high dislocation density or twin substructure formed as a result of the shear transformation from austenite, and is supersaturated with respect to both carbon and alloying elements at whatever levels were produced in the austenite after partitioning between the austenite and retained carbides during austenitizing. Tempering behavior of highly alloyed tool steels is such of Figure 1.1.4, in which secondary hardening, a precipitation hardening associated with the precipitation of alloy carbides in tempered martensite takes place.

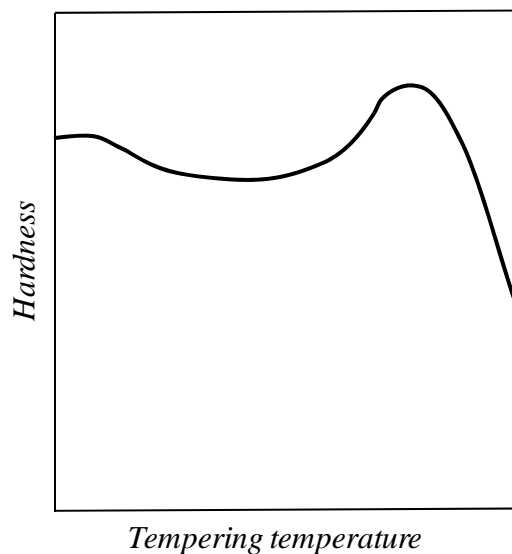


Figure 1.1.4 Schematic diagram of hardness versus tempering temperature (assuming constant time at each temperature) for high-speed or high-carbon, high-chromium tool steels

In order of increasing tempering temperature and assuming a constant time of tempering, the following microstructural changes evolve:

- Carbon atom rearrangements in martensite crystals (up to 100 °C).
- Transition iron carbide precipitation in martensite crystals (100 – 200 °C).
- Transformation of retained austenite (200 – 350 °C).
- Cementite precipitation and lowering of martensite tetragonality to produce a bcc ferritic matrix of tempered martensite.
- Precipitation of alloy carbides.

Carbon atom rearrangement may take the form of carbon atom segregation to dislocations and martensite crystal boundaries, clustering of small groups of carbon atoms, etc [ROB98]. The transition carbides precipitate within martensite crystals as rows of very fine particles, only 2 to 4 nm size. Not all the carbon supersaturation of the martensite is relieved by the transition carbide precipitation, and the martensitic matrix is estimated to retain 0,25 % wt C in solution. In this stage high hardness and strength are maintained because the low tempering temperatures limit the size of the transition carbide particles and cause little change to dislocation substructure of the as-quenched martensite. No substitutional alloying elements are found in the transition iron carbides, because of their very sluggish diffusion in the temperature range of this stage.

In highly alloyed steels, austenite transforms to martensite due to alloy carbide precipitation in the austenite during tempering. As a result for the reduced carbon and alloy content of the retained austenite, M_s temperatures increase and martensite forms on cooling to room temperature. Whether the austenite transforms to coarse carbides at the tempering temperature or to untempered martensite on cooling after tempering, either condition increases the sensitivity of the tool steel to brittle fracture. As a result, double and triple tempering treatments are applied to secondary hardening tool steels, either to spheroidize coarse carbides or to temper the untempered martensite formed after first or second tempering temperatures.

In the next stage of tempering, cementite precipitates. As more carbon combines with iron in the form of cementite, eventually complete relief of the carbon supersaturation of the martensitic matrix is achieved. The tetragonality of the martensite thus is eliminated, and the crystal structure of the martensite becomes cubic. Although the tempered martensitic matrix is now ferrite, it is still referred to as tempered martensite because of its martensitic origin and the fact that the martensitic crystals retain their lath or plate shape to very late stages of tempering. In high alloyed tool steels, precipitation of fine alloy carbides take place in the tempered martensitic matrix.

Prior to the tempering conditions that produce the secondary hardening peak, cementite has formed. At low and intermediate tempering temperatures, the substitutional alloying elements do not have sufficient mobility to form carbide particles. At tempering temperatures above 500 °C, alloying elements are able to diffuse, albeit only short diffusion distances because of the low alloy element diffusion coefficients even in this temperature range. The limited diffusivity of the substitutional alloying elements initially keeps the precipitated carbide particles fine, and thus the characteristic secondary hardness peaks develop. At higher tempering temperatures, however, diffusion accelerates, and the first precipitated alloy carbides are replaced by others. These rapidly coarsen and hardness rapidly falls. The secondary hardening alloy carbides form as very small disks or needles on specific crystallographic habit planes within the martensitic matrix.

From this standpoint, in this Thesis the microstructure of different tool steels will be examined in detail by providing chemic, geometric and crystallographic data of primary as well as secondary carbides embedded in the matrix. This will reveal indications for the microstructural design of tool steels to improve the performance of tools, satisfying the 1st objective of the Thesis.

1.2 Fracture resistance of tool steels

Fracture is characterized as the formation of new surfaces in a material. At the most basic level the essential feature of the process is breaking of interatomic bonds in the solid. From a macroscopic standpoint, fracture may be viewed as the rupture separation of the structural component into two or more pieces due to the propagation of cracks. In between the process involves the nucleation, growth, and coalescence of microvoids and cracks in the material. Thus, in studying the fracture in solids widely diverse factors should be considered, such as the microscopic phenomena taking place at various length scales and the macroscopic effects regarding the loading, environmental conditions, and the geometry of the medium. Due to the high complexity of the phenomenon there seems to be no single theory dealing satisfactorily with all its relevant aspects. Despite many theories developed to study the fracture of solids, they tend to treat the subject from one single point of view: microscopic or atomic, microstructural, and macroscopic or continuum mechanics [ERD00].

In the macroscopic approach to fracture, it is generally assumed that the material contains some flaws which may act as fracture nuclei and that the medium is a homogeneous continuum in the sense that the size of a dominant flaw is large in comparison with the characteristic microstructural dimension of the material. From this standpoint, fracture mechanics emerged to study the influence of the applied loads, the flaw geometry, environmental conditions and material behaviour on the fracture process in the solid.

The fact that theoretical shear stress necessary to deform a perfect crystal was many orders of magnitude greater than values commonly found in engineering materials made essential to explain not the great strength of solids, but their weakness [HER83]. Materials possess low fracture strengths relative to their theoretical capacity because most materials deform plastically at much lower stress levels and eventually fail by an accumulation of this irreversible damage. Tool steels contain material defects, such as pores, slag particles, inclusions and brittle particles (carbides), manufacturing flaws, and design defects which make reasonable to assume that they will fail as a consequence of such preexistent defects. The distribution of these defects and certainly, their size play such a rather important role in fracture.

1.2.1 The stress intensity factors and the notion of fracture toughness

1.2.1.1 Linear elastic fracture mechanics (LEFM)

In the 1920s, Griffith studies showed that various forms of imperfections, defects and scratches are primarily responsible for the difference between theoretical strength and bulk strength of solids. The basic concept underlying Griffith's theory was that solids possess surface energy and, in order to propagate a crack (or increase its surface area) the corresponding surface energy must be compensated through an externally added or internally released energy. For a linear elastic solid, this input energy which is needed to extend the crack may be calculated from the solution of the corresponding crack problem. This Griffith did by simulating the defects with an elliptical hole, the solution for which was previously given by Inglis in 1913.

By analyzing a plate containing an elliptical hole, Inglis showed that the applied stress, σ , was magnified at the ends of the major axis of the ellipse (Figure 1.2.1).

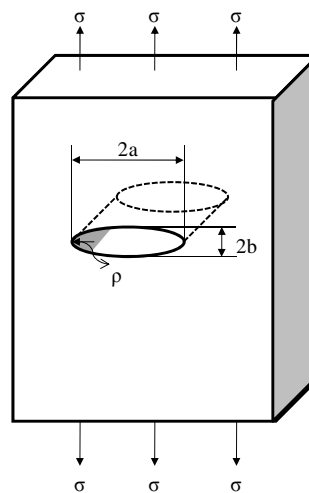


Figure 1.2.1 Elliptical hole in infinitely large panel

Assuming that in most cases $a \gg \rho$, Inglis was able to define the relationship shown in Equation 1.2.1:

$$\sigma_{max} \approx 2\sigma_a \sqrt{a/\rho} \quad (1.2.1)$$

where σ_a is the stress applied normal to the major axis, σ_{max} is the maximum stress at the end of the major axis, a is the half major axis and ρ is the radius of curvature at the end of the ellipse and is given by Equation 1.2.2:

$$\rho = \frac{b^2}{a} \quad (1.2.2)$$

where b is the half minor axis. Using this approach, Griffith calculated the increase in strain energy and, from the energy balance, obtained the stress corresponding to fracture as shown in:

$$\sigma = \sqrt{\frac{2E^*\gamma_S}{\pi a}} \quad (1.2.3)$$

where $E^* = E$ for plane stress and $E^* = E/(1-\nu^2)$ for plane strain conditions and γ_S is the specific surface energy. Thus, regarding the fracture of brittle solids, Griffith's was able to show that the fracture stress is dependent on the flaw size through the expression $\sigma = m/a^{1/2}$, where m is a material constant.

1.2.1.2 Elastic-plastic fracture mechanics

The term $2(a/\rho)^{1/2}$ shown in Equation 1.2.1 describes the effect of crack geometry on the local crack tip stress level and is known as the stress concentration factor, k . In structural materials there are always some inelastic deformations around the crack front that would make the assumption of linear elastic medium with infinite stresses at the crack tip highly unrealistic. According to this, Orowan observed in 1948 that even in materials fracturing in a "purely brittle" manner, there was evidence of extensive plastic deformation on the crack surfaces. This led Irwin and Orowan independently to conclude that the plastic work γ_p at the crack front must be considered as dissipative energy and the surface energy γ_S in Griffith's model must be replaced by $\gamma_S + \gamma_p$.

In the early 1950s, Irwin observed that in a fracturing elastic solid, if the characteristic size of the energy dissipation or plastic zone around the crack tip is very small compared to the crack size, then it is reasonable to assume that the energy flowing into the crack tip fracture zone will come from the elastic bulk of the solid and therefore, will not be critically dependent on the details of the stress state very near the crack tip. Consequently, the stress state in the elastic bulk of the medium will not differ from a purely elastic crack solution to any significant extent and thereby, using a purely elastic solution to calculate the rate of energy available for fracture may be justified.

From this standpoint, the fracture of flawed components may be analyzed by a stress analysis based on concepts of elastic theory. One of Irwin's major contributions was his recognition of the universal nature of asymptotic stress and displacement fields around the crack front in a linear elastic solid. He observed that for a small distance r from the crack tip, the stresses may be expressed as shown in Equation 1.2.4:

$$\sigma_{ij} \cong \left(\frac{K}{\sqrt{2\pi r}} \right) f_{ij}; \quad (1.2.4)$$

where f_{ij} are the functions for specific crack geometries and loading conditions. Irwin called the coefficient of the singular term, K , the *stress intensity factor*. To calculate the energy available for fracture, Irwin interpreted the energy release rate involving in the entire solid in terms of the crack closure energy. For the symmetric loading of a planar crack, he then evaluated the energy release rate as K^2/E^*

and designated it by G . Subsequently, Irwin published the solution for stress distributions associated with the three major modes of loading shown in Figure 1.2.2.

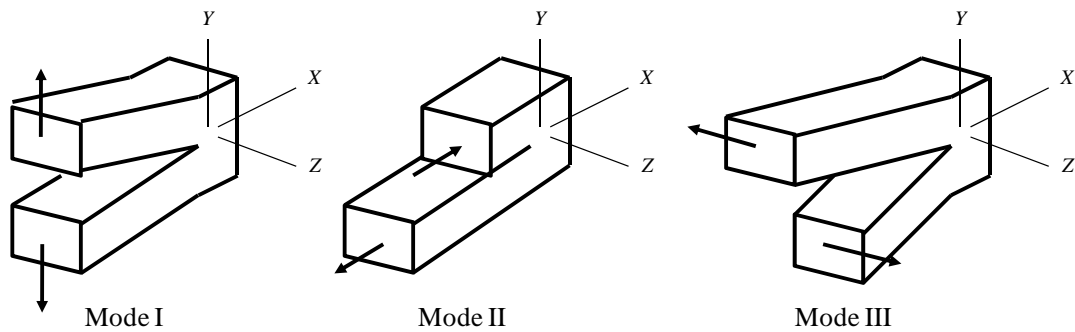


Figure 1.2.2 Basic modes of loading involving different crack surface displacements

Note that these modes involve different crack surface displacements: mode I, opening or tensile mode, where the crack surfaces move directly apart; mode II, sliding or in-plane shear mode, where the crack surfaces slide over one another in a direction perpendicular to the leading edge of the crack; mode III, tearing or anti-plane shear mode, where the crack surfaces move relative to one another and parallel to the leading edge of the crack.

Consistent with Equation 1.2.4, the stress intensity factor is most often found to be function of stress and crack length, as rewritten in Equation 1.2.5:

$$K = f(\sigma, a) \quad (1.2.5)$$

Opposite to the stress concentration factor, k , which only accounts for geometrical variables, crack length and crack tip radius, the stress intensity factor, K , incorporates both geometrical terms (the crack lengths appears explicitly while the crack tip radius is assumed to be very sharp) and the stress level. As such, the stress intensity factor provides more information than does the stress concentration factor.

To make the energy balance theory an effective design tool, the concept of a realistic single-parameter characterization of the materials resistance to fracture also needed to be developed. This required the additional assumption that, in solids fracturing in a brittle manner, the size and shape of the fracture process (or the energy dissipation) zone remain essentially constant as the crack propagates, leading to the hypothesis that in such solids the energy needed to create a unit fracture surface is a material constant. Irwin designated this fracture resistance energy as the fracture toughness, G_{IC} .

At this point, it is appropriate to say that the fracture toughness is often also expressed in terms of K_{IC} . The similarity between the two is demonstrated according to the relationship established by Irwin in which $G = K^2/E^*$.

In elastic-plastic materials, the size of the plastic zone itself is heavily dependent on the constraint conditions along the crack front. An estimate of the size of this zone may be obtained considering the stress existing directly ahead of the crack. As seen in Figure 1.2.3, the elastic stress $\sigma = K / (2\pi r)^{1/2}$ will exceed the yield strength at some distance r from the crack tip, thereby truncating the elastic stress at that value.

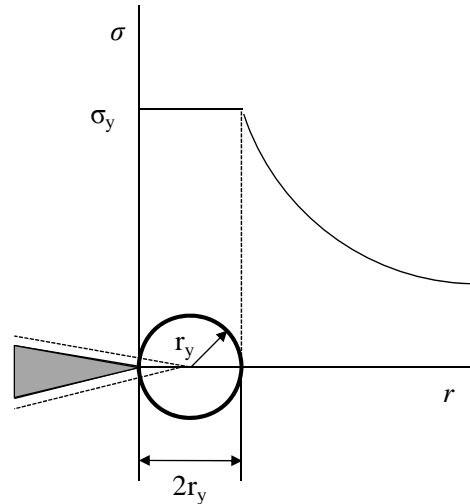


Figure 1.2.3 Onset of plastic deformation at the crack tip. “Effective” crack length taken to be initial crack length plus the plastic zone radius

By letting $\sigma = \sigma_y$ at the elastic plastic boundary, the plastic zone size, r_y , is computed to be $K^2/2\pi\sigma_y^2$. Since the presence of the plastic region makes the material behave as though the crack was slightly longer than actually measured, the “apparent” crack length is assumed to be the actual crack length plus some fraction of the plastic zone diameter. Irwin estimated this increment equal to the plastic zone radius, so that the apparent crack length is increased by that amount. In effect, the plastic zone diameter is a little higher larger than $K^2/2\pi\sigma_y^2$ as a result of load redistributions around the zone and is estimated to be different for plane stress and plane strain conditions, as shown in Equation 1.2.6 and 1.2.7 respectively:

$$r_y \approx \frac{1}{2\pi} \frac{K^2}{\sigma_y^2} \quad (1.2.6)$$

$$r_y \approx \frac{1}{6\pi} \frac{K^2}{\sigma_y^2} \quad (1.2.7)$$

For conditions of plane strain the triaxial stress field suppresses the plastic zone size. Thus, in relatively “thick” specimens the interior region would be under plane strain conditions, and near the surfaces, due to lack of constraints, there would be a transition to plane stress conditions, accompanied by greater plastic zone size and higher resistance to fracture (Figure 1.2.4). One would then observe a low energy flat fracture in the interior and shear lip formation and high energy ductile fracture near the surfaces.

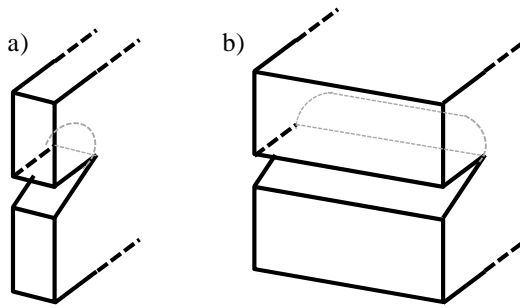


Figure 1.2.4 Fracture in a) thin sheets under plane stress state and b) thick plates under plane strain conditions

Since the fracture toughness of a material will depend on the volume of material capable of plastically deforming prior to fracture, and since this volume depends on specimen thickness, as shown in Figure 1.2.5, it follows that the fracture toughness K_C will vary with thickness. In “thin” specimens plane stress conditions prevail and the material exhibits maximum toughness (although if the sample were made thinner the toughness would gradually decrease because less material would be available for plastic deformation energy absorption). Alternatively, when the thickness is increased to bring about plastic constraint and plane strain conditions at the crack tip, the toughness drops to a lower level than that of the plane stress value. However, the plane strain fracture toughness, K_{IC} , does not decrease further with increasing thickness, thereby making this value a conservative lower limit of material toughness in any given engineering application.

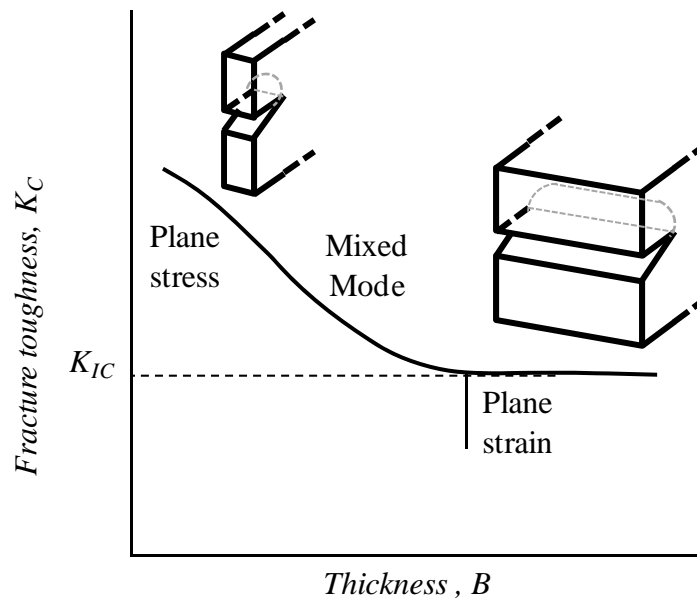


Figure 1.2.5 Fracture toughness in function of the material thickness under plane stress and plane strain conditions

To summarize, the fracture toughness under plane stress or mixed mode, K_C , is related to both metallurgical and specimen geometry, while plane strain fracture toughness, K_{IC} , depends only on metallurgical factors. Consequently the best way to compare materials on the basis of their respective intrinsic fracture toughness levels should involve a comparison of K_{IC} values. Plane strain fracture toughness is such an important property in fracture prevention that accepted test methods have been set forth by the American Society for Testing Materials (ASTM) under Standard E399-90 for its measurement in the laboratory.

1.2.2 The role of the tool steel microstructure in the fracture process

The carbon content in tool steels is high so that both in solid solution and in carbides, it serves as potent hardening agent. These hard particles may assume a variety of configurational forms, characterized by geometry, relative elastic stiffness, thermal expansion, anisotropy, mismatch and so on. The different arrangement, size and shape of particles are obtained depending on the degree of hot reduction forming, and the austenitizing temperature as well as other heat treatment parameters. Dislocations and cracks may be forced to move or propagate either around or through any hard phase obstacle, with consequent effect on ductility and toughness.

Dislocations control most aspects of strength and ductility in structural materials. The essential feature of yield strength is the density of obstacles that dislocations encounter as they move across the slip plane: higher obstacle density implies higher strength. However, the presence of these obstacles has also a strong impact on fracture, since they provide the nucleation sites for many cracks. Therefore, whether or not a material fractures depends on the competition between flow and fracture, and the latter depends, in turn, on the microstructure.

1.2.2.1 The fracture process in tool steels

The relationship between microstructure and fracture behaviour in tool steels has been a matter of concern for the scientific community since the late 1990s. Numerous efforts have been made to determine the stress field in the matrix at the neighbouring of the hard particles and to determine the causes for crack nucleation. Berns et al. [BER98] developed a Finite Element model to simulate material damage evolution and microcracking for a conventional high-speed tool steel ASP30. These authors studied the mechanical behaviour of individual constituents to describe the microcrack initiation and propagation as follows:

- The hard particles: they were assumed to fail by cleavage prior to deform plastically and cleavage was suggested, if the normal stress within the particle reached a critical value (the fracture strength of the carbide).

- The metallic matrix: void growth was used as damage indicator of the matrix, modelled as isotropic, elastic-plastic using Mises plasticity and isotropic hardening.
- The interface: interfacial failure was assumed to occur under pure mode I (tensile failure) and mode II (shear failure) when the radial and shear interfacial stresses reached a critical value.

The evolution of failure was found by Berns et al. as a first, single hard particle breakage due to cleavage, leading to a redistribution of stresses, which in turn caused neighbouring hard phases to fracture. Afterwards, plastic bands developed, connecting the individual microcracks. Along these bands, damage of the matrix took place. The matrix network was found to act as an effective obstacle for microcrack linkage.

Given the above observations in which material failure is initiated by cleavage fracture of carbides rather than matrix rupture, Antretter et al. [ANT97] used a Weibull approach to estimate the fracture probability of carbides in high speed tool steels. Larger particles were assumed to be more susceptible to cracking than smaller ones since the probability of the existence of a critical flaw is higher. The shape of the carbides, which depends largely on the degree of deformation the material has been exposed to in the production process, was also taken into consideration in the model as well as the carbides arrangement and the interaction of one hard particle with the stress field induced by its neighborhood. The study concluded that particles which induce high stress gradients (the most rectangularly shaped) are more likely to break than those which exhibit fairly smooth and uniform stress distributions (the most spherical ones).

Following this work, Rammerstorfer et al. [RAM99] developed a hierarchical modeling strategy describing the different mesostructures of high speed tool steels with microstructures consisting of brittle elastic particles in an elastic-plastic steel matrix. These authors used a mesostructurally layered approach which simulated the typical structures of high speed tool steels, from layered to clustered networks of carbides, to show that the matrix in the particle rich layers started to yield at much smaller macroscopic stress levels than the particle-poor layers, as shown in Figure 1.2.6

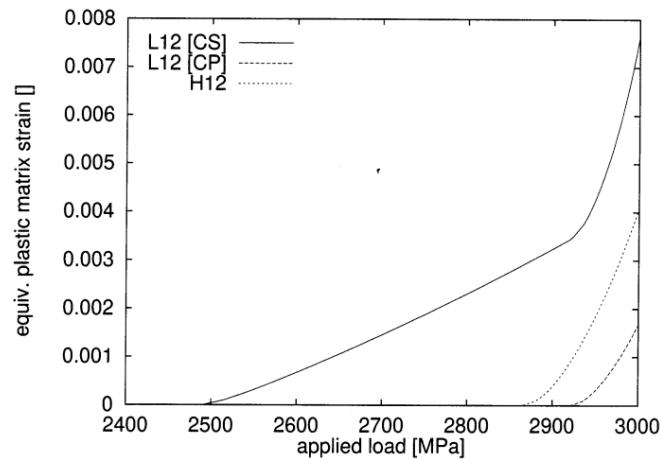


Figure 1.2.6 Accumulated effective plastic strain in the matrix of the individual layers as a function of the uniaxial tensile macro stress predicted via the micro-meso-macro layer model incorporating the MEFM (multiparticle effective field method); carbidic stringers and carbidic poor zones are denoted by CS and CP respectively; H denotes high-speed steel with a statistically homogeneous carbide distribution [RAM99]

Then, it becomes obvious that tool steels with a statistically homogeneous particle distribution (for example produced by powder metallurgy) show a considerably higher macro stress for onset of matrix yielding than the layered structured ones. The maximum principal stress in the particles was considered to assess the cleavage of carbides (Figure 1.2.7 a)). Again, the more pronounced the layer structure the lower is the macro stress leading to cleavage of carbides (in the particle rich layers). Also with this respect a statistically homogeneous carbide distribution would be beneficial. Analogous qualitative statements as for cleavage of carbides apply also for the martensitic-austenitic steel matrix, since it tends to fail in a brittle mode. The maximum principal stress in the matrix of the individual layers is shown in Figure 1.2.7 b).

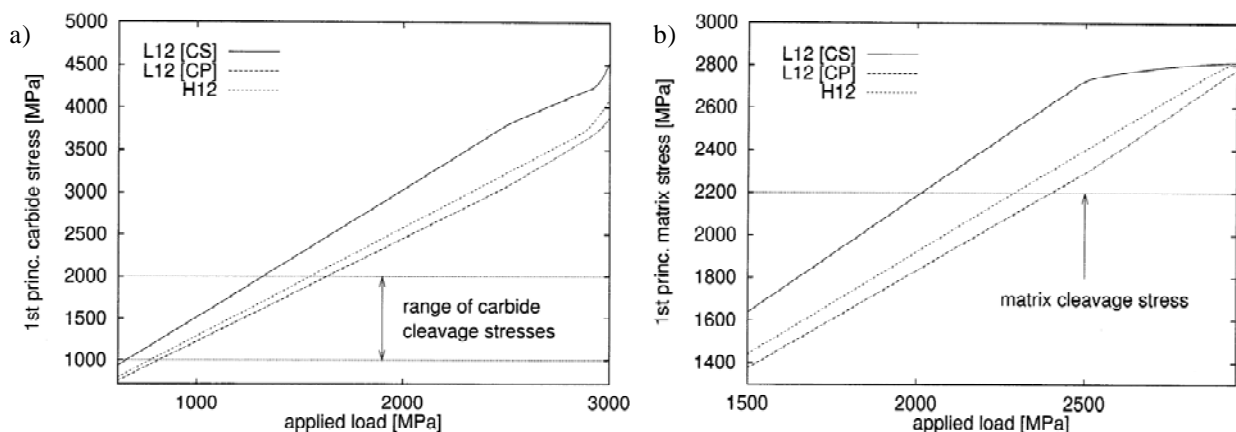


Figure 1.2.7 Maximum principal stress: a) in the carbides and b) in the matrix, in the individual layers predicted via the micro-meso-macro layer model incorporating the MEFM (multiparticle effective field method). The intersection between the horizontal line and the curve indicates initiation of a) carbide and b) matrix cracking at the corresponding macro stress; carbidic stringers and carbidic poor zones are denoted by CS and CP respectively; H denotes high-speed steel with statistically homogeneous inclusion distribution [RAM99]

From Figure 1.2.8 it can be seen that apart from the influence of the particle fraction, the highest principal tensile stress and hence the highest risk of particle cleavage appear in those carbides which have higher aspect ratios with the longer axis oriented in the direction of the applied maximum macro stress component.

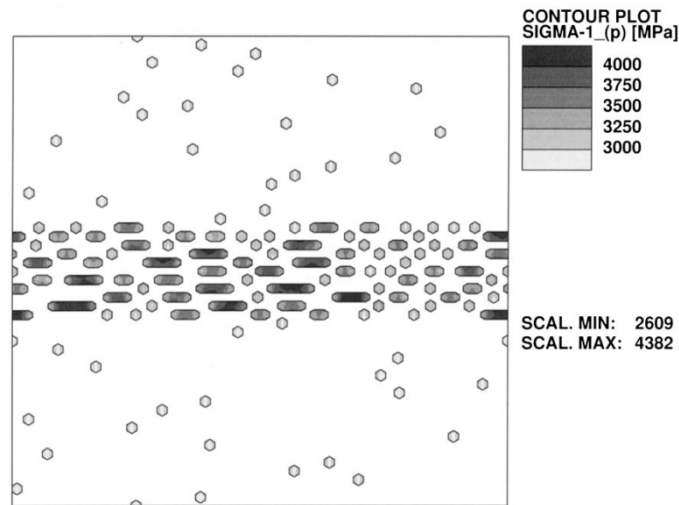


Figure 1.2.8 Fringes of the maximum principal stress in the carbides predicted via the Hexagonal Tiling concept at an applied overall load of $\sigma_{11} = 2900$ MPa [RAM99]

Cracking of carbide clusters was attributed by Bolton and Gant to the stresses generated at these carbides by differences between the Young's modulus of the carbide and the steel [BOL98]. Load transfer between the matrix and the carbide was thought to occur easily, because the carbides are well bonded into the steel matrix. As carbides are subjected to iso-strain conditions, they were assumed to experience higher localized stresses because of the fact that they have a higher Young's modulus than the surrounding matrix. The formation of larger macroscopic cracks by the coalescence of cracks formed in carbide clusters was eventually responsible for creating a critical-sized crack that generated catastrophic failure.

1.2.2.2 Influence of the intrinsic plasticity of the metallic matrix in the fracture toughness of tool steels

As seen previously, the fracture process consists in the formation of voids by carbide cracking, or decohesion with the matrix in the plastic zone at the crack tip, followed by the linking of these voids through deformation of the matrix. In this sense, Horton and Child showed that the most important factor affecting the fracture toughness of high speed tool steels is the intrinsic plasticity of the matrix [HOR83]. Increasing the plasticity of the matrix, by means of controlling the quantity of alloying elements dissolved in the martensite and which, in turn, is determined by the precise chemical composition, austenitizing conditions, carbide distribution and volume fraction, results in higher fracture toughness.

Carbide size and volume fraction also affect the carbide spacing and the size of matrix ligaments involved in the fracture process, thus the distribution of carbide segregates also affect the crack path through matrix areas; i.e. with carbides bands oriented perpendicular to the propagating crack the quantity of plastic work expended in fracturing the matrix is the greatest.

These authors reported the fracture toughness of several tool steels in the hardened condition and showed that hardness alone affects fracture toughness in such a way that lower hardness levels produce higher fracture toughness of the steels. The size of the plastic zone at different hardness levels was also estimated for the cast and hot worked M2 steel at different carbide orientations and the powder metallurgy steel ASP23 (in practice it is not possible to obtain M2 as powder metallurgy product, so ASP23 is the nearest equivalent, and corresponding to AISI M3-2). The mean carbide interparticle spacing of these two steels was also calculated and the values were compared to those obtained for the plastic zone size. The carbide spacing was found to be smaller than the plastic zone size up to 780 – 800 HV (63 – 64 HRC) for both M2 and ASP23 steels. Therefore, if the tool steel is softer than this, the plastic zone will always contain carbides and their distribution and volume fraction may be expected to affect the fracture toughness. In contrast, at greater hardness levels the fracture toughness will be expected to be influenced solely by the matrix properties.

According to this, the fairly superior fracture toughness reported in cast and hot worked tool steels compared to powder metallurgy steels was explained by the different microstructures of the two types of steels. Powder metallurgical steels use to have higher volume fraction of carbides but smaller mean carbide size. Thus the mean free path between the carbides is less than that of cast and wrought steels. Assuming that the plasticity of the ligaments between the carbides is essentially the same for the two types of tool steel of equal hardness, then the quantity of energy dissipated in producing a fast fracture for powder metallurgy steels will be less than that for cast and hot worked. That is, the microcracks formed at or in carbides can link up, with a minimum of plastic deformation of the matrix, owing to the smaller ligament sizes in the powder metallurgy steel [HOR83].

It is noteworthy that Horton and Child designed a semi-matrix steel (with lower volume fraction of carbides and greater carbide spacing) with similar composition than the two other studied tool steels and determined that the fracture toughness values in the semi-matrix steel were higher than those of cast and hot worked and powder metallurgy steels. The higher levels of fracture toughness were attributed to the increased lengths of the matrix ligaments. However, in a region of 800 HV (64 HRC), the fracture toughness values of the semi-matrix converged with, and were similar to, those of the cast and hot worked and powder metallurgy steels respectively (Figure 1.2.9). This observation was consistent with the above statement in which at greater hardness levels the fracture toughness will be expected to be influenced solely by the matrix properties, independently of the presence of primary carbides.

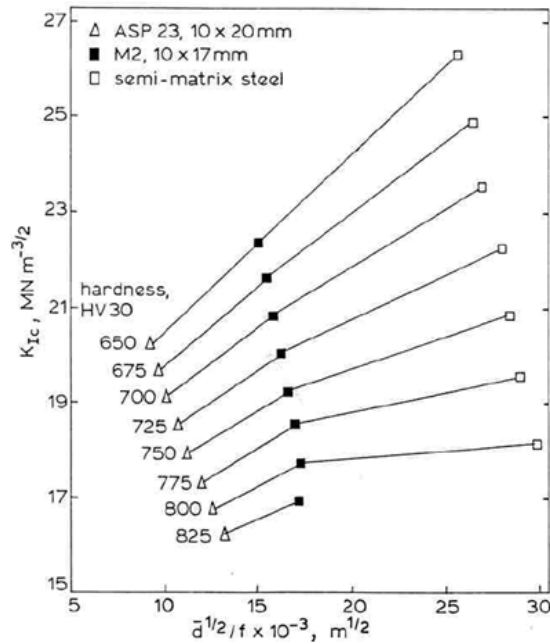


Figure 1.2.9 Fracture toughness, K_{IC} , at constant hardness, $HV30$, versus mean carbide diameter, d , and volume fraction of carbides, f [HOR83]

Muro et al. performed similar tests to Horton and Child analysing whether there is any difference between the fracture toughness of wrought D2 and powder metallurgy D2 matrix steel and how different carbide distributions affect toughness [MUR02]. From the experimental results, Muro et al. appreciated that the presence of primary carbides produced a clear decrease in the fracture toughness of D2 steels as compared to that of D2 matrix steel with the same hardness. Primary carbides are brittle and they are easily broken in the steel before the crack reaches them, especially when the plastic region ahead the crack tip is similar to the distance between primary carbides, as is the case when carbides are oriented parallel to the crack growing direction and in the PM steel.

However, independently of the relation between the mean free path between carbides and the radius of the plastic zone ahead the crack their distribution or orientation was found by Muro et al. to not affect toughness because the calculated critical defect size was much higher than the carbide size or the mean distance between carbides. If so, the carbides would not be big enough to control crack propagation and could only act as nucleation sites. Therefore, it was emphasised that crack propagation is controlled by the ductility of the matrix, which is in turn, a result of the heat treatment conditions like austenitizing and tempering times and temperatures.

This statement was already corroborated in the work by Bolton and Gant [BOL98]. These authors found that fracture toughness values in a M3/2 + TiC composite were almost identical to those found in the baseline M3/2 high speed tool steel of equivalent matrix hardness, and were largely unaffected by the particulate addition. Crack propagation was therefore unaffected by the presence of any small pre-existing cracks that were formed within TiC/MC clusters at stresses below the final fracture stress. Such behaviour

agrees with the suggestion above that individual cracked carbide clusters of such sizes are too small, too isolated and too dispersed to influence crack propagation.

Therefore these findings support the suggestion that fracture toughness of metal matrix composites become dependent on the volume fraction, size, and distribution of added particles only at some critical level. Below this critical level, fracture toughness is governed by the microstructure and mechanical properties of the matrix, which are particular to the heat treatment state of the steel. Tempering improves the fracture toughness of as-quenched tool steels due to stress relief, until secondary hardening exercises a dominant effect above 500 °C. Tempering below 500 °C leaves residual austenite in the structure and from Figure 1.2.10 it is clear that retained austenite improves the fracture toughness.

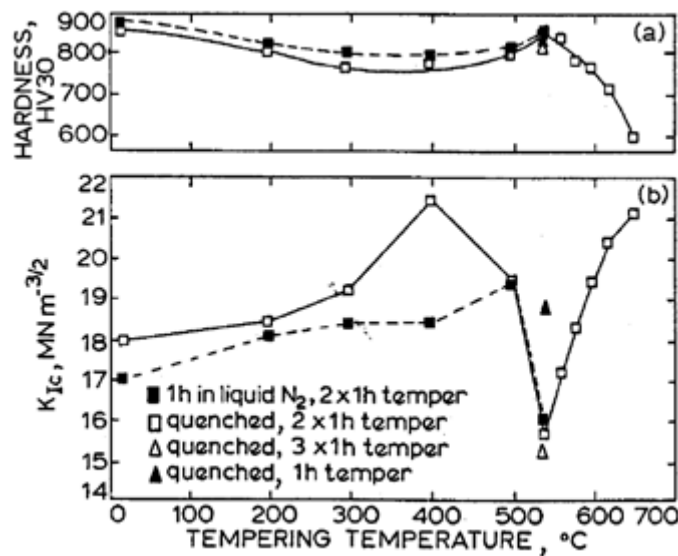


Figure 1.2.10 Fracture toughness and hardness versus tempering temperature for 10x17 mm M2 bar, after quenching to room temperature and after immersion in liquid N₂ before tempering; all samples austenitized at 1220 °C for 4 min [HOR83]

1.2.2.3 Dislocation movement and crack propagation in tool steels

Carbide cracking or decohesion, as discussed above, are believed to occur before the failure of the matrix. It is thought that these cracks link up through the fracture of the matrix, and, as the carbide segregates are not all in the same plane, changes in the local crack growth direction occur. There is an increase of the fracture surface area due to the linking of the crack nuclei at the carbide bands, which do not all lie in the same plane. Not only this will result in an increase of the surface energy but, more importantly, it will also be associated with local plastic deformation of the matrix during the process of fast fracture. That is why first, plastic deformation of the metallic matrix controlled by the movement of dislocations through the metallic matrix and then, propagation of the existing cracks from carbides through the microstructure are two governing mechanisms in the fracture process of tool steels.

-Principles of dislocation movement

The Orowan mechanism considers the interaction between a dislocation and an array of hard obstacles which are impenetrable for the dislocation, Figure 1.2.11. The dislocation is forced to bow out between the obstacles (this is the primary effect responsible for all particle strengthening mechanisms). Plastic deformation due to long-range dislocation motion requires dislocations to fully bypass the obstacles (the “Orowan mechanism”). The bypass condition is reached when the characteristic length, d , approaches (or comes to lie below) the obstacle spacing, L . In other words, plastic deformation requires the dislocation loops (or half loops) to fit between two neighboring obstacles. This requirement reflects the classical size effect: a finer dispersion (smaller L value) results in more efficient hardening.

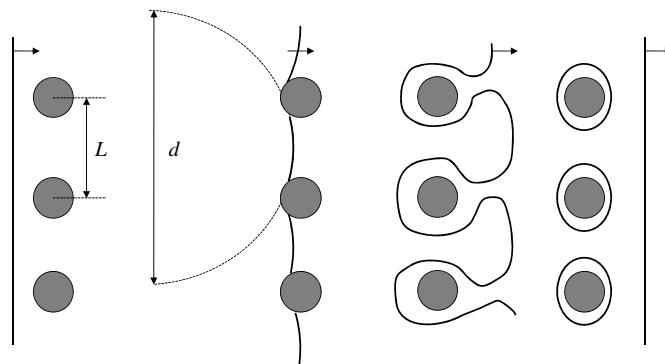


Figure 1.2.11 The onset of plastic flow controlled by obstacles: plasticity requires bypassing of strong obstacles by dislocations, equivalent to the condition that dislocation loop fit between neighbouring obstacles

As follows from the explanation above, Orowan’s mechanism accounts the fact that obstacles are impenetrable to the dislocation. However, many obstacles such as solute atoms or coherent precipitates are not impenetrable and the dislocation can be released from the obstacles before the limiting condition $d \leq L$. In this case, the obstacle spacing is no longer a constant given by the microstructure, but depends also on the strength of the obstacle. At small particle sizes, the dislocation cuts through the particle. Strengthening imparted by such shearable particles is scaled with their radius, r_p , of the following form [ARZ98]:

$$\tau \propto \sqrt{r_p} \quad (1.2.8)$$

where τ is the “cutting stress”. At large particle sizes, the dislocation bows around the particle more easily than it cuts through it. But larger particles mean fewer particles (via coarsening) hence, lower flow stress. In contrast to the cutting stress, the “bypassing stress” stands with a r_p dependence as follows [ARZ98]:

$$\tau \propto \frac{Gb}{r_p} \quad (1.2.9)$$

where G is the shear modulus of the matrix material and b the Burgers vector magnitude. These opposite size effects are the basis for age-hardening behaviour of precipitation-strengthened systems. Figure 1.2.12 illustrates schematically a simple ageing curve constructed using Equations 1.2.8 and 1.2.9. The maximum yield stress, corresponding to the “peak-aged” conditions, occurs at the transition from cutting to bowing, i.e. at the critical radius, r_{pc} , which reflects the particle properties.

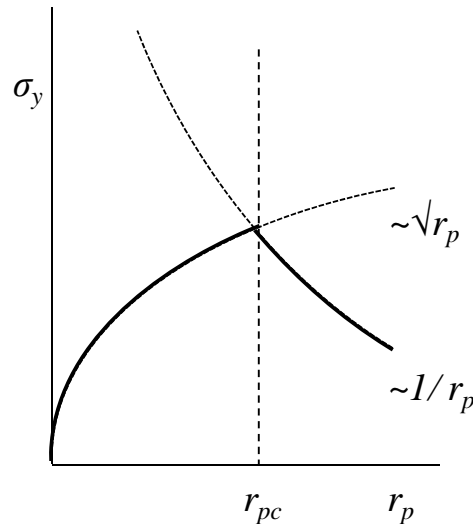


Figure 1.2.12 Size effect resulting from a $\sqrt{r_p}$ -dependence of the cutting stress (Equation 1.2.8) and a $1/r_p$ -dependence of the bypassing stress (Equation 1.2.9). This causes maximum in yield stress σ_y vs particle radius r_p at a characteristic value r_{pc}

-Principles of crack propagation

Analogous to dislocation movement, obstacle particles determine crack bowing and crack deflection phenomena in structural materials. If particles are present, large differences in elastic modulus can either attract or repel the crack in the same plane (tilt deflection) or out of it (twist deflection), Figure 1.2.13 [LAW93]. As a result, in either case the stresses at the crack tip are lower than it would be if the crack was straight and in the plane.

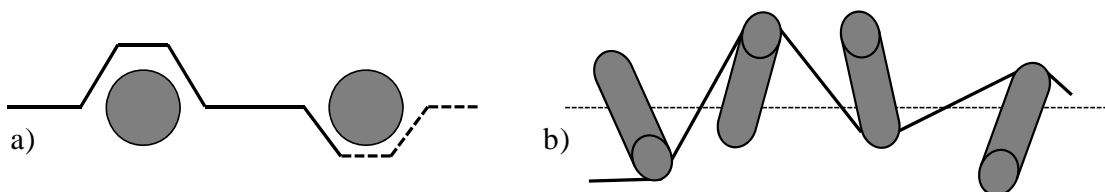


Figure 1.2.13 Crack deflection geometries in two-phase solids: a) tilt deflections around spheres, large mode II component (crack propagation left to right); b) twist deflections around rods, large mode III component (crack propagation into plane of diagram – dashed line undisturbed crack plane)

Toughening induced by crack deflection may be accomplished by providing moderately weak interfaces perpendicular to the anticipated direction of crack growth. Since there can be no stress normal to a free surface, the crack becomes blunted when reaches this interface, Figure 1.2.14. If the adhesion at the interface boundary is too strong, the crack may be forced to penetrate the second phase [LAW93]. An advancing front may then be pinned, causing local in-plane segments between dispersed particles to bow into loops, much like the pinning and breakaway concept in dislocation-hardening theories explained before.

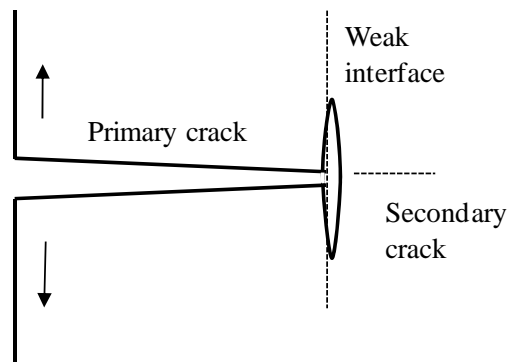


Figure 1.2.14 Division of crack along extended weak interface in tensile specimen. Driving force for extension diminishes as secondary fracture grows further from primary plane

Horton and Child postulated that in tool steels, if cohesive strength of planes of weakness (as would be generated by carbides oriented perpendicular to the propagating crack) is of the order of one-third of the general cohesive strength of the solid, then separation along the planes of weakness is prone to take place [HOR83]. Thus, if the planes of weakness are oriented at right angles to the macroscopic crack propagation direction, then crack deflection and crack tip blunting can occur if the above conditions are satisfied, see Figure 1.2.14. Not only this will result in an increase in the fracture surface area, but it will also lead to the elimination of the triaxial state of stress at the local crack tip, which will be replaced by a state of uniaxial tension below the deflected crack tip. Therefore, if the crack front is to propagate any further an increase of the load will be required, which in turn will result in increased toughness. Therefore, Horton and Child's argument may explain the marked superiority, in terms of fracture toughness, of single notched bend specimens, with their carbides segregates oriented perpendicular to the crack front.

1.2.3 Crack nucleation and growth in tool steels

1.2.3.1 Principles of R-curve in tool steels

Gomes et al. [GOM97] reported on static subcritical crack growth in metallic materials namely high speed steels, that under increasing monotonic stresses, crack nucleation and growth of natural cracks in these materials takes place at stresses below those for yielding or fracture. This argument found by Gomes et al. questioned the meaning of fracture mechanics and the employ of stress intensity factors for

microstructurally short cracks, and led these authors to introduce the notion of the R -curve in tool steels. Although the R -curve behaviour of ceramics and composites is commonly known, just the work of Gomes et al. dealt with it in case of tool steels (at least up to the knowledge of the present author).

Gomes et al. postulated that if stress intensity factors were to be estimated at the level of these short cracks, a critical value did not need to be reached since microstructural parameters, rather than macroscopic material properties (which hold for long cracks in the same materials) governed this type of microcrack growth. The size of the plastic region around the crack front varies with growing crack size, generally increasing with the increasing crack size. This implies that a material's resistance to fracture, R , would also increase with increasing crack size.

With rising load conditions, it is possible for the material to experience stable crack extension prior to failure, which makes it difficult to determine the maximum stress intensity level at failure because the crack length is uncertain. In addition to the uncertainties associated with the measurement of the stable crack growth increment, Δa , a plastic zone may develop in the metallic matrix of tools steels, which also must be accounted for the stress intensity factor computation.

First for crack propagation, a local condition for crack growth initiation needs to be satisfied, and then a global energy balance must be fulfilled for further crack growth or unstable fracture. The mechanism for crack initiation may be the nucleation, growth and coalescence of voids or microcracks, or simply decohesion at the crack tip. Failure should then occur when the rate of change in the elastic energy release, dG/da , equals the rate of change in material's resistance to such crack growth, dR/da (Figure 1.2.15). The material's resistance to fracture, R , is expected to increase with increasing plastic zone development and strain hardening. Consequently, both G and R increase with increasing stress level.

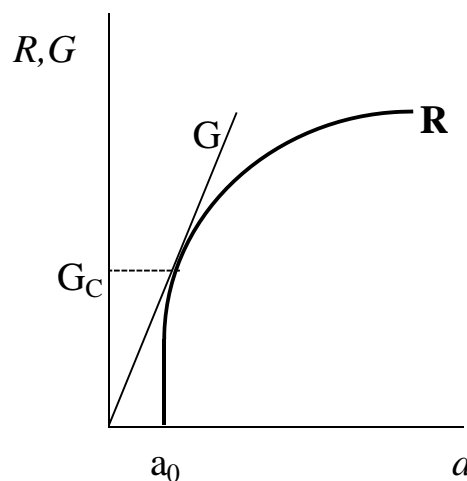


Figure 1.2.15 Instability condition occurs in cracked solid when $dG/da = dR/da$

The fracture resistance is sometimes represented by the equivalent stress intensity factor, K_R , since G and K can be related by the expression shown by Irwin $G = K^2/E$. The R -curve is thus a continuously distributed parameter characterization of fracture growth which provides an effective tool to examine the process of slow stable crack growth and fracture instability.

1.2.3.2 The R-curve behaviour of tool steels as described by Gomes et al.

The short R -curve behaviour proposed by Gomes et al. [GOM97] differed from specimen to specimen in high speed tool steels of nominally the same composition and microstructure; being recognised that there is no unique R -curve for a material. Cracking of MC carbides in a cast and wrought T42 high speed steel was observed on the tensile faces during bend testing at stress levels of 770 to 1080 MPa (46 – 64 % of the fracture strength), 450 to 570 (39 – 49 % of the fracture strength) and 450 to 550 MPa (40 – 49 % of the fracture strength) for 575, 525 and 450 °C tempers respectively.

In the series of metal matrix composites based upon M3/2 high speed steel produced by powder metallurgy studied by Bolton and Gant, microcracks were also observed on the polished tensile faces of heat treated three-point bend test specimens after testing, at some distance away, 100 μm , from the point where complete fracture occurred [BOL98]. This observation is in agreement with the work of Gomes et al. in the way that some form of sub-critical crack growth must have had occurred prior to final failure. This failure initiation in carbides was always associated by Gomes et al. with large, > 25 μm , irregularly shaped MC carbides in the T42 wrought steel. From several crack nuclei generally present, crack extension took place in one or more locations as the stress was increased. Microcracks initiated in a carbide grew easily within the stringer, but were arrested temporarily (till a higher stress was applied) on reaching the relatively carbide free region between the stringers [GOM97]. Cracks in M3/2 composites in turn, were found by Bolton and Gant to occur in both the high speed steel matrix and inside the ceramic carbides, or within MnS inclusion/carbide clusters seen in the composite materials through debonding at the MnS/matrix interface [BOL98]. The more usual for high speed steels stepwise R -curve behaviour (b) is to be contrasted with (a) in Figure 1.2.16, where growth took place from two crack nuclei (cracked carbides) along prior austenite grain boundaries oriented nearly transversely to the tensile axis.

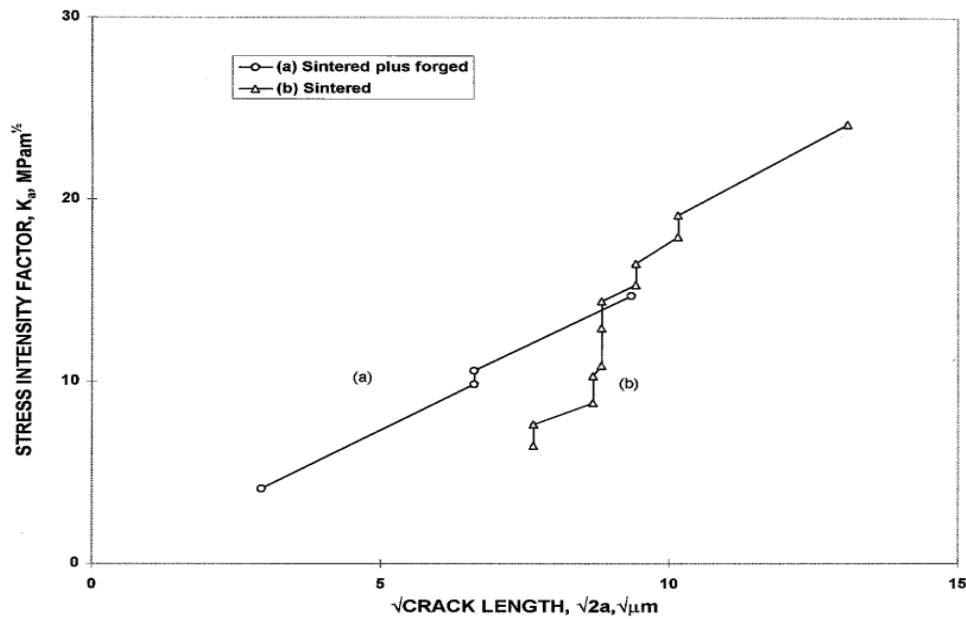


Figure 1.2.16 Experimental *R*-curves from stress generated crack nuclei for two T1 high-speed steel bend specimens which failed at $K < K_{IC}$. Contrast the markedly stepwise behaviour of the (b) specimen with that of (a), which involved linking up two crack nuclei along prior austenite grain boundaries, oriented nearly perpendicularly to the tensile axis [GOM97]

Although these nucleated cracks might potentially be sufficiently large to promote instantaneous/catastrophic crack propagation, it appeared more likely that they were initially sub-critical-sized cracks which progressively grew into larger cracks that eventually satisfied the critical size and critical stress intensity conditions needed for their propagation. Ahead of some arrested cracks, especially if there was an easy prospective path for crack growth transverse to the tensile axis, characteristic regions (tentatively identified as domains of localised plastic flow) were observed by Gomes et al., extending of some 2 -15 μm . The regions sometimes were of V-shape and in some specimens nucleation of fresh microcracks appeared to take place in these regions [GOM97].

Several subcritical crack systems were identified in a bend specimen both by Gomes et al. and Bolton and Gant. However, the non-propagating microcracks were found by Gomes et al. to be extremely shallow, their depth not exceeding 5 - 6 μm , contrasting with the approximately semicircular geometry of the observed failure initiating sites. Development into a critical-sized defect required growth of any microcracks into a semi-circular flaw and that was dependent on the local microstructure being conducive to the formation of semi-circular microcracks. Effects as any lack of inherent ductility within the surrounding matrix, or a small separation between isolated cracks in brittle particles, would assist the linking together of small cracks to form a larger critical-sized crack.

Critical stress intensity levels required for crack propagation with short cracks at the micro level were found by Bolton and Gant to be less than K_{IC} , which refers to the propagation of large macroscopic cracks [BOL98]. Additional problems in estimating K_{IC} also arise from possible variations in flaw shape parameter that could occur with different types of crack initiating sites, changes in local crack opening mode, and the possible absence of plane strain conditions at the defect responsible for initiating bend stress failure. Considering that the estimated stress intensity factor decreases with c/a ratio (where c and a are the surface length and in-depth dimensions of the propagating crack, as schematized in Figure 1.2.17) and since the geometry of the nuclei of these critical cracks is unknown, Gomes et al postulated that if a semi-circular ($a = c$) crack, which simply grows in size, is assumed to be formed instead of an initially shallow ($a < c$) crack, which would eventually cause failure when attaining the semi-circular geometry, the R -curve plot behaviour would be overestimated.

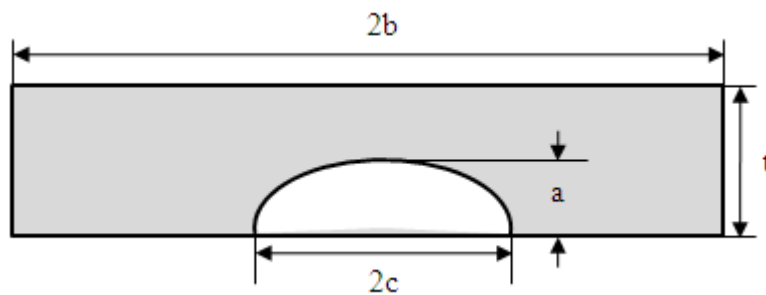


Figure 1.2.17 Geometry of a surface crack; $2c$ is the surface major axis and a the interior semi-minor axis, the crack depth. The thickness, t , and width, $2b$, of the specimen are also shown

What was clearly established by these authors was however, that microstructurally short cracks naturally nucleated and then arrested, followed by subsequent fracture under monotonic loading, cannot be satisfactorily interpreted by conventional go / no go linear elastic fracture mechanics. Subcritical growth can take place, in several discrete steps of crack extension, and the condition for eventual crack propagation cannot be satisfactorily described in terms of a critical value of stress intensity factor.

Crack tip plasticity, crack tip shielding and crack closure have been considered in an attempt to interpret this phenomenon. A distinction should be drawn between growth of a microcrack and formation of microcracks ahead of a macrocrack which link up the main crack. The microcrack will stop or deflect if the easiest path for cracking is sufficiently tortuous and a higher stress will be required for its continued growth or propagation.

It is interesting to note after the work of Gomes et al. that the secondary hardening treatment at $575\text{ }^{\circ}\text{C}$, overtempering, resulted in the greatest difficulty for crack growth and the smallest critical defect size, as the fracture strength was higher than for material with the other two heat treatments. Interestingly, crack nucleation was also the most difficult in this microstructure. This was related to matrix microplasticity. Thus, the subcritical crack growth would not be only influenced by the established microstructural

features such as grain misorientations, shape of grain boundaries, surface energies of interfaces (grain/grain, grain boundary/carbide, matrix /carbide), but also by minor changes in the microstructure of the matrix, possibly change in size and distribution of secondary carbides in the case of high speed steels. That meant that bend strengths were most likely controlled by subcritical crack growth to a critical crack size, and then by the fracture toughness of the matrix, which determined the point at which cracks became capable of causing catastrophic fracture.

The behaviour of short cracks in high speed steels under fretting, monotonic and cyclic loading is postulated to be similar and thus, these observations are relevant to cutting tools and wear parts. Gomes et al. also evidenced carbide cracking in compression at comparable stresses, meaning that a critical shear stress criterion for this process could appear reasonable. This hypothesis was negated by the orientation of the cracks, transverse not only to the tensile, but also frequently the compressive axis. Crystallographic orientation of these carbides and their cleavage planes may be the important factors regarding the operating mechanism. The criterion may well be of a distortional strain energy (independent of sign of uniaxial stress). This has the added attraction that energy, unlike simple mismatch criteria, are inclusion (precipitate) size dependent. It is therefore suggested that the roles of carbide composition, size and shape in the context also of crack nucleation (cracking and decohesion) need to be examined, especially the relevant energies, and not only local stresses and mismatch strains.

Gomes et al. noted that *R*-curves were employed in their study as the least inappropriate representation of the phenomenon of this static subcritical crack growth, using the assumptions usually applied in ceramic materials and oversimplifications. This approach generally postulates that the crack grows in a continuum solid and assumes a continuous *R-a* function, what is unrealistic for real steels. In these materials there are microstructural discontinuities, as evidenced by the observed stepwise crack growth in high speed steel specimens.

From this standpoint, in this Thesis the results reported by Gomes et al. on subcritical crack growth will be contrasted with the outcomes of the present investigation, by means of the analysis of the initiation and growth of small cracks and *R*-curve behaviour of the tool steels considered. Additionally, the macro- as well as micro-mechanical properties of different tool steels will be determined in fracture tests, and results will be rationalised according to the microstructural features of samples, the principles of fracture mechanics and the most relevant findings in the literature exposed before. These findings will contribute to reach the 2nd, 3rd and 4th goals of this Thesis.

1.3 Fatigue resistance of tool steels

Fatigue is characterized as a three-stage process involving nucleation, propagation and final failure stages. The initiation life is considered as the number of loading cycles required to develop a crack of some specific size, and the propagation stage corresponds to that portion of the total cyclic life which involves growth of that crack to some critical dimension at fracture. So far, there is no precise definition for crack nucleation, i.e. for when a defect becomes a crack; and defining the transition point corresponding to a small and large crack length has typically been rather controversial [HER83].

When the crack length is small, fatigue behaviour is controlled by the microstructure ahead of the crack tip and the local stress field associated with it. In contrast, when the length is large fatigue behaviour is then controlled by the remote stress and concepts of linear elastic fracture mechanics (LEFM) can be applied. Thus, LEFM can only be used to calculate the propagation portion of the total life (when the length of a crack is sufficiently large) and the applicability of the stress intensity factor as the controlling parameter for short fatigue crack formation and early growth is doubtful.

1.3.1 Fatigue crack initiation mechanisms in tool steels

1.3.1.1 The different failure modes observed in fatigue of tool steels

As seen in earlier sections, tool steels contain defects, such as pores, slag particle, inclusions, manufacturing flaws or design defects, and they also contain brittle particles (carbides), which make relatively easy the nucleation of fatigue cracks. Despite the variety of existing publications regarding the fatigue behaviour of high-speed and cold work tool steels (Berns et al. [BER87], Meurling et al. [MEU01], Shiozawa et al. [SHI01, SHI06-1 and SHI06-2] Lu et al. [LU09], Fukaura et al. [FUK04] and Sohar et al. [SOH08-1, SOH08-2, SOH08-3], amongst many others) all the investigations convey that fractured carbides or inclusions (or debonding at the particle – matrix interface) can initiate fatigue cracks which propagate and cause fracture.

Berns et al. [BER87] compared the fatigue behaviour of sintered PM and conventionally manufactured ingot metallurgical high-speed steels up to the 10^6 loading cycles and found that in as-sintered PM variants, crack initiation occurred at pores but, after hot working, it occurred at nonmetallic inclusions (mostly in the subsurface region). However and besides the observation of some cracks in the surface of polished PM steel specimens at already early stages, no visible microstructural initiators could be found by these authors. Contrarily, in conventional cast and hot worked steel specimens, the primary alloy carbides (which represent the largest discontinuity group with a high frequency of occurrence) were found to be cracked in the surface during the first cycle. After the 20 – 30 % of the total fatigue life,

Berns et al. observed the matrix bridges between neighbouring carbides to have split up and the crack to have left the carbide band and penetrate the matrix, giving rise to cracks which caused the fracture.

The work of Meurling et al. [MEU01] also revealed that internal oxide inclusions and carbides at the surface of various types of cold work and high-speed tool steels acted as crack initiation sites during fatigue loading up to $2 \cdot 10^6$ cycles. However, due to the fact that some S-N data of PM steels showed material failure beyond 10^6 loading cycles, some authors realized the necessity of producing data at low stress amplitudes and up to the very high cycle fatigue (VHCF) regime to explain the fatigue initiation mechanisms of tool steels.

In this sense, Shiozawa et al. and Lu et al. [SHI01, SHI06-1, SHI06-2 and LU09] showed that in cantilever-type rotary bending fatigue tests at the regimes of the 10^7 - 10^9 cycles, the fatigue crack initiation sites in a high carbon-chromium bearing steel, JIS SUJ2 [SHI01 and SHI06-1], in a high-speed tool steel, JIS SKH51 [SHI-06-2] and in a high carbon-chromium bearing steel, GCr15 [LU09] were different depending on the stress amplitude and the number of cycles to failure, and that it could be classified into two typical modes:

- The first mode was observed at high stress amplitude and short life. The fatigue crack initiated on the specimen surface due to gradual growth of microcracks, which were initiated in slip bands due to stress concentrations at the surrounding of non-metallic inclusions (Figure 1.3.1 a)).
- The second mode occurred at low stress amplitude and long life, when the aforementioned microcracks initiated at the surface were arrested (i.e. below the fatigue limit for a surface fracture, which depended on the microstructure, hardness, residual stress distribution, etc.) and the fatigue crack initiated then from the interior of a specimen and formed a fish-eye pattern with a non-metallic inclusion at the centre (Figure 1.3.1 b)).

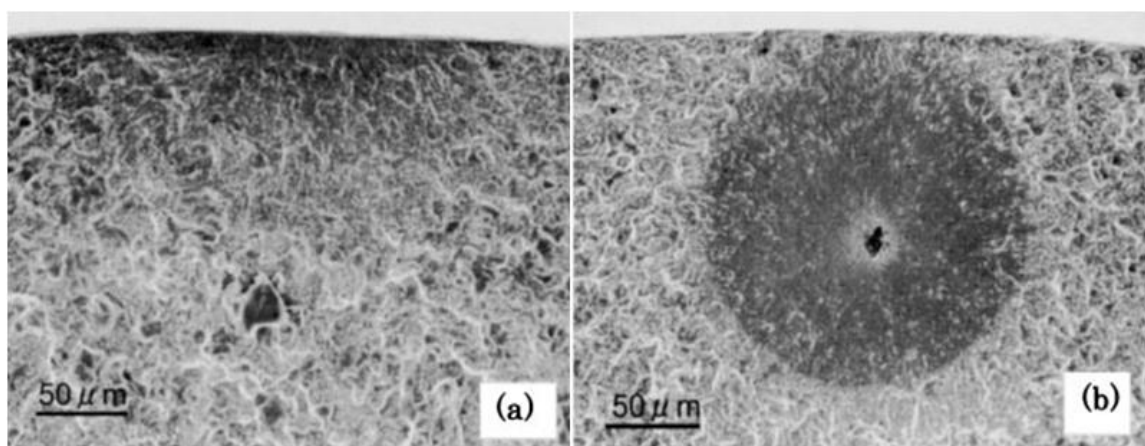


Figure 1.3.1 SEM observations of a) surface crack initiation sites and b) fish-eye type fracture surface [SHI01]

In the first case, the fatigue crack was initiated at inclusions and increased in size in a circular shape. But in the second, Shiozawa et al. observed a bright-facet area, the so-called “granular-bright-facet” (GBF) area, at the centre of the fish-eye and in the vicinity of the inclusion at the fracture origin. The GBF revealed a very rough and granular morphology in comparison with the area inside the fish-eye. These differences in roughness were attributed to different crack propagation mechanisms: the rough morphology in the GBF was attributed to multiple microcracks which increased in size and number during the fatigue life (the propagation of these microcracks was assumed to be very slow at this time); but after the formation of an appropriated size for the GBF area to enable the propagation as an ordinary crack, the smooth fish-eye surface was attributed to the stable propagation of this crack, which took place without dependence on the microstructure of the material.

Shiozawa et al. proposed a “dispersive decohesion of spherical carbide” model to explain the formation of the GBF area during the high-cycle fatigue process. As shown in Figure 1.3.2, initially multiple microcracks would be dispersed by decohesion of spherical carbides from the matrix near a non metallic inclusion (Figure 1.3.2 a). These microcracks would grow and coalesce with each other during fatigue cycles (Figure 1.3.2 b) and propagate along a boundary between the spherical carbide and the matrix (some carbides would remain and some others would peel off from the matrix, generating a high roughness on the fracture surface). The crack would then propagate in the matrix and create the smooth surface outside the GBF, as shown in Figure 1.3.2 c) up to final fracture (Figure 1.3.2 d)). Further investigations showed that fine spherical carbides tended to peel off from the matrix, while large carbide particles were ruptured during the GBF formation process with cycling, as shown in Figure 1.3.2 c)). The reason why the fracture behaviour may be different for these kinds of carbides was found on the ability to adhere and deform between the carbide and the matrix.

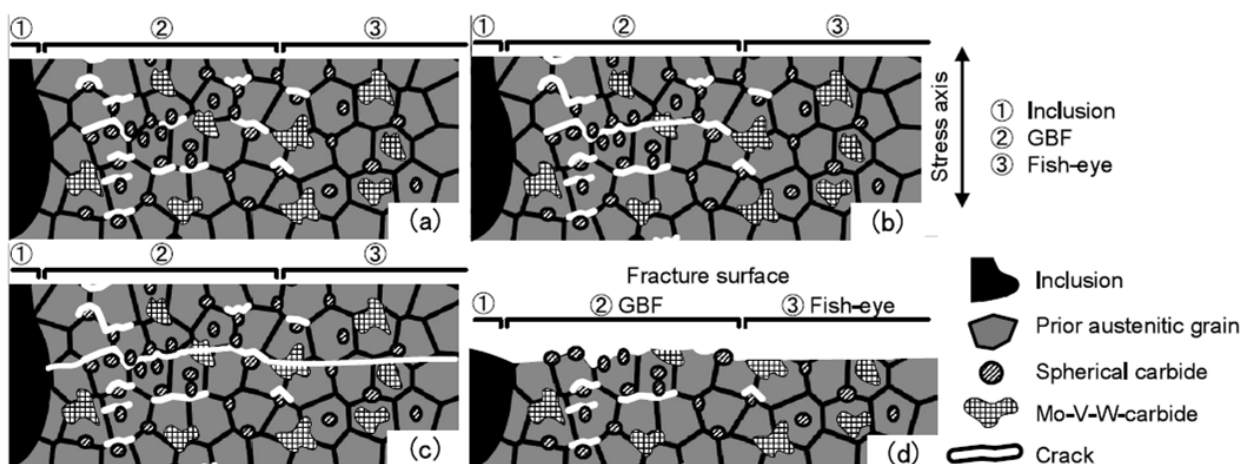


Figure 1.3.2 Proposed model, “dispersive decohesion of spherical carbide”, for the formation of the GBF area around an inclusion (black area on the left side of the images) during a very high-cycle fatigue process [SHI06-1]

A fatigue crack occurred at an inclusion due to the stress concentration without the formation of a GBF area, under high-stress amplitude levels and a low number of cycles. However, the formation of a GBF area near a non-metallic inclusion was required for a fatigue fracture in a VHCF regime, since the stress intensity factor calculated around an inclusion was found to lay below the threshold value for crack initiation and propagation [SHI06-2].

According to these findings, Fukaura et al. [FUK04] tested a JIS-SKD11 (AISI D2 type equivalent) tool steel up to 10^7 loading cycles and observed crack initiation at one or more primary carbide particles located at/close to the surface and in the interior of the specimens. The carbides were always found fractured (they were not debonded), with some dimples surrounding them. A closer interpretation of the results led the authors to the same conclusion that Shiozawa et al. had elaborated for high-speed steels; i.e. when the applied stress was high, fatigue fracture initiated from inclusion particles at the surface (one or more primary carbides were observed at the origin of fracture in case of JIS -SKD11 steel), but when the stress amplitude was reduced, a crack initiated near the surface (again at the primary carbides), formed in the interior and spread towards the outer surface.

In some specimens where the stress had been lower than 1100 MPa, the fracture initiation site was a fish-eye type and contained a fractured carbide particle in the centre, from which a round region of smooth surface developed. It is clear after the work of Fukaura et al. that fracture occurred only after the development of a fish-eye because the internally initiated and grown crack did not touch the specimen surface. However, they did not ascertain whether the fracture of large primary carbides was a precondition for the formation of the observed fish-eye, although this had been commonly assumed to be the trigger of the fatigue fracture in the literature [BER87].

Sohar et al. [SOH08-1, -2 and -3], in turn, performed a detailed fractographic study and quantitative evaluation of AISI D2 type cold work tool steel specimens tested in fatigue up to the 10^{10} loading cycles. These authors obtained both internal and at/near surface crack initiation, with a very flat morphology and fish-eye, or half of fish-eye, appearance respectively. In their work, five different zones in the fracture surface were distinguished, likely to be attributable to subsequent stages of fatigue crack growth. As shown in Figure 1.3.3, “2a” represented the region with very low surface roughness and in some cases some short cracks perpendicular to the fracture surface. This crack growth stage was followed by zone “2b” and “2c”, which both revealed a significantly rougher surface (no clear boundary was detected between the two but rather a gradual change). The area outside the fish-eye “3” corresponded to the final fracture surface.

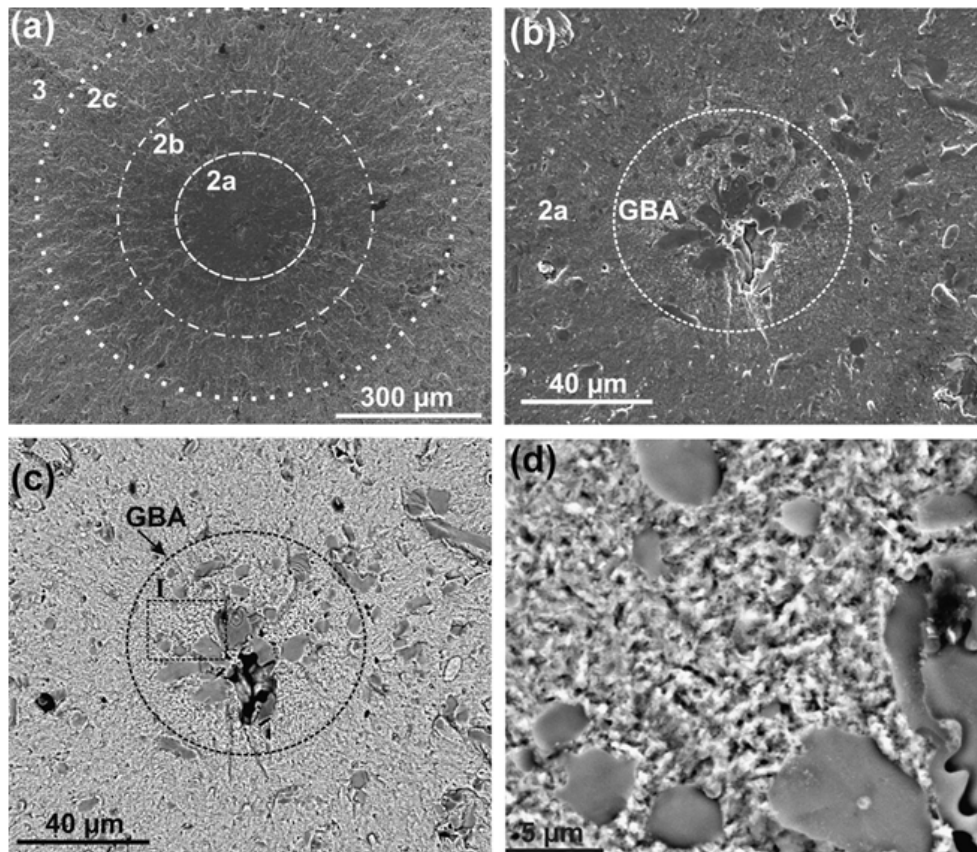


Figure 1.3.3 Fracture surface of AISI D2 type tool steel specimen failed after $6,1 \cdot 10^6$ cycles at 800 MPa: a) SEM image of internal fatigue crack nucleation and propagation zones; b) SEM image of GBF (or “granular bright area (GBA) as referred in the work of Sohar et al.) in the vicinity of the carbide cluster; c) and d) BSE images revealing the granular surface morphology within the GBF [SOH08-2]

Primary carbide clusters were observed in the centre of the fish-eyes, with GBF areas around them. Sohar et al. found that the “dispersive decohesion of spherical carbides” model developed by Shiozawa et al. applied satisfactorily in this steel. However, the work of Sohar et al. [SOH08-1, -2 and -3] was neither able to reveal whether the carbide fracture initiated the fatigue crack or if it was a result of fracture of the specimen.

1.3.1.2 Plastic damage mechanisms versus carbide fracture as fatigue crack initiators in tool steels

The work of Fukaura et al. [FUK04] tried to clarify the fact that at a low stress range, the monotonic tensile stress for carbide cracking was much higher than for fatigue. With the purpose of answering this question and knowing the stress required to break carbides, these authors proved the effectiveness of the Acoustic Emission (AE) technique to catch the breakage of carbides in the JIS-SKD11 steel. Fukaura et al. found that the beginning of AE signal observation occurred at 1100 MPa, which was much the same as that of the critical stress below which the fish-eye fracture was found to take place. However, it is not clear from the work of these authors why this AE signal was obtained at these stresses, or why it was in

good agreement with the maximum stress for fracture with fish-eye. The AE tests performed in this study did not clarify whether the determined stress values were predicted to correlate with carbides fracture or with an elastic breakdown. Nevertheless, these findings meant that fish-eye fracture would occur at applied stress amplitudes below the critical stress required to generate damage in the microstructure under monotonic loading conditions.

A better understanding of the correlation between AE signals and micro-damage in monotonic conditions was given by Yamada and Wakayama [YAM09]. Although these authors used AE monitoring to clarify the flexural fracture of cermets, they observed a rapid increase in cumulative AE energy prior to the final fracture and attributed this phenomenon to the maincrack formation. They also distinguished two types of AE signal: one was a burst-type signal with high frequency and the other was a continuous-type signal with low frequency. The former was considered to be emitted from microcracking while the latter was due to plastic deformation of the binder phase.

Yamada and Wakayama understood the microfracture process in cermets as follows:

- In a first stage both carbide grains and binder phase would have deformed elastically and no AE signal was observed.
- Secondly, the binder phase would have deformed plastically and a continuous-type signal with low frequency was detected. Some fractures at carbide/carbide and carbide/binder interfaces could also take place and corresponding burst-type signals were detected.
- In a third stage, a macroscopic crack would have initiated due to the coalescence of pre-existing flaws, such as pores, coarse carbide grains or carbide agglomerates. As a result the main crack which may lead to the final fracture could have formed.
- In stage four the main crack would have propagated stably. Simultaneously, small scale intergranular and interface fractures could have taken place at a large number of sites.
- Finally the maincrack would have propagated in an unstable manner.

Therefore, after the work of Yamada and Wakayama the AE signals correlate well with the observed microdamage in the microstructure prior to failure. However, these observations are not obvious to apply to fatigue, even though the work of Yokoi et al. [YOK03] using AE enabled to relate the carbide fracture stresses to the yield stress of the matrix in the JIS-SKD11 steel. Carbide breakage by cleavage was found to be likely produced by dislocations pinning at the carbide/matrix interface, since the stress concentration associated with dislocation pile-ups was thought to trigger the development of cracks. These authors observed that in low-cycle fatigue testing the most of the fatigue life was consumed in crack initiation processes, and that would mean that even if carbides use to be detected in the fracture initiation sites of tool steels, extrusion-intrusion mechanisms caused by the accumulation of damage in the specimen surface would be operative and they could cause carbide cracking.

In fact, cyclic loading is known to produce sharp peaks (extrusions) and troughs (intrusions) as a consequence of nonreversible slip, and these are actually considered the initial stage of microcrack formation in monocrystalline materials (where no large defects are present in the microstructure which can give rise to microcracks at earlier stages) [HER83].

Extrusions and intrusions represent the free surface terminations of dense bands, “persistent slip bands” (PSBs), of highly localized slip and their number increases also with strain range. Fukaura et al. [FUK04] observed cyclic softening in the overpeak-tempered cold-work tool steel JIS SKD11, and they understood this phenomenon as the tempered martensite structure destabilization by strain localization processes, such as PSBs and vein formation. It is believed that these PSBs are softer than the surrounding matrix material, resulting in a concentration of plastic strain. Although the cracking begins at the surface, the material within these PSBs and below the surface is also damaged and it can control the location of the nucleated cracks.

PSBs can be arrested at carbides or at grain boundaries, thereby contributing to crack nucleation at these two junctions. Fukaura et al. [FUK04] reported that if the steel had fine carbides and their volume fraction was small, the possibility of pinning up of dislocations to the carbides decreased, the carbides were difficult to fracture and the overall material response in fatigue was increased. Dougherty et al. [DOU96] studied the fatigue crack closure in a 1070M steel, with a tempered martensite microstructure, and also attributed the progressive decrease in cyclic stress response at low strain amplitudes to the formation of PSBs. They stated that in absence of local stress and strain concentrators, the intensified slip bands were the most likely sites for crack initiation. Later on, Mughrabi [MUG02] conveyed that in cyclic loading, a major part of fatigue life was spent in the bulk microstructural processes leading to cyclic strain localization in the form of PSBs and subsequent crack initiation.

1.3.2 Fatigue crack propagation mechanisms in tool steels

1.3.2.1 The notion of the stress intensity factor in fatigue: stress and crack length correlations with fatigue crack propagation

As discussed earlier, concepts of LEFM can successfully be applied in case of propagation of large cracks in the microstructure. Fatigue crack propagation processes have been commonly studied using the relationship proposed by Paris in which the stress intensity factor, itself a function of stress and crack length, is the overall controlling factor, as shown in Equation 1.3.1:

$$\frac{da}{dN} = A\Delta K^m \quad (1.3.1)$$

where da/dN is the fatigue crack growth rate, ΔK the stress intensity factor range ($\Delta K = K_{max} - K_{min}$) and A and m are function of material variables, environment, frequency, temperature, stress ratio, etc.

As shown in Figure 1.3.4, fatigue crack propagation processes can be separated into three regimes, with different ΔK dependences of the crack growth rate. At both low and high ΔK values, the crack growth rate increases markedly compared to the rather stable crack growth rate in the intermediate ΔK levels. The reason for these behaviours can be found since:

- At high ΔK levels, the plastic zone becomes large and also K_{max} approaches K_C , creating local crack instabilities by increasing amounts of microvoid coalescence and/or cleavage in the fracture surface.
- At the other end of the crack growth rate spectrum, for low ΔK level the fatigue crack propagation rate diminishes rapidly to a vanishingly small level. A limiting stress intensity factor range is then defined as the threshold level, ΔK_{TH} , and represents a service operating limit below which fatigue damage is highly unlikely. Thus, if $\Delta K < \Delta K_{TH}$, the fatigue crack will cease to grow; alternatively, if $\Delta K > \Delta K_{TH}$ the newly initiated fatigue crack will continue to grow to failure.

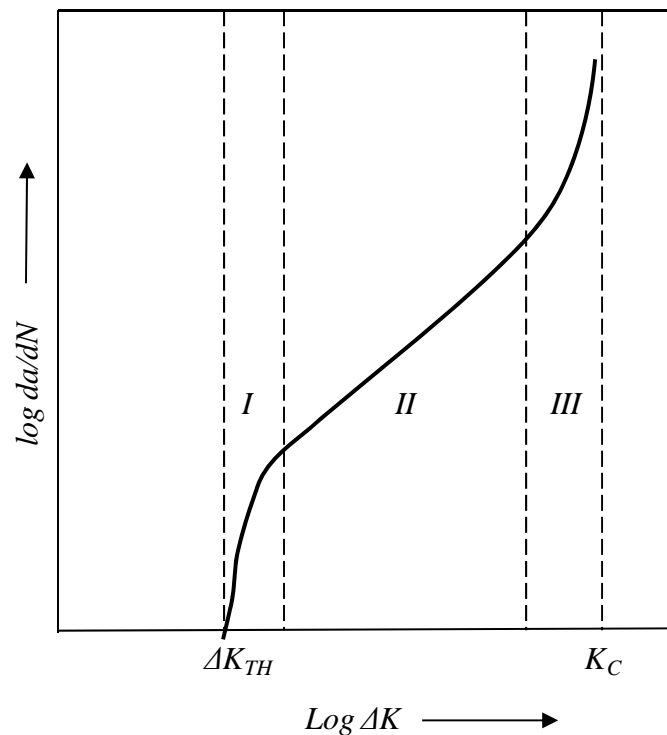


Figure 1.3.4 Diagram showing three regimes of fatigue crack growth response. Region I, crack growth rate decreases rapidly with decreasing ΔK and approaches lower limit at ΔK_{TH} ; Region II, midrange of crack growth rates where “power law” dependence prevails; region III, acceleration of crack growth resulting from local fracture as K_{max} approaches K_C

When the stress intensity factor range is low (resulting by low applied stress and/or small crack size), a small plastic zone is developed. When the material thickness is large compared to this zone size, plain strain conditions prevail and flat fracture usually results. With subsequent fatigue crack extension, the stress intensity factor and the plastic zone size increase. When the zone is large compared to specimen thickness, plane stress conditions and slant fracture are dominant. Therefore, depending on the stress level and crack length, the fractured component will possess varying amounts of flat and slant fracture. Consequently, a fatigue crack may start out at 90° to the plate surface but complete its propagation at 45° to the surface (Figure 1.3.5). Alternatively, the crack could propagate immediately at 45° if the plastic zone size to plate thickness ratio were high enough, reflecting plane stress conditions.

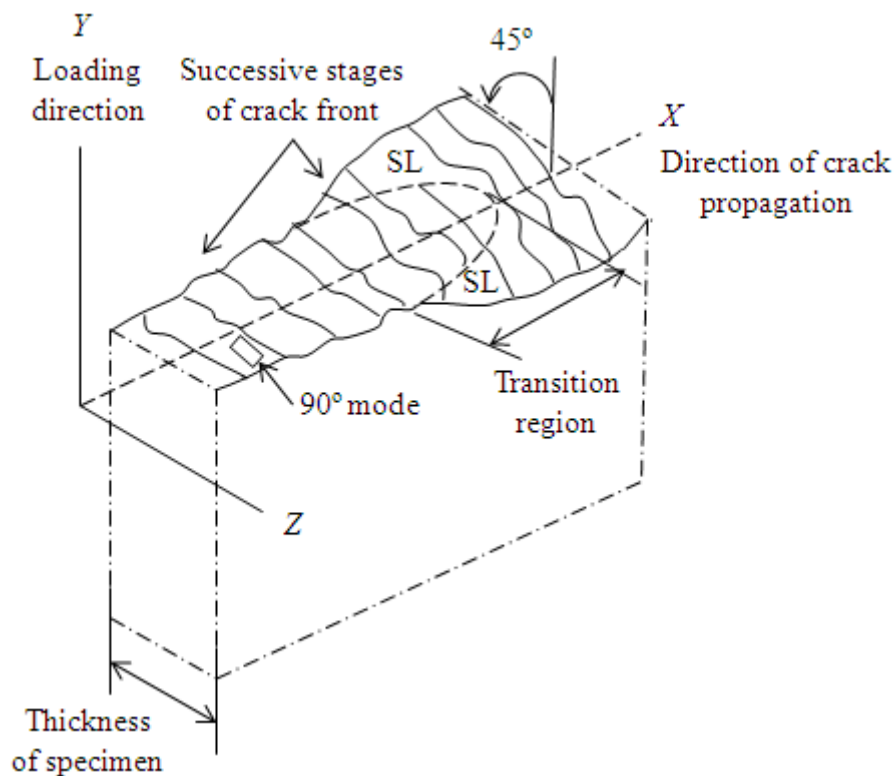


Figure 1.3.5 Diagram showing fracture mode transition from flat to slant fracture appearance

1.3.2.2 Growth of physically short cracks

Similar than for K_C (see chapter 1.2), physically short cracks can grow at ΔK levels less than those predicted using linear elastic fracture mechanics possibly due to an elastic breakdown. On one hand, the crack tip plastic zone dimension at a given ΔK level may become large when compared with the length of the physically short crack. Furthermore, continuum concepts would be expected to break down when the length of the crack is comparable to the dimension of the pertinent microstructural unit, such as the grain size. In this sense, at a given ΔK level, crack growths are faster when the cracks are physically short, before converging at longer crack lengths.

However, due to the plastic zones at the crack tip and the plastic deformation process, a crack might be partially closed during part of the loading cycle, even when R , the ratio between the minimum to the maximum stress, is higher than 0 [HER83]. Residual tensile displacements resulting from the plastic damage of fatigue crack extension would interfere along the crack surface in the wake of the advancing crack front and cause the crack to close above the minimum applied load level. In other words, the crack would be partially closed for a portion of loading cycle and would not open fully until a certain opening K level, K_{op} , is applied. As a result, the damaging portion of the cyclic load excursion would be restricted to that part of the load cycle which acted on a fully opened crack.

It is most important to note that a fatigue crack could initiate and then grow at a decreasing rate to the point where the effective crack-driving force (perhaps some plasticity and crack closure-modified function of ΔK) decreases below the threshold value for continued crack advance (Figure 1.3.6). At this point, the crack would cease to grow with the fatigue limit of practical interest being based not on initiation, but on the higher stress level needed to cause propagation and a “non-propagating crack” would be created [HER83]. That is, a fatigue crack would initiate but then would not propagate to failure. The presence of these non propagating cracks is consistent with the fact that fatigue crack growth essentially ceases when the stress intensity factor decreases below the threshold level, ΔK_{TH} .

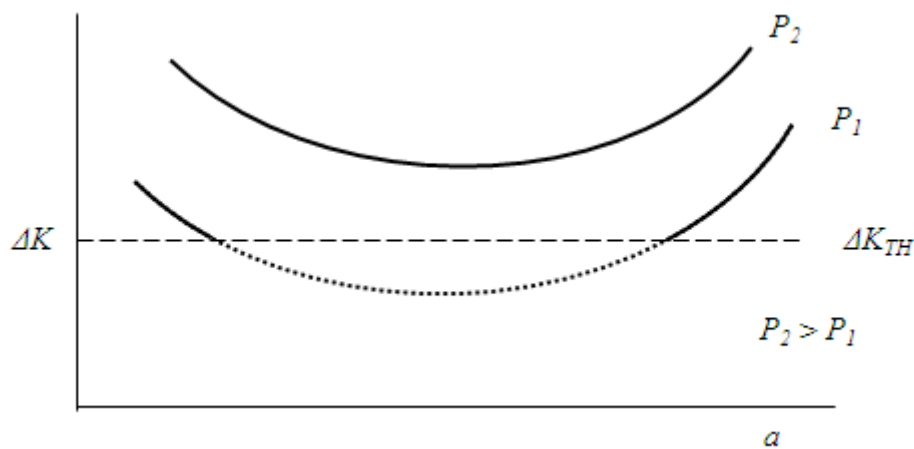


Figure 1.3.6 Effective ΔK level as a function of crack length at two load levels. At P_1 , ΔK will decrease below ΔK_{TH} as a crack moves through notch root zone. Crack arrest will then occur

1.3.2.3 Microstructural aspects of fatigue crack propagation in tool steels

There is a major influence of metallurgical variables on fatigue crack propagation at both low and high ΔK levels. Conversely, fatigue crack propagation at intermediate ΔK levels is relatively microstructure insensitive. The transition from microstructure-sensitive to microstructure-insensitive crack growth behaviour is associated with a concomitant transition in fracture mechanisms. Below some critical ΔK level, a highly faceted fracture surface appearance is developed in conjunction with a highly branched

crack front. Above this ΔK range, the fracture surface is much smoother overall and covered with fatigue striations. At the same time, the crack front is no longer bifurcated.

The transition from structure-sensitive to structure-insensitive behaviour also influences the dependence of the macroscopic growth rate on the applied ΔK level, as noted by the slope change drawn in Figure 1.3.7. It follows that with increasing the size of the relevant phase, the transition to structure-sensitive behaviour should occur at higher ΔK levels. Consequently, the fatigue crack propagation rate of these materials should decrease in the regime below ΔK_T with increasing grain size. The threshold conditions are established when the slip band at the crack tip is unable to traverse the nearby grain boundary. This should occur when the slip band size or the cyclic plastic zone dimension is approximately equal to the average grain diameter. Since the plastic zone size varies with the square of the stress intensity factor, it follows that the stress intensity level associated with the threshold condition should increase with increasing grain size.

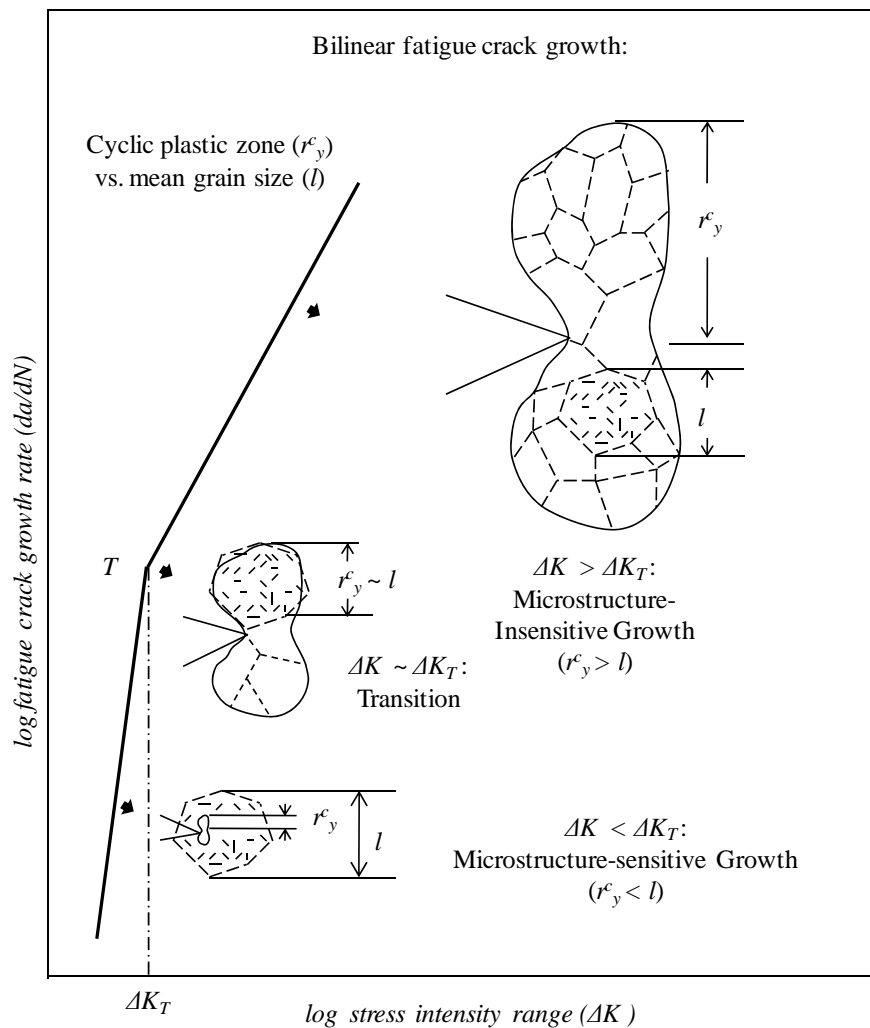


Figure 1.3.7 Bilinear fatigue crack growth behavior. Microstructure - sensitive behavior observed when reversed plastic zone < mean grain size. Microstructure - insensitive mode occurs when reversed plastic zone > mean grain size

However, it is important to recognize that the critical dimension which acts as effective barrier to slip depends on the material and may correspond to grain size, Widmanstätten packet dimension, sub-grain size or the dislocation cell dimension. In some martensitic high strength steels, prior austenite grain boundary might not be the structural parameter that controls thresholds behaviour in this material but instead, the martensite-lath boundary could serve as the effective slip band barrier.

Berns et al. [BER87], in turn, reported that stable fatigue crack growth in the intermediate Paris regime was rather independent of large discontinuities in the microstructure of PM and cast and hot worked steels, but it was controlled by the matrix, which was similar for all the specimens. However, at the near threshold stress intensity regime, some differences in crack growth were observed. The explanation offered by these authors consisted in the following: at low ΔK levels, the matrix plastic zone diameter at the crack tip would be large enough in PM steels to promote carbide-matrix boundaries to fail and thus, instability of the main crack. Contrarily, in the cast and hot worked specimens the carbide band spacing would stay above the plastic zone, thereby rising the critical ΔK values for crack growth.

According to these results, Højerslev et al. [HØR02] observed that fatigue crack growth in notched high-speed steels samples subjected to four point bending tests was affected by the microstructure until a crack length of up to five hundred microns had grown. Near the notch, the carbide damage zone was found to be large but after a few hundred microns of crack growth, the main carbide damage occurred within a zone of radius 5 μm . Consequently, carbide fracture would have occurred when a threshold load value was reached. Several changes in crack path were observed in the vicinity of fracture carbides and that was explained if the cracked carbides showed a lower fracture energy path in the matrix. In this sense, fractured carbides would be expected to attract an approaching matrix crack, whereas intact carbides would be expected to repel it, because the Young's modulus of the carbides is significantly larger than that of the matrix.

The maximum applied loads corresponded to stress values below the estimated yield strength of the steel, thereby it was apparently impossible to initiate fatigue crack growth at such applied loads since they would be too low to cause carbide damage (and crack initiation was thought to require the presence of fractured carbides). Some investigations of the crack paths showed that a threshold value was required to cause carbide damage, but when this value was exceeded the carbides failed immediately.

The mechanism how fractured carbides caused matrix crack initiation was tentatively explained by Højerslev et al. [HØR02] as follows: a microscopic notch associated with a fractured carbide gave rise to a plastic strain field in the matrix and the affected matrix volume increased with carbide size; consequently, cyclic micro-plasticity and eventually damage may have been introduced in the matrix. Damage was more likely to occur if there was interaction among the cyclic strain fields of adjacent

cracked carbides. Such energy effects become particularly critical if preferred orientations of the carbide cracks prevail. However, it was also observed that fatigue crack propagation does not need to include a carbide damage zone. These authors showed that the relevant mean free carbide spacing is roughly equal the plastic deformation zone for the steels studied. Consequently, the crack was able to propagate through the matrix without cracking of carbides.

Jesner et al. [JES06] studied the fatigue crack initiation in notched samples under compression loading (between nominal stress levels of -3300 MPa and -330 MPa) of two PM steels, and they stated that due to stress concentration, plastic deformation occurred in the notch root from the first loading cycle on. This deformation was thought to induce residual tensile stresses after unloading and with the subsequent cyclic loading it would cause accumulated plastic strains in the notch root. The accumulation of cyclic plastic deformation caused crack initiation was supported further by the generation of residual tensile stresses. Figure 1.3.8 shows the notch surface after cyclic loading and indicates that carbide cracking, decohesion of carbides from the metallic matrix and crack initiation within the metallic matrix took place even after 10 cycles.

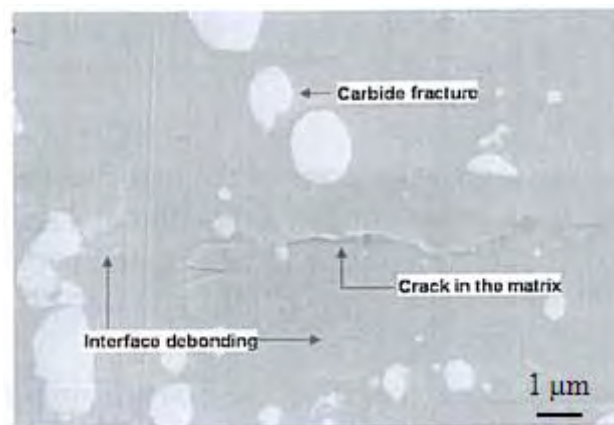


Figure 1.3.8 SEM micrograph of the notch surface after 10 loading cycles [JES06]

Jesner and Pippin studied also the fatigue crack growth behaviour at different stress ratios in a PM steel grade [JES09] and, based on fractographic observations of the fracture surface area, they showed that different fatigue crack propagation mechanisms were acting in the near threshold region and in the upper Paris regime respectively. Figure 1.3.9 a) illustrates the fracture mechanism in the near threshold regime, in which the fatigue crack grew predominantly in the matrix (around carbides) and cleavage of particles took only place when the crack front approached the particle near its midsection plane. In the upper Paris regime, in turn, some particles were observed to be cracked parallel and perpendicular to the macroscopic crack plane, as shown in Figures 1.3.9 b) and c), and this was attributed to the large stresses of the crack tip. The existence of broken carbides in the advancing crack front was found to accelerate the fatigue crack propagation at K levels near the fracture toughness.

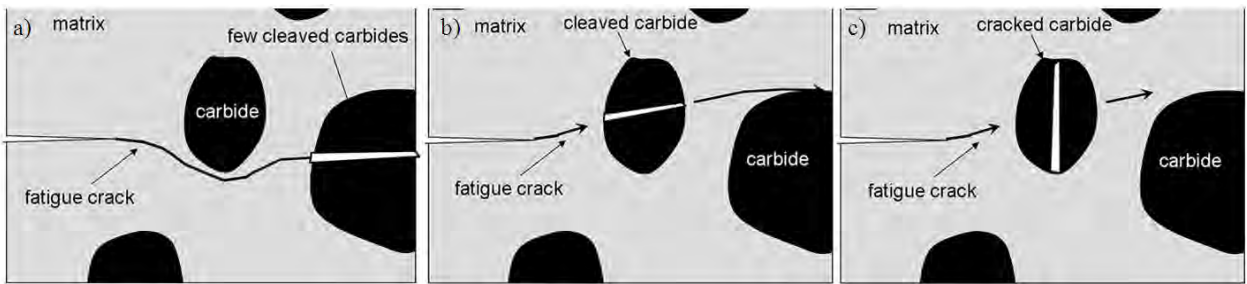


Figure 1.3.9 Schematic representation of the different fracture mechanisms in quenched and tempered PM steel in the: a) near threshold region and b) and c) upper Paris regime with crack propagation with cleaved carbide in the crack growth direction and normal to it respectively [JES09]

From this standpoint, in this Thesis the behaviour of different tool steels in fatigue will be assessed in order to determine if the mechanisms of crack propagation of short, medium and long cracks are governed by similar mechanical properties to those determined by means of standard tests. In this way, the main arguments reported in the literature which are summarised in this section will be contrasted with the results of the present investigation. The interaction of the microstructural constituents during crack nucleation and propagation mechanisms will be evaluated as well, and the origins of fatigue cracks will be deeply examined. These findings will contribute to reach the 2nd, 3rd and 4th objectives of this Thesis.

1.4 Failure in tools for shearing Ultra High-Strength Steels

1.4.1 The shearing process

Shearing is the most frequent applied manufacturing method in sheet metal working and it consists in the separation of metal by two blades moving as shown in Figure 1.4.1. In this process, a narrow strip of metal is severely plastically deformed to the point where it fractures at the surfaces in contact with the blades. The fracture then propagates inward to provide complete separation. The depth to which the punch must penetrate to produce complete shearing is directly related to the ductility of the metal; the penetration is only a small fraction of the sheet thickness for brittle materials, while for very ductile materials it may be slightly greater than the thickness.

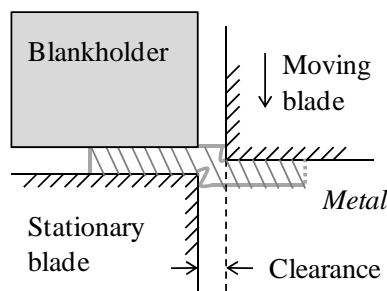


Figure 1.4.1 Shearing of metal sheet

In shearing operations the application of a blankholding force is required in order to prevent the sheet from sliding. The clearance between the blades is an important variable to provide a clean fracture surface since with the proper clearance the cracks that initiate at the edges of the blades propagate through the metal and meet near the centre of the thickness. Insufficient clearance can produce a ragged fracture (Figure 1.4.2 a)) and also requires more energy to shear the metal than when there is proper clearance. In contrast, with excessive clearance there is greater distortion of the edge and more energy is required because more metal must plastically deform before it fractures. Furthermore, with too large clearances, burrs or sharp projections are likely to form on the sheared edge (Figure 1.4.2 b)). The height of the burr increases with increasing clearance and increasing ductility of the metal. Because the quality of the sheared edge influences the formability of the part, the control of clearance is important and thus, the clearance generally ranges between 2 and 10 percent of the sheet thickness (the thicker the sheet the larger the clearance).

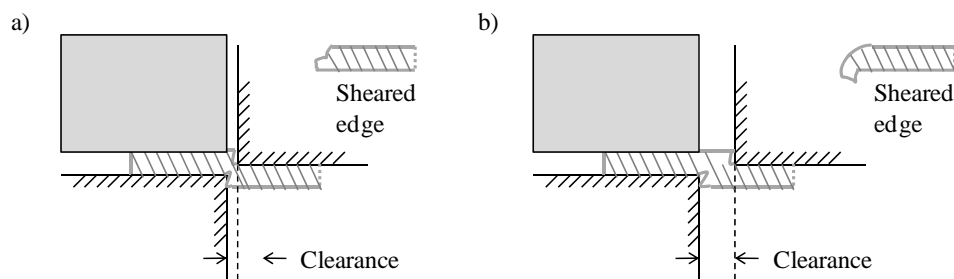


Figure 1.4.2 Shearing with: a) insufficient clearance; b) excessive clearance

The shearing process can be divided into five phases, as shown in Figure 1.4.3 a). In the first phase the blankholder and the upper blade come in contact with the sheet. It follows in the second phase, the elastic deformation of the sheet under the acting vertical force. The cutting force acts all along a narrow zone of the cutting edge so that the distance between the resulting force and the cutting edge generates a moment, which produces bending of the sheet under the upper blade and slightly lifting from the lower blade. The elastic deformation turns into plastic deformation and forms the rollover zone, as shown in Figure 1.4.3 b). With the increasing penetration of the upper blade into the sheet, shearing results with the bright zone formation in phase three. Once the stress generated in the sheet exceeds its fracture strength, small fractures nucleate and propagate, creating the fracture zone. At the moment of breaking the elastic stresses are suddenly released (phase IV) and this leads to a very high impact shock for the tool and the press. In phase V the upper tool returns upwards [SO08].

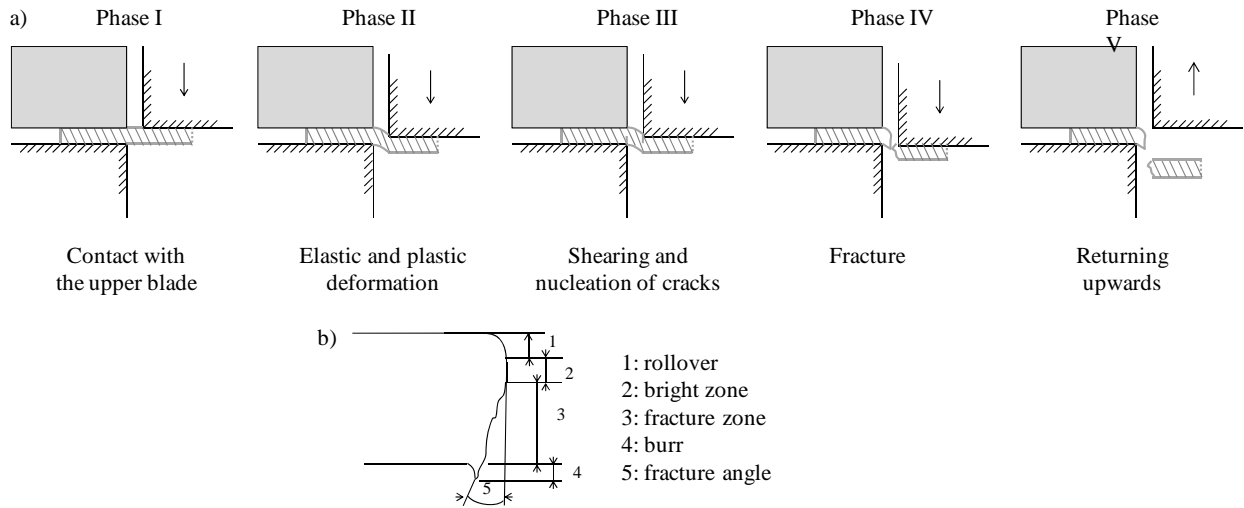


Figure 1.4.3 a) Phases of the shearing process; b) schema of the sheared edge

The maximum force required to shear a metal, F_{Smax} , is the product of the length cut, L , the sheet thickness, t , and the shear strength, k_s , as shown in Equation 1.4.1:

$$F_{Smax} = t \cdot L \cdot k_s \quad (1.4.1)$$

k_s can often be assumed equal to $0,8 \cdot \sigma^R$, where σ^R is the fracture strength of the material. However, in case of materials with very high strengths, k_s is usually lower and it is estimated as $0,6 \cdot \sigma^R$ [UDD06]. The shearing force can be reduced appreciably by making edges of the cutting tool at an inclined angle, so that only a short part of the total length of cut is made at one time (Figure 1.4.4). Then the shearing force can be rewritten as:

$$F_{Smax} = \frac{t^2 \cdot k_s}{2 \tan \alpha} \quad (1.4.2)$$

The shearing force increases during elastic and plastic deformation of the workpiece, and decreases once the first cracks start to appear, as shown in Figure 1.4.4.

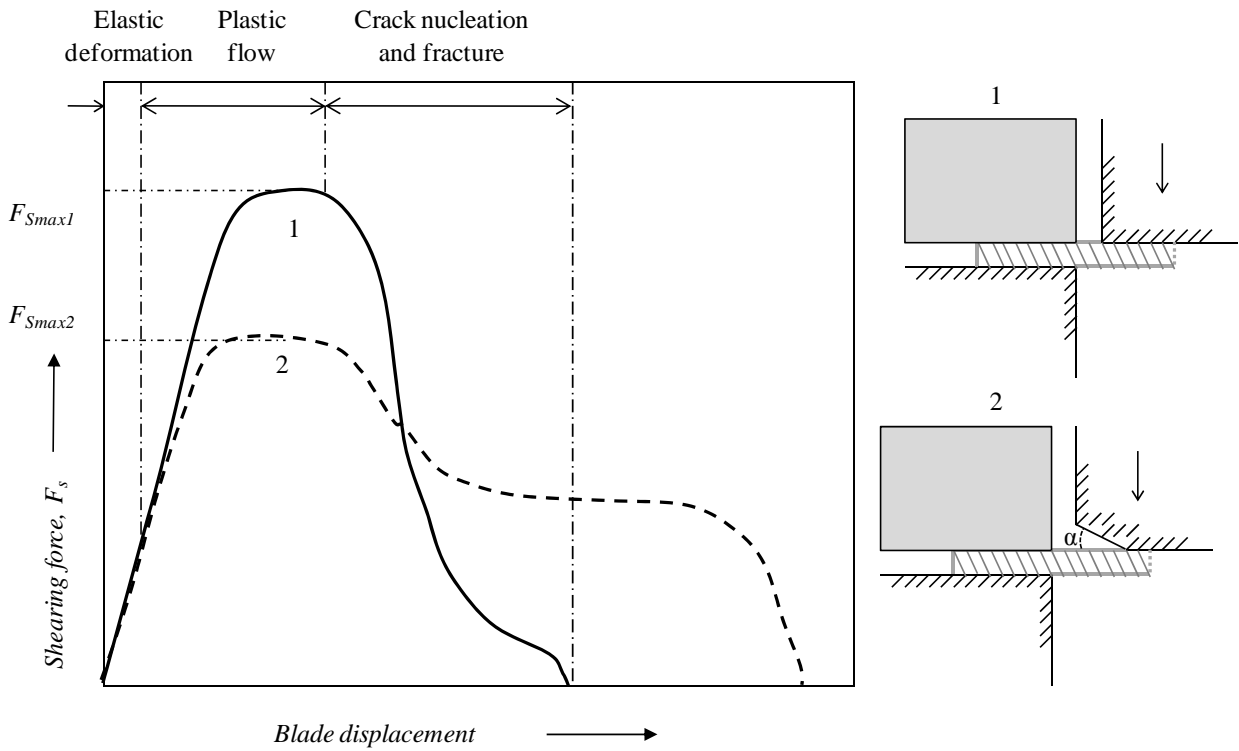


Figure 1.4.4 a) Phases of the shearing process; b) schema of the cut edge

However, the resulting force in the cutting edge can be divided into two components (vertical, F_V , and horizontal, F_H), which lead to a bending moment, as shown in Figure 1.4.5.

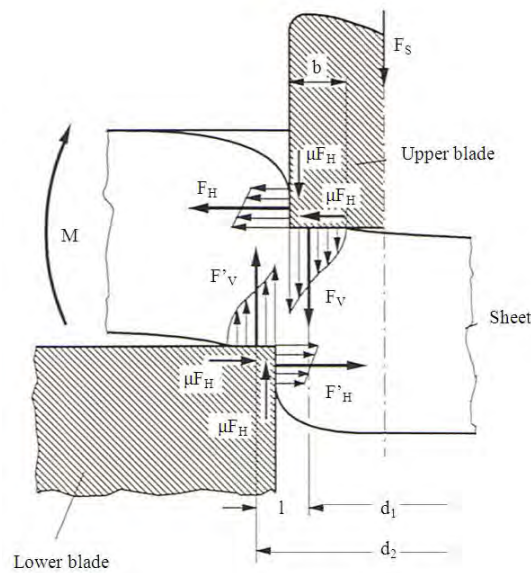


Figure 1.4.5 Components of the shearing force, F_S : vertical force, F_V , horizontal force, F_H , and bending moment M [adapted from LAN90]

Both forces derive from the friction between the workpiece and the blades and result to a lateral force, F_{RS} , which is highly related to the clearance, the sheet thickness and the hardness of the workpiece and can be estimated as a percentage of the shearing force as follows:

$$F_{RS} = (0,02 \dots 0,2)F_S \quad (1.4.3)$$

A whole group of press operations are based on the process of shearing, as briefly described in the following lines:

- Blanking is the shearing of closed contours, when the metal inside the contour is the desired part, (Figure 1.4.6 a)).
- Punching or piercing is known as the shearing of closed contours, if the material inside the contour is discarded (Figure 1.4.6 b)).
- Punching indentations into the edge of the sheet is called notching (Figure 1.4.6 c)).
- Parting is the simultaneous cutting along at least two lines which balance each other from the standpoint of side thrust on the parting tool (Figure 1.4.6 d)).
- Slitting is a shearing cut which does not remove any metal from the sheet (Figure 1.4.6 e)).
- Trimming is a secondary operation in which previously formed parts are finished to size, usually by shearing excess metal around the periphery (Figure 1.4.6 f)).
- Finally, fine blanking is a process in which very smooth and square edges are produced in small parts such as gears. The sheet metal is tightly locked in place to prevent distortion and is sheared with very small clearances on the order of 1 % at slow speeds. Usually the operation is carried out on a triple-action press so that the movements of punches, hold down ring, and die can be controlled individually.

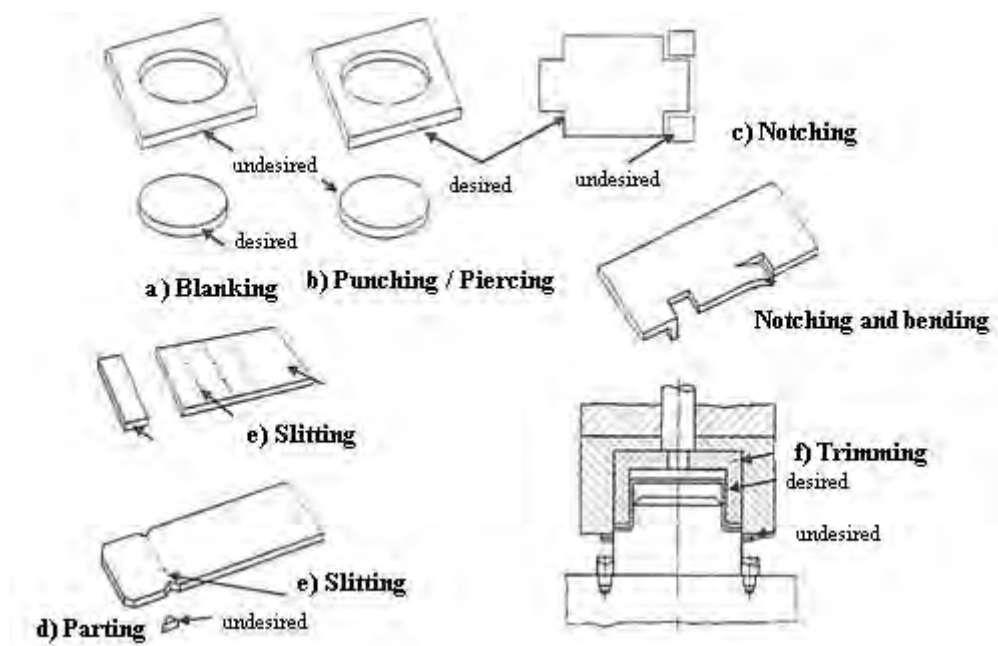


Figure 1.4.6 Shearing processes [adapted from LAN90]

1.4.2 Ultra High-Strength Steels

Characteristic High-Strength Steels (HSS) have yield strengths from 210 to 550 MPa and tensile strengths from 270 to 700 MPa, while Ultra High-Strength Steels (UHSS) (named also as Advanced High-Strength Steels (AHSS)) have yield strengths greater than 550 MPa and tensile strengths greater than 700 MPa [WAS09]. The main difference between conventional HSS and UHSS is their microstructure, determining their strength. Conventional HSS are single phase ferritic steels with some pearlitic islands whereas UHSS are primarily multi-phase steels which contain ferrite, martensite, bainite, and/or retained austenite in quantities sufficient to produce unique mechanical properties. The high strength of UHSS at very thin gauges makes them suitable for being applied in auto body components to reduce the weight of vehicles and improve their safety performance.

The metallurgy and processing of UHSS grades is somewhat novel compared to conventional steels. The most common UHSS are DP (Dual-Phase), TRIP (Transformation Induced Plasticity), CP (Complex Phase) and MS (Martensitic) steels and they all are produced by controlling the cooling rate from the austenite or austenite plus ferrite phase. Recently, it is possible to control the cooling rate from prior austenitization and thus, the final microstructure of the steel, directly in the forming press. Manganese-Boron steels (22MnB5) have been developed with the aim to be shaped by hot stamping. The high quenchability of these steels makes them suitable to be rapidly cooled in the press in contact with the tools and allow to obtain complex parts with totally hardened microstructures (high amounts of martensite and just small content of bainite or ferrite) and tensile strengths above 1500 MPa. Figure 1.4.7 schematically compares the UHSS with other steel grades in terms of total elongation and tensile strength.

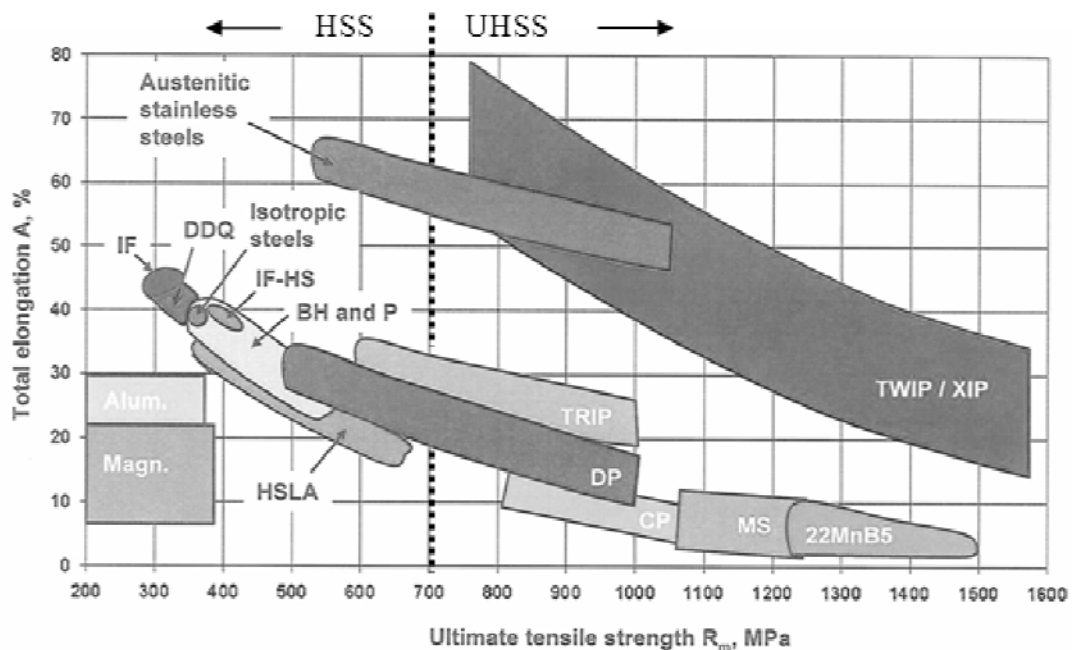


Figure 1.4.7 Schematic of UHSS compared to HSS [KOG09]

1.4.3 Damaging mechanisms of tools

Due to the high strength of UHSS, shearing processes of these steels are extremely tedious so as to be performed by mechanical means. The high loads required to shape them generate very high stresses and contact pressures in tools, which lead to their premature fracture by fatigue and accelerated wear. Since the introduction of UHSS in the industry is rather new, there is no extended knowledge in the literature concerning the damaging mechanisms of the tools employed to shape them. However, similar damage mechanisms have been already observed by several authors in other types of cold forming processes, such as cold forging. The very high mechanical loads registered in cold forging tools and their iterative application lead to severe damage by fatigue and cracking due to accumulation of plastic strain, together with wear. Thus, the failure mechanisms acting in tools for shearing UHSS can start to be discussed on the basis of the existing knowledge about processes involving high mechanical solicitations in tools, as cold forging, amongst others.

Accordingly, Nagao et al. [NAG94] analyzed by means of Finite Element (FE) computer simulation the stress states that existed in the inserts for cold forging during forming operations and determined the causes of the fatigue failures observed in industrial tools. The authors showed that the formation of a plastic zone at the transition radius of the lower insert was responsible for the initiation of fatigue cracks, as shown in Figure 1.4.8, while the tensile maximum principle stresses that developed at the radius under the forging load were responsible for the propagation of these cracks. In this area, the maximum principle stresses were found to change their circumferential direction to a direction tangential to the radius and their compressive magnitude to a tensile value; so the crack path followed the planes of the maximum shear stress.

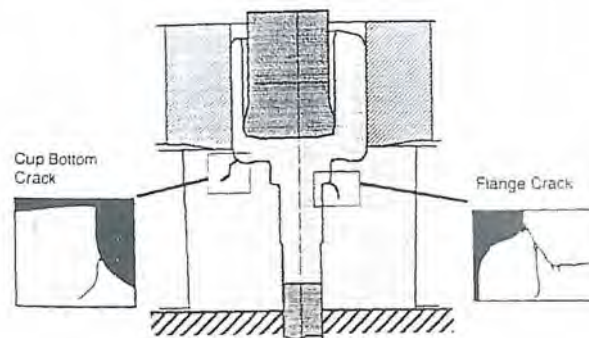


Figure 1.4.8 Location of the two crack sites in the lower set of the backward extrusion tooling [NAG94]

Pedersen [PED97] presented a model which using FE analysis, was suitable for describing effects of cyclic loading in cold forging tools, i.e. cyclic softening or hardening and mean stress relaxation. The method made possible to account for the redistribution of stresses in the damaged region and considered that in the low cycle fatigue regime undergone by tools, fatigue damage evolved with the accumulation of plastic strain due to cyclic loading, typically near the inlet of the radius transition region (as shown in

Figure 1.4.9). This author found that at the first load cycle, as pressure was applied, the material yielded in the radius transition region but, except for this area, almost the entire insert was found to deform elastically. Thus, at the end of the load cycle, as the pressure was decreased, the elastic energy stored in the body led to reversed yielding in the region near the fillet and this cyclic deformation pattern was assumed to be responsible for the plastic strain accumulation and development of damage.

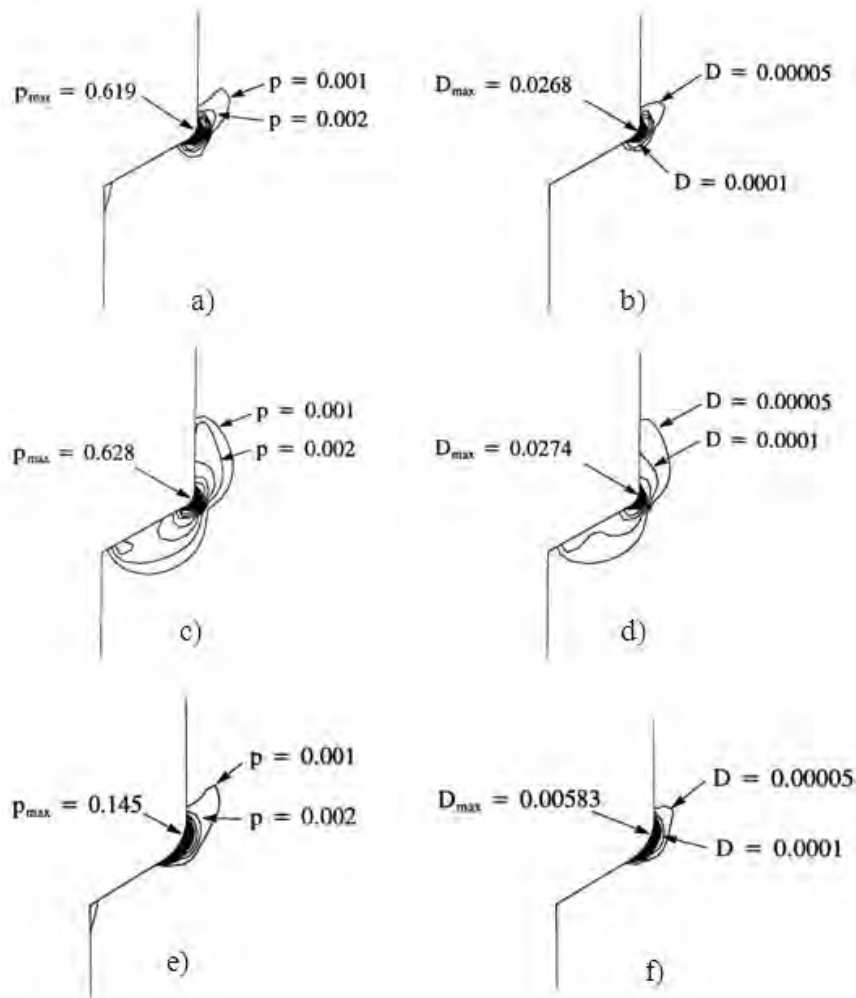


Figure 1.4.9 Contours of accumulated effective plastic strain, p , and damage, D , in the radius transition region after 50 subsequent load cycles: a) fillet radius A, p , prestressed die; b) fillet radius A, D , prestressed die; c) fillet radius A, p , die without prestress; d) fillet radius A, D , die without prestress; e) fillet radius B ($B > A$), p , prestressed die; f) fillet radius B ($B > A$), D , prestressed die [PED97]

Dubar et al. [DUB01] in turn, worked in wear related failures of cold forging tools. These authors proposed wear criteria to define the degradation state of cold forging tools and developed a sliding test allowing to reproduce the real contact conditions developed during the process and also a numerical model able to quantify the friction stresses responsible for seizure at the tool-workpiece interface. The tool steel employed in their tests was uncoated AISI M2 and the evolution of wear at the first number of cycles showed that while surface roughness decreased up to a stabilized value, particles produced by abrasive wear started to plough in the tool surface. After 5000 cycles, scratches and dominant abrasion

phenomena were observed and after 20000, the scratches were deeper and the abrasive features more pronounced. The friction stresses increased at the tool-workpiece interface with the number of cycles and they also showed a large scattering. This scatter was found to be responsible for the seizure in the tool surface because it strongly modified the shape of the produced parts and plastically deformed a particular zone in the tool.

Vinter Dahl [VIN02] studied the fractography of a cold forging tool made of AISI M3:2 steel and the mechanisms of crack growth. Chipping was observed when two or more small cracks grew together and a flake of material was loosened and fell off whereby the crack was expanded. This author stated that cracks occurred in a brittle cleavage like manner near the surface, as shown in Figure 1.4.10 a). Since several cracked carbides could be observed in the bottom of the crack (Figure 1.4.10 b), Vinter Dahl noted that the initiation of the main crack in the tool could be linked to the cracking of carbides in the area where the fracture took place, even though this did not provide evidences enough to confirm it.

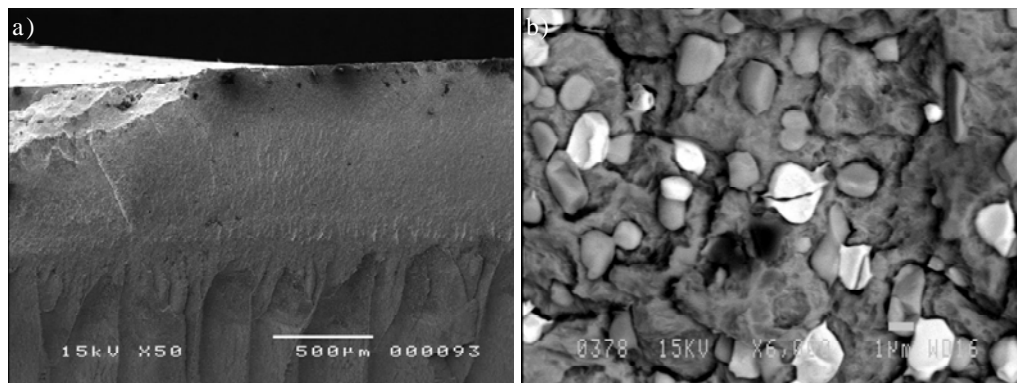


Figure 1.4.10 SEM-SE picture of: a) an opened specimen. In the top left corner, the part of the crack that is visible in the unopened specimen can be seen. In the lower part of the picture the crack running inside the specimen can be observed; b) fractured carbides in the bottom of the crack [VIN02]

Krishnadev and Jain [KRI07] performed a detailed metallographic analysis of microstructures and fractures of cold working tools to identify the sources and mechanisms of failure. These authors found that in an AISI D2 die for trimming aerospace components, cracks initiated and propagated by linking up along parallel carbide stringers, even though they also deviated and propagated along carbide colonies, as shown in Figure 1.4.11 a). The non-uniform microstructure with large angular carbides as shown in Figure 1.4.11 b), made easy the initiation of microcracks due to high stress concentration, grow and linking up, resulting in a drastic reduction of the die service life.

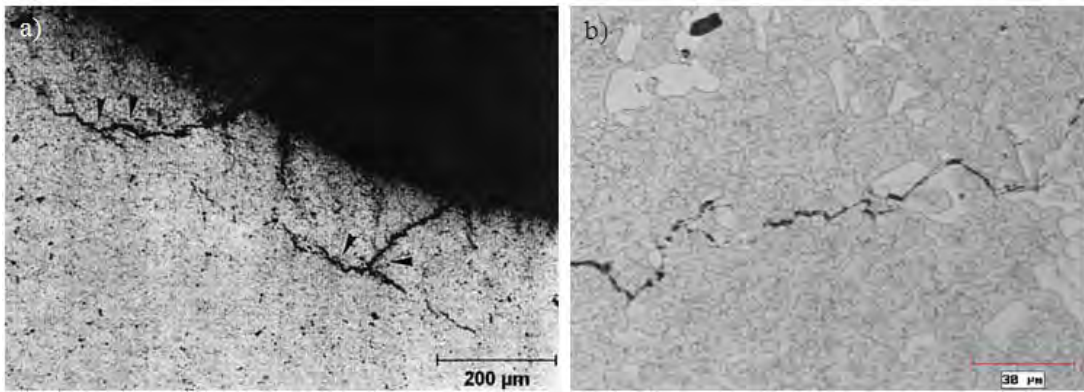


Figure 1.4.11 a) Crack morphology showing crack link up and propagation along aligned carbide stringers; b) crack propagation along angular carbides [KRI07]

These authors listed the factors that determined the integrity of the working edges of trimming dies as follows:

- Wear resistance, which depended on the hardness, the type and the volume fraction of carbides.
- Cutting edge strength, or the ability of the tool material to resist rounding off or deformation of the cutting edge.
- Compressive yield strength, which determined the risk of suffering from plastic deformation.
- Toughness, or the ability of the cutting edge to resist cracking, macro-chipping and micro-chipping.

Boniardi et al. [BON06] performed a fractographic study to identify the origin of damage in carburized and nitrided gears. The authors found that the formation of surface and subsurface cracks was the main failure mechanism in gears and they directly attributed the nucleation of these cracks to the locally very high Hertzian contact pressures generated, which led to very high values of peak shear stresses (beyond the endurance limit of the material). The mechanism explaining the fracture process could be divided in the following steps:

- Firstly, the asperities present in the surface were polished by very local material removal and thus, the area of effective contact became larger. The pressure was redistributed on the surface and the phenomenon was arrested.
- In a second stage, some initiated superficial cracks propagated (usually inclined with a shallow angle to the surface) in the forward direction of the rolling contact.
- The cracks went deeper for few microns, but instead of resurfacing, they developed secondary branches which created sub-superficial layers at a considerable distance from the surface, as shown in Figure 1.4.12 a).
- However, some cracks initiated deeper below the surface in the points where the ratio between the shear stress and the fatigue strength of the material was the highest. The applied load led the

material to a local plastic deformation and some micro cracks nucleated and propagated following planes parallel to the surface of the teeth.

- Finally the cracks resurfaced and large pieces of material were detached (Figure 1.4.12 b)).

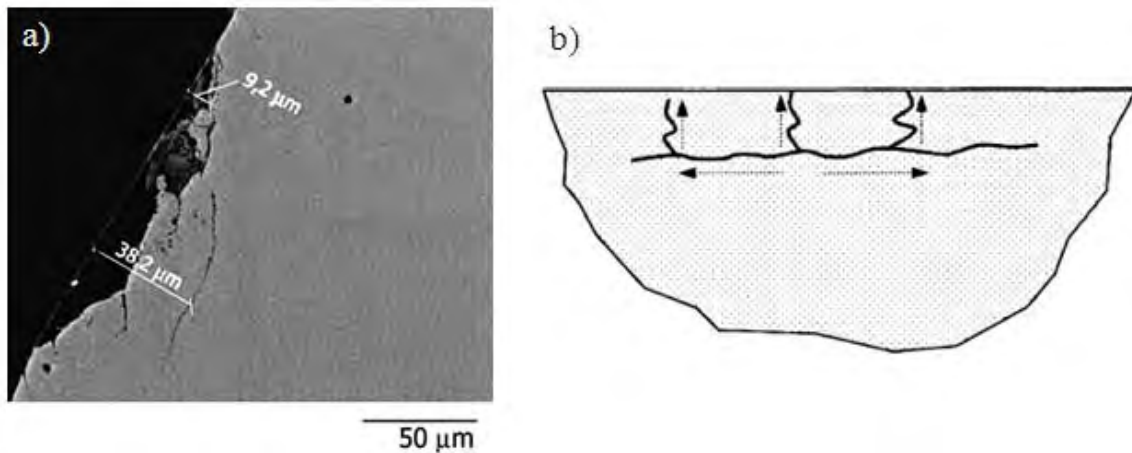


Figure 1.4.12 a) Example of superficial micro-chipping in presence of branching phenomena; b) Diagram of coplanar advancement of a sub-superficial crack, with a propagation towards the surface along perpendicular directions (the arrows show the direction of fatigue propagation) [BON06]

Luo [LUO99] studied the main failure mechanisms acting in punching tools after piercing thick AISI 52100 steel plates. The punch material was a high-speed steel of PM type, hardened and tempered to 65 - 67 HRC. Luo classified the damage observed in tools into the following categories:

- Side wear
- Face wear
- Chipping
- Cracking
- Gross fracture

In side wear (Figure 1.4.13 a)) some metal layers were adhered to or welded onto the side surfaces of the punch and the friction forces increased progressively. These forces led the side face to produce micro-fractures and pits (or voids) as a result of the development of surface fatigue cracks. Primary and secondary cracks in the surface were caused by the action of repeated stress cycles during the punching process, and resulted in liberating wear particles and formation of pits and voids. The side surface of the punch also showed grooves and valleys, which were related to abrasive wear. Thus, damage on the punch side was found to be a combination of adhesive, fatigue and abrasive wear. Side wear would cause the internal diameter of the punched holes to become small, it would lead to an increase of the clearance between the punch and the die and furthermore, the deformation (edge draw-in) of the workpiece during shearing would also be increased.

Face wear (Figure 1.4.13 b) caused the punch to become round and obtuse due to mechanical attrition and micro-chipping. Face wear was responsible for the reduction of the sharpness of the punch during shearing and the increase of the deformation and burrs of the punched workpiece. Chipping (Figure 1.4.13 c) occurred when the punch appearance showed some micro-fractures, fragments and breakage on the cutting edges, possibly due to the action of the repeated loads. If the surface of the punch was too rough or if the turning feed marks of the machining process were retained, then chipping of the punch cutting edges occurred easily.

Cracking appearance (Figure 1.4.13 d) displayed many irregular microcracks on the face of the punch edges and it was the result of mechanical fatigue during shearing. When these microcracks propagated further during shearing, the punch edges produced chipping, or in an extreme case, macro-fracture. In gross fracture (Figure 1.4.13 e) the beach markings on the cyclically grown portions of the fracture were a result of fatigue failure.

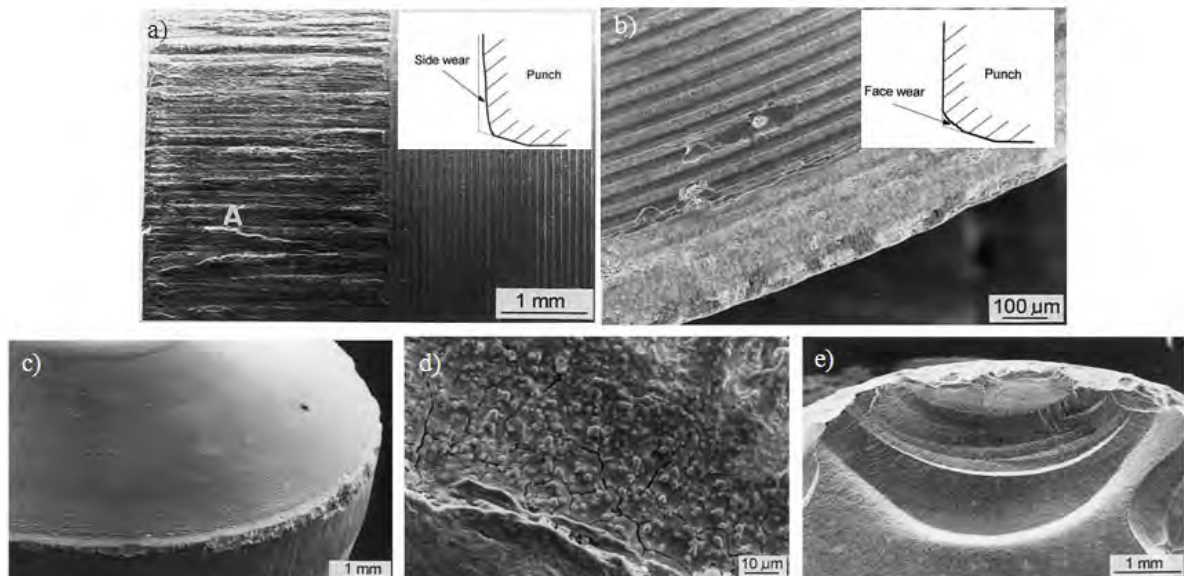


Figure 1.4.13 Classification of the main damaging mechanisms observed in punching tools after piercing larger thickness plates of AISI 52100 steel: a) side wear; b) face wear; c) chipping; d) cracking; e) gross fracture [LUO99]

Wear has typically been a main inconvenience in cold working tools. Thus, many authors such as Pereira et al. [PER08], Ersoy-Nürnberg et al. [ERS08], or Hambli [HAM01 and HAM03] studied in detail the evolution of the contact pressure at the die radius in sheet metal stamping and they developed FE models to simulate and predict wear. Högman [HOG02], in turn, investigated the effect of the cutting clearance and the influence of this parameter in the wear type and distribution on the punch. He performed blanking tests using different tool steel materials (Calmax, Sverker 21, Sleipner, Vanadis 4 and Vanadis 6), and Docol 1400 DP, Docol 800 DP and conventional mild steel as sheet materials and he concluded that wear increased markedly with the resistance of the sheet steel.

Blanking of Docol 800 DP was found to produce galling at the surface of tools, and Högman attributed this phenomenon to the presence of ferrite in this steel. In case of Docol 1400 DP, fatigue cracks in the punches started to be observed after 80 – 100000 strokes and they were much worn out than for Docol 800 DP. Högman also tested some coated punches (using one CVD type (TiC) and three PVD types (TiCN, TiAlN, TiN)) and he found that despite they improved the performance in Docol 800 DP (where galling was the main inconvenience), they did not in Docol 1400 DP (because the coating did not prevent the microcracks to form in the substrate).

Hence, fatigue cracks and chipping are actually a main concern in tools for shearing the highest strengths families of UHSS since they cannot be prevented following the strategies conventionally applied in the forming industry to increase the performance of tools (consisting in increasing hardness to improve the wear resistance or applying hard coatings). In this context, many investigations have been devoted in the last few years to optimize the strategies to cut UHSS [SO09, MAC10, etc.]. Jonsson et al. [JON08], Krönauer et al. [KRÖ10] and Mackensen et al. [MAC10] performed semi industrial cutting tests and blanking tests using high performance stamping presses and extremely stiff test tools with special characteristics to resist the lateral forces. They studied the influence of the process parameters, such as the cutting edge radius or the clearance, in the cut edge profile of the parts and in tools wear. Nevertheless, the performance of tools must also be improved from a microstructural point of view, regarding the effect of the microstructural constituents of tool materials in its macro and micro-mechanical behaviour during service and in this sense, there is a lack of publications and still a big field for research so far.

In this sense, this Thesis will shed light on the phenomena involved in the failure events taking place in tool steels during cold forming and shearing processes of UHSS and PHS and contrasted to the published data in the literature. Damage of tools will be analysed from an in depth microstructural and micro-mechanical point of view and the results will be rationalised in basis of the operational features such as applied loads, surface conditions, clearance and tools radii, etc. Accordingly, the 5th objective of this Thesis will be attained.

1.5 Methods for tool life prediction

Failure prediction of engineering components is often desirable to establish safe operating service lives, to compare the mechanical performances of different materials, set maintenance and reparation tasks, or to determine the most affecting parameters to the recorded life. Fatigue life calculations are then required since many of these components are subject to fatigue loads. In the following lines some of the most relevant fatigue life calculation models applied in case of tool steels are reviewed, together with the most recent patented methods developed to estimate tooling lives.

1.5.1 Existing models for fatigue life prediction based on LEFM

Such a computation is well known and it has been applied since decades to predict failure of engineering materials provided that cracks are already present in the microstructure (the assumption of negligible time for nucleation in front of propagation must be valid in these materials). The model runs with the integration of Equation 1.3.1 (known as Paris law), considering that $\Delta K = Y \cdot \Delta \sigma \cdot a^{1/2}$, with the starting, a_0 , and final flow size, a_f , as limits of the integration. When the geometrical correction factor Y does not change within the limits of integration, the cyclic life, N , is given by:

$$\frac{da}{dN} = A \Delta K^m = A (Y \Delta \sigma a^{1/2})^m = AY^m \Delta \sigma^m a^{\frac{m}{2}} \quad (1.5.1)$$

$$N = \int_{a_0}^{a_f} \frac{da}{AY^m \Delta \sigma^m a^{\frac{m}{2}}} = \frac{1}{AY^m \Delta \sigma^m} \int_{a_0}^{a_f} \frac{da}{a^{\frac{m}{2}}} \quad (1.5.2)$$

$$N = \frac{2}{(m-2)AY^m \Delta \sigma^m} \left[\frac{1}{a_0^{\frac{m}{2}-1}} - \frac{1}{a_f^{\frac{m}{2}-1}} \right] \quad (1.5.3)$$

where $\Delta \sigma$ is the stress range and A and m are material constants. Usually however, this integration cannot be performed directly, since Y varies with the crack length. Consequently, cyclic life may be estimated by numerical integration procedures by using different values of Y held constant over a number of small crack length increments. It can be seen from equation 1.5.3 that when $a_0 \ll a_f$ (the usual circumstance) the computed fatigue life is not sensitive to the final crack length a_f , but instead, is strongly dependent on estimations of the starting crack size a_0 [HER83].

Meurling et al. [MEU01] developed a model for predicting the fatigue limit of tool steel specimens considering that inclusions and carbide particles acted as fatigue crack initiation sites. The model was based in fracture mechanics and it was assumed that a specimen would fail if it contained at least one broken carbide or inclusion particle which had a critical size. It was also assumed that cracks existed in all particles already before fatigue testing, and that they had the same size as the particles.

According to these assumptions, these authors built up a model using Poisson's statistics and upon the following considerations:

- Around all particles such as carbides and inclusions, cracks existed of equal size as the initiating particles.
- An existing crack would not grow unless the stress intensity at its tip would exceed the stress intensity threshold for crack propagation.

-If there existed at least one crack for which the stress intensity exceeded the threshold value, then this crack would eventually propagate to cause failure of the specimen.

Meurling et al. estimated the stress intensity ranges for the crack initiating particles at internal inclusions and carbides using the following the expression:

$$\Delta K = 2 \cdot \Delta\sigma \cdot \sqrt{\frac{D}{2\pi}} \quad (1.5.4)$$

where D is the equivalent particle diameter and $\Delta\sigma$ the stress range. A defect was defined by these authors as critical if its stress intensity exceeded the threshold for propagation, ΔK_{TH} (ΔK_{TH} was assumed equal to $4 \text{ MPa}\cdot\text{m}^{1/2}$, since all the studied steels showed values around this value). Therefore, the critical size of a particle was defined as:

$$D_c = 2\pi \cdot \left(\frac{\Delta K_{TH}}{2 \cdot \Delta\sigma}\right)^2 \quad (1.5.5)$$

As there is no single carbide size in tool steels, a statistical approach accounting for the distribution of carbides sizes was applied. Provided that the cumulative size distribution of the initiating defects was known, i.e. primary carbides and inclusions respectively, the expected number of critical defects in a volume of stressed material, λ_c , was estimated using the expression:

$$\lambda_c = \iint_{V_{D_c}}^{\infty} \sqrt{\frac{2k}{\pi D}} \cdot f k \cdot e^{-kD} \cdot dD \cdot dV = f \cdot \sqrt{\frac{2k^3}{\pi}} \cdot \iint_{V_{D_c}}^{\infty} D^{-\frac{1}{2}} \cdot e^{-kD} \cdot dD \cdot dV \quad (1.5.6)$$

where $N_A(D)$:

$$N_A = f \cdot e^{-kD} = \int_D^{\infty} f \cdot k \cdot e^{-kD'} \cdot dD' \quad (1.5.7)$$

was an exponential function describing the cumulative size distribution of carbides or inclusions (Figure 1.5.1 a) and b) respectively) and it was fitted using an exponential function with f and k constants obtained from the curve fitting.

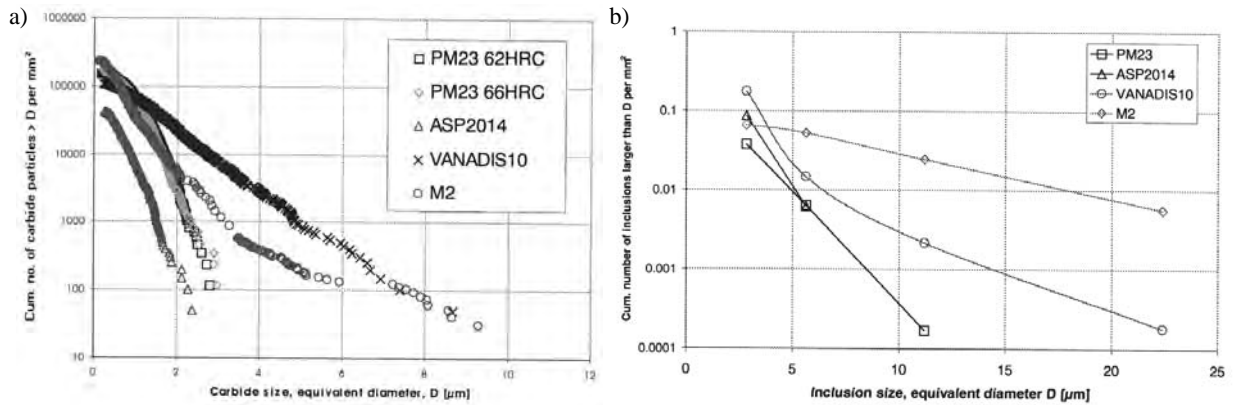


Figure 1.5.1 a) Carbide size distribution presented as cumulative number of carbides with size larger than a certain equivalent diameter plotted vs carbide diameter; b) cumulative number of inclusions with size larger than a specific value plotted vs inclusion size. PM23, ASP2014 and VANADIS 10 were PM steels and M2 was ingot cast [MEU01]

Once the expected number of critical defects, λ_c , was estimated, the probability of finding a certain number of critical defects, n , in a volume of material was calculated using Poisson's statistics:

$$p(n) = \frac{\lambda^n}{n!} \cdot e^{-\lambda}, n = 0, 1, 2, 3, \dots \quad (1.5.8)$$

According to around all particles, cracks existed of equal size as the initiating particles, if there existed at least one crack for which $\Delta K > \Delta K_{TH}$, this crack would eventually propagate to failure; the specimen would fracture if n equals any number except zero, i.e. at least one critical defect existed. Then, the fracture probability, P_f , equaled one minus the probability that there existed no critical defects ($n = 0$ in Eq. 1.5.8):

$$P_f = 1 - e^{-\lambda_c} \quad (1.5.9)$$

In general, the results obtained by Meurling et al. regarding the application of this model in different tool steels: PM23, ASP2014, VANADIS10 and M2 steels showed good agreement in experimental and predicted fatigue limit values (Figure 1.5.2). However, in case of VANADIS10 and M2 steels slight differences were observed, which were attributed by the authors to the fact that their model did not account for the clustering of the initiating carbide particles and their non-spherical shape.

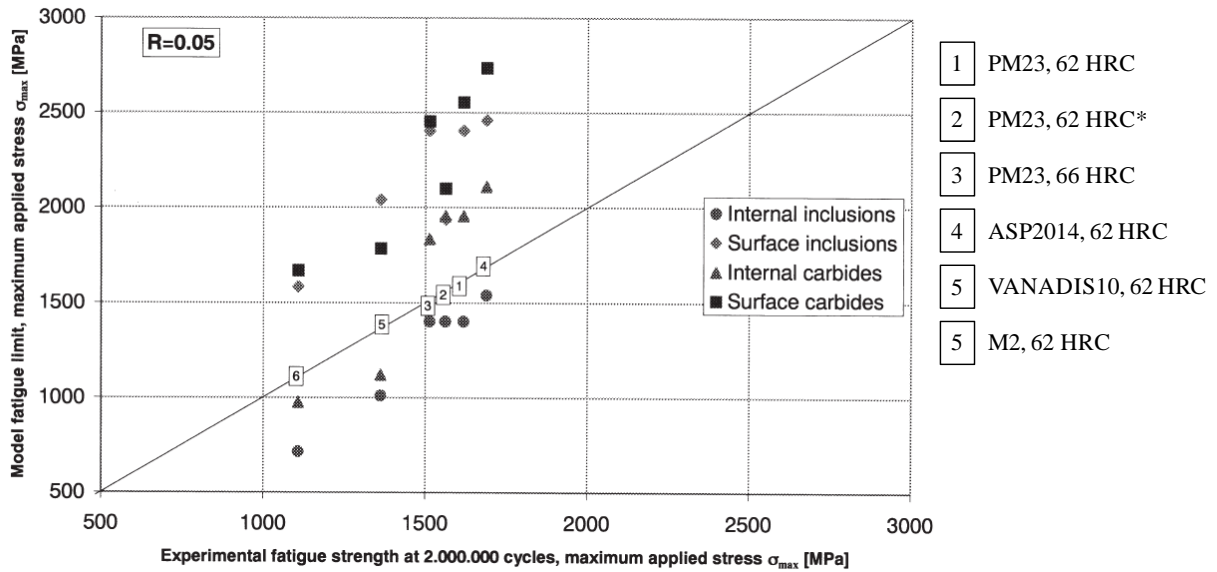


Figure 1.5.2 Model fatigue limit vs experimental fatigue strength at $2 \cdot 10^6$ cycles. *PM23 was longitudinally ground instead of hard-turned and polished as the rest of specimens [MEU01]

In order to palliate this limitation of the model, Melander et al. [MEL02] rewrote Equation 1.5.4 assuming that a cluster of carbides could cause a fatigue crack of the same size as the cluster, instead of a single carbide or inclusion (as it was assumed initially by Meurling et al.). That crack would be expected to be permanently arrested if the range of stress intensity of the crack at the cluster was below the threshold value for fatigue crack propagation, ΔK_{TH} . If however, the range of stress intensity was above the threshold value, then the crack would grow and the specimen would eventually fail.

$$\Delta K = 2 \cdot \Delta \sigma \cdot \sqrt{\frac{DCR}{2\pi}} \quad (1.5.10)$$

Melander et al. proposed the expression shown in Equation 1.5.10 based on a semi-circular crack in an infinite medium, where DCR was the diameter of the crack of the cluster. A cluster was defined as a volume V of material within which the volume fraction of carbide phase was larger than a critical value, f_c , as shown in Figure 1.5.3 a). The critical carbide fraction should be so large that a crack could form on the equator plane of the cluster early in fatigue life, as shown in Figure 1.5.3 b). It was found that this would mean that the volume fraction f_c was between 0,25 and 0,75. If cracks were easily generated around the individual carbides in the cluster, these cracks would then be expected to grow rapidly the short distances between the carbides, so an equatorial crack in the cluster was to be formed (Figure 1.5.3 c)).

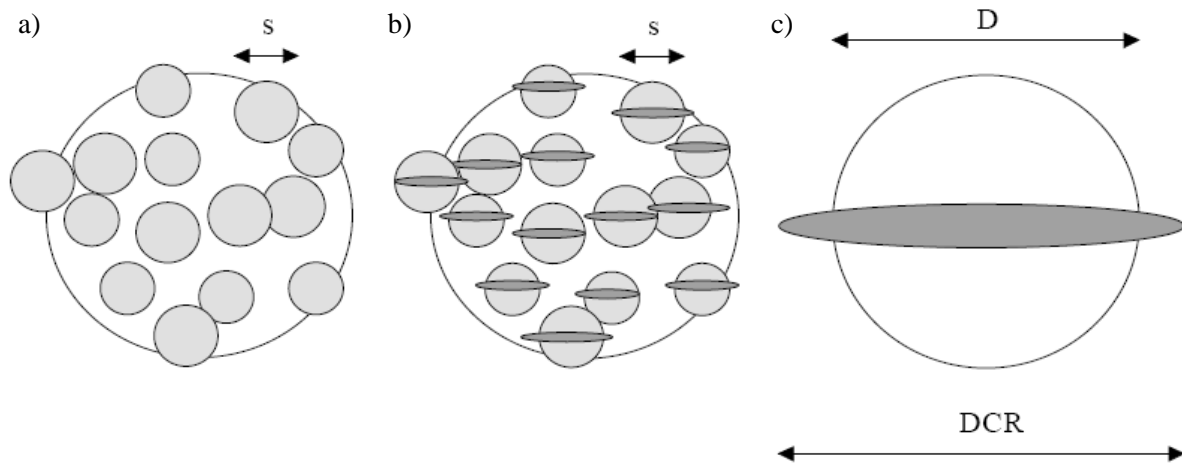


Figure 1.5.3 a) Cluster of carbides; b) cracks at carbides in a cluster; c) crack through cluster [RAN08]

The authors made the simplification that all carbides had the same size, s , and that the carbides and cluster were spherical. All carbides which had centers inside the cluster sphere, D , belonged to the cluster but since some of these carbides would extend partly outside the cluster sphere, the cluster diameter was considered as $DCR = D + s$.

Melander et al. introduced these modifications in the model developed by Meurling et al. and calculated the failure probability of the steels VANADIS10, M2, PM23 and ASP2014, using the same carbide distribution parameters as Meurling et al., but assuming f_c values of 0,5 and 0,25 (Figures 1.5.4 a) and b) respectively). The steels were however, found to fail at lower stresses than predicted from carbide clustering at 2 million cycles, with one exception namely VANADIS10 for $f_c = 0,25$. These results meant that carbide clusters played a role just in case of the fatigue failure of VANADIS10 (where the average carbide fraction was around 25 % and the carbide size around 2,5 μm) but that clusters played a minor role in the other steels.

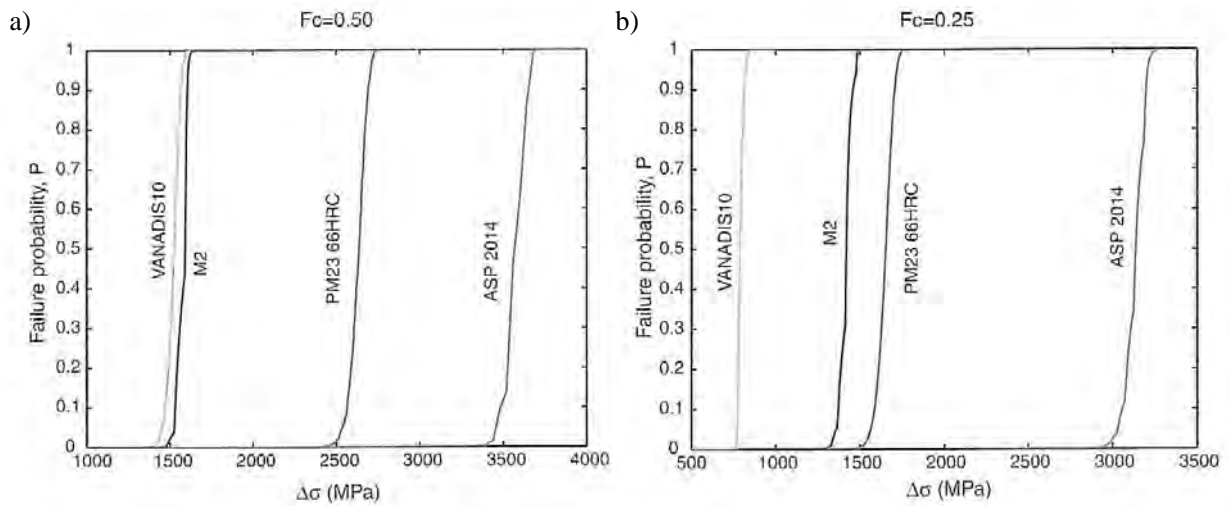


Figure 1.5.4 a) Failure probabilities for the steels VANADIS10, M2, PM23 and ASP2014 with $f_c = 0,5$; b) failure probabilities for the steels VANADIS10, M2, PM23 and ASP2014 with $f_c = 0,25$ [MEL02]

1.5.2 Existing patents on methods to predict damage of tools

There are few patents dealing with methods to predict damage in tools by breakage, wear, or the combination of both, and they can be separated depending on their approach. However, none of them has been found helpful predicting fatigue failure of tool steels in shearing operations of UHSS, as described in the short summary below:

- A first approach consisted in the instrumentation of industrial tools in order to measure physical data and transform them into feature values for tool life prediction. This was done thanks to the use of different computer signal treatments, which computed an average of the received signals, identified and classified them as indicative for the total life, and finally determined a security factor related with the given probability of duration [RAM93]. Other authors estimated the tool life by means of quantifying the changes in the registered load and the accumulation of all of them [TOR95]; or by comparing the registered load with a threshold value previously defined, above or below which failure was considered to take place [MAE08].
- The second approach used FE modelling to simulate fatigue fracture or wear phenomena by means of introducing algorithms based on aspects from fracture mechanics or the Archards's law [ARC56] respectively ([WAY94], [LIU07] and [ERS08]). Another work studied the relationship between the von Mises and the principal stresses acting in tools and compared the values at each element with a threshold value previously calculated [YOS06-1].
- Finally, the third approach to predict lives of tools dealt with the analysis of plastic deformation in tools and its evolution during forming processes by means of an equation relating the von Mises stress with the yield stress and a cyclic softening coefficient [YOS06-2].

From the standpoint presented in this section and according to the 6th objective of this Thesis, the adequacy of the aforementioned models based on LEFM to predict tool performances will be determined, as well as their limits of application and the requirements to estimate the life and performance of tools with increased accuracy. Finally, taking into account the knowledge gained throughout this investigation, a new approach to predict tool lives based on micro-mechanical damage will be introduced in order to succeed the 7th and last goal of the Thesis.

2. Experimental procedure

2.1 Material

Four different cold work tool steels are considered in this Thesis. The first type is a conventional ledeburitic high-carbon, high-chromium tool steel DIN 1.2379 (AISI D2). The second type is also a ledeburitic steel but with lower content of chromium, named K360 ISODUR and produced by BÖHLER EDELSTAHL GMBH & CO KG. The third and fourth types are a special grade of cold work tool steel developed by ROVALMA S.A., named UNIVERSAL and HWS respectively, which in comparison to the aforementioned materials have lower carbon and chromium content but higher of vanadium. 1.2379, K360 and UNIVERSAL are obtained by ingot metallurgy routes while HWS is produced by powder metallurgy. The main alloying elements found in their chemical composition are shown in Table 2.1.1.

Table 2.1.1 Main alloying elements in the chemical composition of the studied steels (in wt %)

Steel	C	Cr	Mo	V	W	Others
1.2379	1,5 – 1,6	11,0 – 12,0	0,6 – 0,8	0,9 – 1,0	-	-
K360	1,2 – 1,3	8,0 – 9,0	2,0 – 3,0	1,0 – 1,5	-	+ Nb +Al
UNIVERSAL, HWS	0,9 – 1,2	6,8 – 8,5	-	2,5 – 3,0	1,1-1,4	-

Prismatic samples were extracted from forged and annealed commercial bars with their major axis oriented perpendicular (D1), parallel (D2) and transverse (D3) to the forging direction. Forging results in the elongation and dispersion of the primary carbides forming bands aligned in the same direction, thus each type of sample configuration showed different carbide orientations as schematised in Figure 2.1.1.

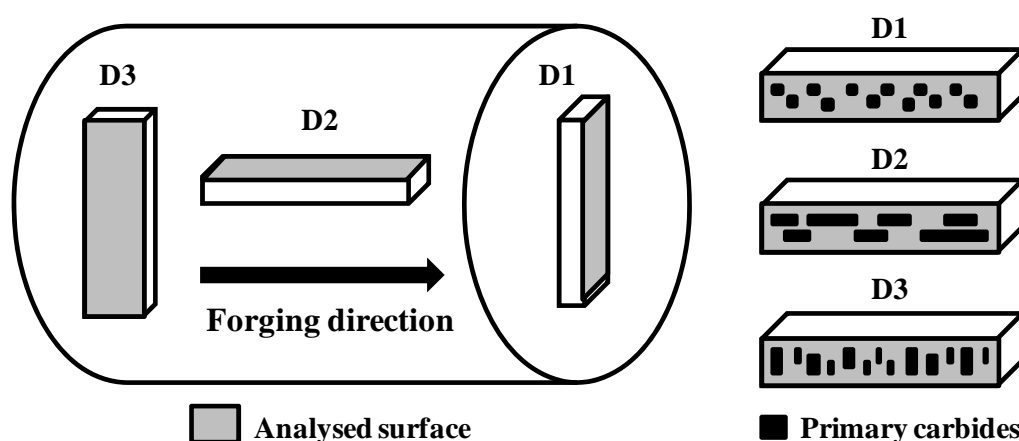


Figure 2.1.1 Sampling: samples perpendicular (D1), parallel (D2) and transverse (D3) to the forging direction

Heat treatment was applied to the samples of each material in order to get a hardness level of 60 – 62 HRC, as summarized in Table 2.1.2.

Table 2.1.2 Heat treatment applied to the studied materials and obtained hardness level

Steel	Austenitizing (quench in oil)	Tempering	HRC
1.2379	1050 °C for 30 min	550 °C for 2 h (x2)	60 - 62
K360	1060 °C for 30 min	450 °C for 2 h (x3)	60 - 62
UNIVERSAL, HWS	1060 °C for 35 min	540 °C for 2 h (x3)	60 - 62

2.2 Microstructure analysis

D2 samples were mechanically ground and mirror-like polished using colloidal silica particles with approximately 40 nm sizes for microstructure inspection using a FE-SEM (Field Emission Scanning Electron Microscope), equipped with EDX (Energy Dispersive X-Ray Spectroscopy) detectors for chemical analysis. The size distribution of the primary carbides was determined by means of image analysis using a minimum of 15 images for each material. Backscatter detection was employed to contrast carbides and metallic matrix and classify carbides with different chemical compositions. Images were randomly taken at 500X in 1.2379, K360 and UNIVERSAL, and at 7000X in HWS according to its smaller carbide size (as it can be observed in Figure 2.2.1).

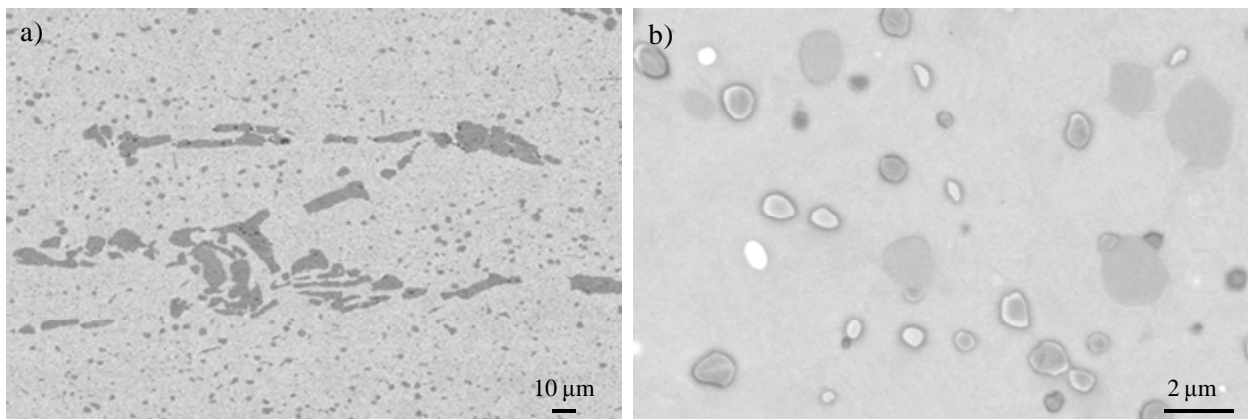


Figure 2.2.1 Images obtained by SEM using backscatter detection: a) 1.2379 and b) HWS

Carbide sizes and morphologies were determined in terms of the following parameters:

- Equivalent diameter (ECD), where the equivalence refers to the area of the particle. The ECD is the diameter of a circle that has an area equal to the area of the particle (Figure 2.2.2 a)).
- Minimum diameter (D_{min}) and maximum diameter (D_{max}) of a particle for angles in the range 0° through 179° with step width 1° (Figure 2.2.2 b) and c) respectively).
- Aspect ratio (AR) or the maximum ratio of width and height of a bounding rectangle of the particle (Figure 2.2.2 d)).
- Sphericity (ψ) described as the 'roundness' of the particle by using central moments (Figure 2.2.2 e)).

- Shape factor (SF), also provides information about the "roundness" of the particle and for a spherical particle the shape factor is 1, while for all other particles it is smaller than 1 (Figure 2.2.2 f)).

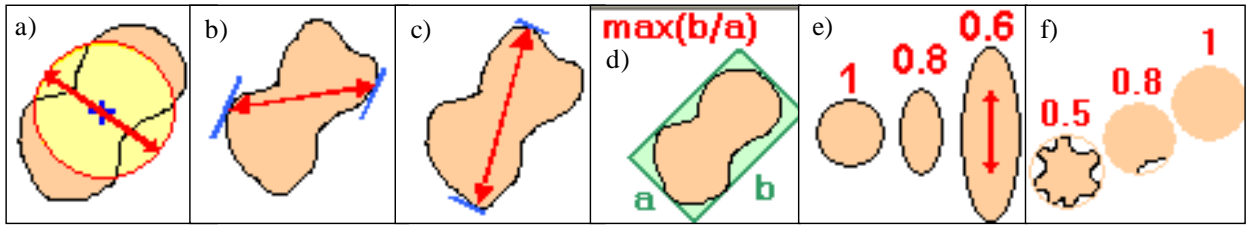


Figure 2.2.2 Studied parameters by means of image analysis: a) equivalent diameter (ECD); b) minimum diameter (D_{min}); c) maximum diameter (D_{max}); d) aspect ratio (AR); e) sphericity (ψ); f) shape factor (SP)

Besides the parameters listed above, an estimation of the average carbide percentage, ACP , was calculated for each material by means of the ratio between the area occupied by carbides, $A_{Carbides}$, and the total area, A_{Total} , for each of the 15 images, i , as shown in Equation 2.2.1.

$$ACP = \frac{A_{Carbides}}{A_{Total}} \cdot 100 = \frac{\sum_{i=1}^{15} A_{Carbides}^i}{\sum_{i=1}^{15} A_{Total}^i} \quad (2.2.1)$$

As only primary carbides were aimed at being studied in this way, carbides with an ECD smaller than 5 μm were discarded in 1.2379, UNIVERSAL and K360. The reason for this was that in these steels and at the number of magnifications in which the images were taken, it was not possible to ascertain with accuracy the sizes of the smallest carbides.

The chemical composition and structure of the primary carbides was determined using EDX, with a maximum spot size of about 1 μm , an acquisition time of 10 s and a beam voltage of 10 kV. These parameters were set to ensure small removal of material during detection period and thus, good accuracy in contents of lightweight elements such as carbon. The results of 1.2379, UNIVERSAL and HWS were contrasted with available information in previous works of Fundació CTM Centre Tecnològic (from now on CTM) and ROVALMA, where the structure of primary and secondary carbides was analysed using EBSD (Electron Back Scatter Diffraction) and TEM (Transmission Electron Microscopy). An in depth analysis of carbides in K360 was performed using EDS and WDS at the Institut Jean Lamour UMR CNRS 7198 in Nancy (France), at the hands of Prof. Jean Steinmetz.

2.3 Mechanical properties

2.3.1 Fracture strength, σ^R , and fatigue limit, $\Delta\sigma^{fat}$

Fracture strength, σ^R , and fatigue limit, $\Delta\sigma^{fat}$, were evaluated by means of three point bending tests with a constant span length of 40 mm (Figure 2.3.1 a)) under monotonic and cyclic load conditions respectively. Samples dimensions were 5 mm x 4 mm x 50 mm. The influence of the carbide orientation on σ^R and $\Delta\sigma^{fat}$ was studied using different sample configurations (D1, D2 and D3) as previously showed in Figure 2.2.1. Samples were mechanically ground and their corners were rounded to avoid stress magnifications and to remove any defect introduced during sample preparation. Faces subject to tensile stress during three point bending tests were carefully polished to mirror-like using colloidal silica particles with approximately 40 nm sizes.

σ^R was evaluated in a universal testing machine using an articulated fixture to minimize torsion effects and with a load rate of 100 N/s (Figure 2.3.1 b)). For each type of steel and carbide configuration 10 to 15 samples were tested and Weibull statistics was applied to take into account the wide scattering of fracture results originated by the heterogeneous distribution of primary carbides.

Fatigue tests were conducted in a resonance testing machine at a load ratio, R , of 0,1 (Figure 2.3.1 c)) at room temperature. Fatigue limit, $\Delta\sigma^{fat}$, was determined at $2 \cdot 10^6$ cycles using the staircase method [WEI61]. In the staircase procedure the first test was started at a stress level which was equal to an estimated mean value of the fatigue strength. If failure occurred prior to the preassigned cycle life, the next specimen was tested at a lower stress level; if the specimen did not fail within the preassigned number of cycles, the next test was run at a higher stress level. The intervals between the stress levels were approximately equal to the standard deviation of σ^R . The test continued in this way, the stress level of each succeeding test being raised or lowered depending on the preceding result. This procedure resulted in the testing being concentrated mainly on three stress levels, centred on the mean level (Figure 2.3.1 d)). The number of samples ranged between 15 and 20 for each material and sample configuration (D1, D2 and D3) and $\Delta\sigma^{fat}$ was then statistically calculated.

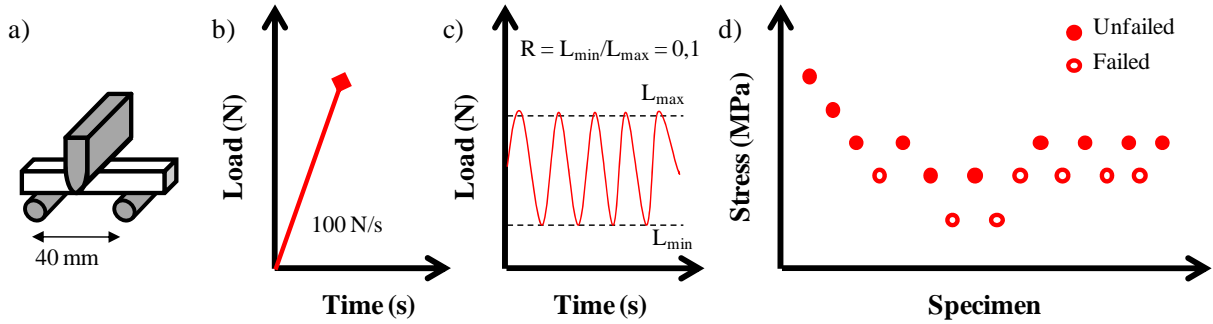


Figure 2.3.1 a) Schema of the three point bending test with a constant span length of 40 mm; b) testing under monotonic load to determine σ^R ; c) testing under cyclic load and d) schema of the staircase method applied to calculate $\Delta\sigma^{fat}$

Fractographic analysis of fracture and fatigue failed specimens was performed using FE-SEM and Confocal Microscopy (CM).

2.3.2 Fracture toughness, K_{IC} , and fatigue crack propagation threshold, ΔK_{TH}

Fracture toughness, K_{IC} , and fatigue crack propagation threshold, ΔK_{TH} , were determined according to the standard test method for measurement of plane strain fracture toughness of metallic materials (E 399-90) and the standard test method for measurement of fatigue crack growth rates (E 647-00). Three point bending tests with a constant span length of 40 mm were performed using prismatic pre-notched specimens, as schematised in Figure 2.3.2 a). Sample dimensions were 15 mm x 7,5 mm x 60 mm. Notches were machined in the face subject to tensile stress and their length and tip radius were 4,5 mm and 0,06 mm respectively. The influence of the carbides orientation in K_{IC} and ΔK_{TH} was studied using different sample configurations (D1, D2 and D3) as previously showed in Figure 2.1.1.

Fatigue precracking was conducted in a resonance testing machine at room temperature using an R of 0,1 (Figure 2.3.2 b)). Once a crack was nucleated, fatigue crack propagation was performed as described in the standard method E 647-00. ΔK_{TH} was defined as the ΔK value at which the crack growth rate, da/dN , was lower than 10^{-12} m/cycle. The fitting parameters of the Paris equation (Equation 1.3.1), A and m , were also determined. Once the fatigue precrack was present in specimens, they were brought to fracture (as shown in Figure 2.3.2 c)) and K_{IC} was calculated as specified in E 399-90.

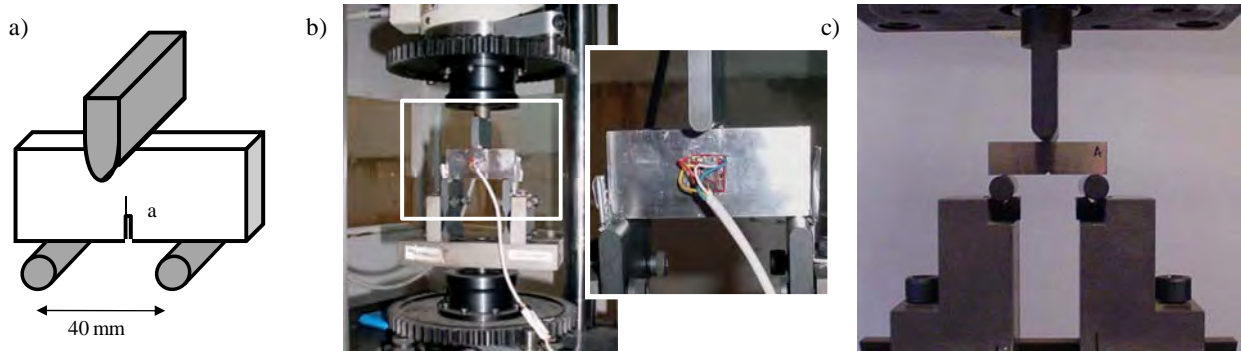


Figure 2.3.2 a) Schema of the three points bending test with a constant span length of 40 mm and using prismatic pre-notched specimens; b) fatigue pre-cracking in the resonance testing machine, crack propagation was monitored by means of strain gauges; c) fracture of the precracked specimens

2.4 Study of crack nucleation and growth in tool steels

2.4.1 Micro-mechanical properties of the primary carbides and the metallic matrix

Micro-mechanical properties, i.e. Young's modulus, E , hardness, H , and fracture toughness, K_C , of the primary carbides embedded in 1.2379, UNIVERSAL and K360 steels were determined by means of instrumented nanoindentation. E and H of the metallic matrix were determined using this technique as well. In HWS the size of primary carbides and the matrix ligaments in-between them were too small to be indented without influence of neighbouring phases. Hence the micro-mechanical properties of this steel could not be determined.

(Note: the term K_C is used here to refer to the fracture toughness of primary carbides instead of K_{IC} , to distinguish it from mode I plane strain toughness).

In the present work, the micro-mechanical properties of primary carbides and metallic matrix were helpful as driver to understand and rationalize the behaviour and damaging mechanisms of tool steels. However, the investigation on nanoindentation belongs to the background of CTM on micro-mechanical characterisation of hard phases and, particularly to the work of Núria Cuadrado within the frame of her Doctoral Thesis (in course). The reader is pleased to refer to the publications of Oliver and Pharr [OLI92 and OLI04], Casellas et al. [CAS07] and Cuadrado et al. [CUA12] for a detailed description of E , H and K_C measurement techniques.

2.4.2 Crack nucleation and growth under monotonic loading

Mechanisms of crack nucleation and growth under monotonic loading were evaluated using the same test set-up and samples as for evaluate σ^R . The three ingot cast steels were analysed both under D2 and D3

configurations, while only HWS D2 was studied since PM steels typically show a rather isotropic behaviour compared to ingot cast steels.

Samples faces subject to tensile stress during three point bending tests were carefully polished to mirror-like conditions. In case of 1.2379, UNIVERSAL and HWS the final finish of colloidal silica particles was applied. In K360 it hardly allowed distinguishing between carbides of different compositions and metallic matrix. Therefore, an electrolytic etching consisting in a 1 % CrO_3 solution at 3 V dc during 10 s was applied on the surface. This type of etching was prepared as specified by Van der Voort et al. [VAN04], since the work of these authors shows that it is possible to identify carbides with different chemical compositions and structures (namely MC, M_7C_3 , M_6C , M_{23}C_6 , M_3C and M_2C) by attacking, colouring, outlining or simply not reacting with them when certain selective etchants are employed.

Stepwise loading was conducted by increments of 10 to 15 % of σ^R of each material. Inspection of the tensile face followed the application of each load step in order to detect damage in the microstructure, as schematised in Figure 2.4.1 a). In this way the threshold stresses corresponding to the fracture of primary carbides, growth of cracks, coalescence of these through the matrix, etc., were determined. Observations of the surface were made using LOM, CM and FE-SEM and as shown in Figure 2.4.1 b), they were focused on a narrow zone at the centre of the sample where the stresses were the highest during the three point bending test. The applied stress level from which primary carbides were found to start breaking was assumed as the fracture resistance of primary carbides, σ^{RC} .

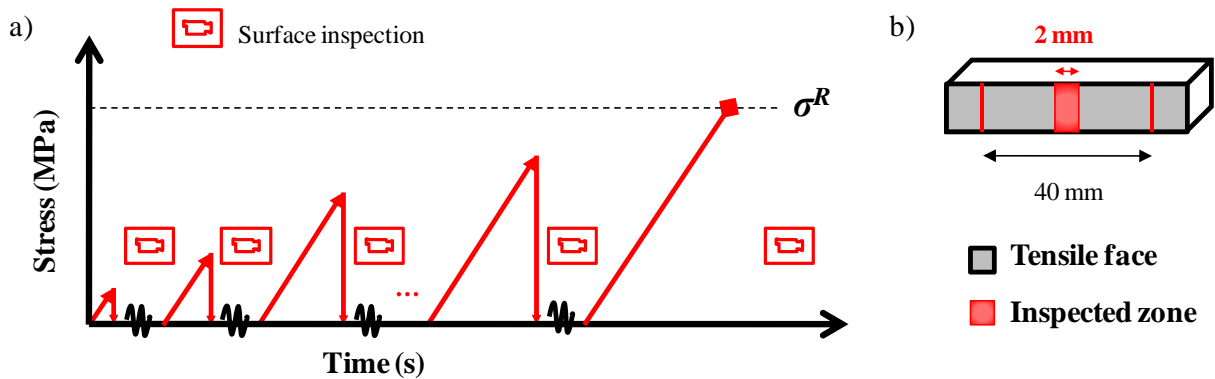


Figure 2.4.1 a) Stepwise monotonic tests and surface inspections; b) schema of the inspected zone in the tensile face of samples

2.4.3 Monitoring micro-damage using Acoustic Emission techniques

The procedure described above these lines presented some limitations to accurately determine the threshold stresses at which damaging mechanisms took place. One of these restrictions consisted in the fact that damage could be detected only at the surface, as the interior of samples could not be checked. In addition, threshold stresses for damaging mechanisms could only be determined in-between stress

intervals, i.e. between an applied stress increment and the following one. And last but not least, a detailed inspection of the microstructure after each loading-unloading step was rather dependent on the skills of the investigator to find damaged zones using the magnifications available with LOM or CM.

To tackle with these limitations, micro-damage accumulation and quantitative detection of individual microcracks were monitored using Acoustic Emission (AE) source characterization. Using this technique, AE signals could be coupled to the acting applied stresses at which they were registered and hereby, damage thresholds could be determined in situ with accrued accuracy. This work was carried out in cooperation with the Laboratori d'Enginyeria Acústica i Mecànica (LEAM) of the Universitat Politècnica de Catalunya (UPC), within the frame of the Doctoral Thesis of Eva Martínez-González (in course).

In this way, three point bending tests were coupled to AE sensors and an analyser to detect and record, and posteriorly investigate, the signals obtained. Signal filtering was carried out to remove noise, friction and other emitting phenomena not related to the micro-mechanisms occurring in the material during the test. A constant span length of 40 mm was used and the samples dimensions were 8 mm x 6 mm x 120 mm. These dimensions were especially chosen taking into account the reasons listed below:

- In order to ensure the transmission of AE signals from the sample to the sensors through the surface, the sample had to be wider than the sensors diameter to well allocate them as schematized in Figure 2.4.2;
- The sample had to be much longer than the span length since proper signal filtering required the distribution of more than one sensor, as shown in Figure 2.4.2. The signals which were first received at sensors number 1 and 2 were rejected while only those initially acquired at sensor 3 were considered as relevant for micro-damage evaluation. The reason for this was that sensor 3 was placed directly on the most stresses area. The presence of three sensors also permitted to localise the signals with respect to the centre of the sample by means of a linear localisation process. Finally, the length of the sample helped reducing wave rebounding at walls and attenuating friction signals as well.

D2 samples of 1.2379, UNIVERSAL and HWS were analysed by these means. Sample preparation was carried out as explained in section 2.4.1. This time tests were performed under control of displacement with a rate of 0,01 mm/min. The tests monitored by means of AE were interrupted before unstable failure to avoid damaging the sensors and recalibrating them. Due to the suddenness of fracture, some tests could not be stopped and in these cases, sensors were discarded for other tests.

The AE system consisted of three AE sensors, three pre-amplifiers and one acquisition device with a computer as it is shown in Figure 2.4.2. Sensor 3 acquired the specimens AE signals, while sensors 1 and 2 were employed to detect the background noise. Small resonant piezoelectric sensors were used, type

VS700-D from Vallen System GmbH, with the centre frequency at around 700 kHz and two peak response frequencies at 300 and 675 kHz approximately. Three AEP4 pre-amplifiers with a fixed gain of 34 dB (Vallen System GmbH) were used as well. In order to avoid magnetic and mechanical noise, digital filters of 95-850 kHz were applied in each channel. The threshold level was set to 34 dB, a higher value than the previously measured background level.

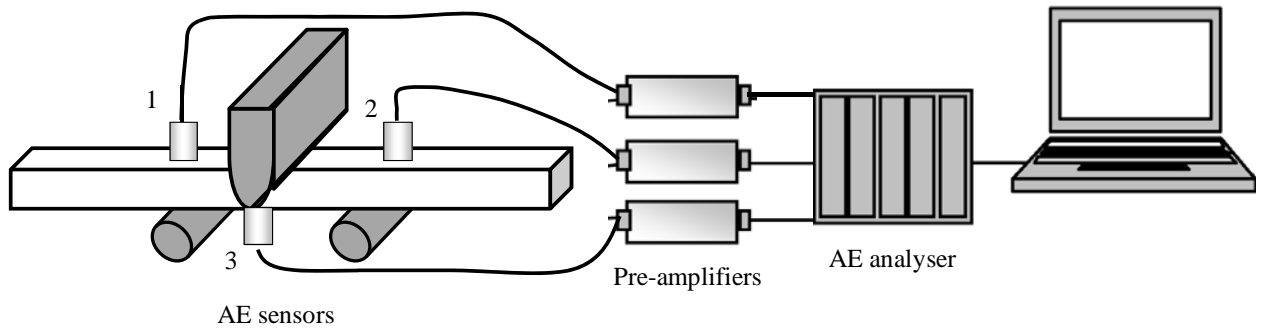


Figure 2.4.2 Experimental set-up for the AE monitored bending tests

Due to small specimens dimensions very short signal acquisition times were chosen in order to avoid capturing noise produced by wave rebounding. Furthermore, only the very initial part of every signal was considered as purely representative of micro-damage phenomena. Thus, analysis and post-processing of acquired signals was exclusively carried out for this frame times.

By means of AE monitoring the final fracture of tested samples was anticipated since characteristic signal patterns could be distinguished when failure was about to occur. In this way the crack geometry just before failure could be studied, as it will be explained in section 2.4.5.

2.4.4 Crack nucleation and propagation in cyclic loading conditions

Mechanisms of crack nucleation and propagation under cyclic loading were evaluated using the same test set-up and samples as those employed for evaluating $\Delta\sigma^{fat}$. In a first set of tests, 1.2379 D2 samples were used to determine the fatigue crack propagation threshold of cracks nucleated from broken primary carbides, and compare the values obtained to those determined for long cracks following the procedure E647-00. The applied stress amplitude, $\Delta\sigma$, for these tests was kept at 720 MPa, and the tensile surface of the sample was inspected using CM after 10000, 15000, 20000, 25000, 45000, 245000 and 745000 cycles.

In order to assess the effect of increasing the applied stress on the threshold for crack propagation (and promote the growth of those cracks which remained arrested in broken carbides at 720 MPa) the stress amplitude was increased to 820 MPa and inspections at 3000 and 11000 cycles were carried out. The sample was then brought to $\Delta\sigma = 850$ MPa and its surface was inspected after 3000 and 13000 cycles. At

this point fatigue cracks as long as 200 µm were observed at the surface. With the aim to assess their shape, the sample was broken monotonically to measure the halo of the fatigue precrack.

The acting stress intensity factors of cracks observed at the surface were calculated as follows from Equation 2.4.1:

$$\Delta K = Y\Delta\sigma\sqrt{a} \quad (2.4.1)$$

where a is the depth of the crack beneath the surface (as schematised in Figure 1.2.17) and Y a coefficient depending on the geometry of the crack. As only $2c$, the length of the cracks at the surface, could be measured (see Figure 1.2.17 as well), semi-elliptical geometries with a/c ratios 0,3 - 0,5 and 1 were considered to estimate the shapes of small cracks. Y values were calculated according to Newman and Raju [NEW84] assuming the aforementioned a/c ratios. ΔK values estimated through Equation 2.4.1 were then compared to the ΔK_{TH} determined for long cracks (E 647-00) and the validity of ΔK_{TH} for small cracks was verified if they had certainly propagated or remained arrested.

In a second set of tests the parameters regulating stable crack growth of long cracks, i.e. m and A of the Paris equation were compared to those determined for small propagating cracks nucleated from carbides in fatigue samples. For that, a UNIVERSAL D2 sample was loaded to $\Delta\sigma = 990$ MPa and the lengths of cracks at the surface were measured using CM at increasing number of cycles (up to 27664 when the sample failed). In this way, and assuming an a/c ratio of 1, the Paris curves of “small” cracks was calculated as well as the corresponding A and m parameters.

2.4.5 Subcritical growth of small cracks: assessment of R -curve behaviour

As shown previously in section 1.2.3, Gomes et al. [GOM97] reported on static subcritical crack growth in high speed steels and claimed to introduce the notion of R -curve in tool steels. Hereby, the aim of this part of the investigation is to evaluate the possible R -curve behaviour of 1.2379, K360, UNIVERSAL D2 and D3, as well as HWS D2.

To calculate the R -curve, stepwise monotonic tests were carried out as described in section 2.4.1 and the tensile face of samples was inspected at the end of each step. The length of cracks identified at the surface, $2c$, was measured at each applied stress, σ_a , so that the applied stress intensity factor, K_a , for each crack could be estimated through the expression shown in Equation 2.4.2:

$$K_a = Y\sigma_a\sqrt{a} \quad (2.4.2)$$

a , the depth of the crack beneath the surface was assumed to answer to the ratios of $a/c = 0,3 - 0,5$ and 1 and Y values were calculated according to Newman and Raju [NEW84].

In order to shed light to the real shape of small cracks, stepwise polishing was performed in UNIVERSAL D2 samples in which thanks to AE monitoring, bending tests could be halted some instants before failure. To control the amount of removed material during polishing, Rockwell C imprints were performed close to the studied cracks. By the reduction of the imprint diameters after each polishing step the depth of cracks could be estimated. FE-SEM inspections were performed after each step in order to cope with the changes in crack morphologies.

2.5 Mechanical and tribological behaviour of tools for cold forming and shearing UHSS

2.5.1 Identification of the main failure mechanisms of industrial tools

Tools working in cold forming and shearing operations of UHSS in the industry were analysed at the end of their service life in order to determine their main failure mechanisms. These investigations were carried out in the frame of the research project FORMA0 (2006-2009) which was funded by the Spanish government and led by SEAT S.A. Many tools working with various types of UHSS, sheet thicknesses and different process parameters could be investigated thanks to tests performed at SEAT S.A., AUTOTECH ENGINEERING AIE (Group GESTAMP AUTOMOCIÓN) and TROE S.L.

Both mechanical and tribological aspects affecting tools in mass production lines were taken into account in this investigation. In order to identify and characterise damage in tools, fractographic studies were performed using the SEM available at ROVALMA R&D department, in which an extra-large vacuum chamber allows the analysis of tools up to 50 kg.

2.5.2 Characterization of the damaging processes of tools working in industrial conditions and their evolution with the number of strokes

In this part of the investigation the evolution of damage on selected reference tools working at SEAT S.A., AUTOTECH ENG. and TROE S.L. was studied by carefully supervising the tests, and interrupting them to inspect the tools after certain numbers of strokes. On every stop, tools were analysed using the SEM at ROVALMA. The influence of using different strategies regarding tool materials, hardness, coatings, etc., on the performance of tools was also evaluated, as well as the effects of the surface quality as a result of machining (i.e. roughness, surface defects, scratches, grinding grooves, etc.). The details of the studied tools are described in the following sections 2.5.2.1, 2.5.2.2 and 2.5.2.3 respectively, but the main details of the different tests are summarised in Table 2.5.1.

2. Experimental procedure

Table 2.5.1 Summary of the shearing tests studied in industrial conditions at different companies

Shearing process	Sheet steel	Sheet thickness, mm	Company	Tool steel
Trimming	Press hardened 22MnB5	2	SEAT S.A.	HS6-5-4 (63-64 HRC)
				DIN 1.3202 (62-63 HRC)
				VANADIS 4 EXTRA (62-63 HRC)
				HWS (59-60 HRC)
Punching	MS-W1200	2	AUTOTECH ENG.	HWS (62 HRC)
Drawing & Punching	TRIP800 DP1000	2	TROE S.L.	1.2379A (60-62 HRC)
				1.2379B (58-60 HRC)
				UNI2 (61-62 HRC)
				HWS2 (61-62 HRC)

2.5.2.1 Trimming of press hardened boron steel 2 mm thick (at SEAT S.A.)

Two PM high speed steels: HS6-5-4 (AISI M4) and DIN 1.3202 (AISI T15), and two PM cold work steels: VANADIS 4 EXTRA and HWS were employed to trim press hardened boron steel at SEAT S.A. The chemical composition of the aforementioned tool steels is shown in Table 2.5.2 (for HWS refer to Table 2.1.1).

Table 2.5.2 Chemical composition of the tool materials (in wt %)

Steel	C	Cr	Mo	V	W	Co	Mn	Si
HS6-5-4	1,30	4,25	4,75	4,10	5,40	-	-	-
DIN 1.3202	1,60	4,00	-	5,00	12,25	5,00	-	-
VANADIS 4 EXTRA	1,40	4,70	3,50	3,70	-	-	0,40	0,40

In order to analyse the influence of hardness on the behaviour of tools, heat treatments were applied as described in Table 2.5.3 to obtain hardness levels ranging from 59 to 64 HRC. Trimming was performed in remnant flanges of press hardened 22MnB5 steel B-pillars (see Figure 2.5.1). The sheet was 2 mm thick and coated with an Al-Si layer of about 30-50 μm thick to prevent surface oxidation during austenitizing.

Table 2.5.3 Heat treatment applied to the studied materials and obtained hardness

Steel	Austenitizing (quench in oil)	Tempering	HRC
HS6-5-4	1160 °C for 30 min	520 °C for 1 h (x3)	63 - 64
DIN 1.3202	1180 °C for 30 min	595 °C for 2 h (x3)	62 - 63
VANADIS4	1100 °C for 30 min	549 °C for 2 h (x2)	62 - 63
HWS	1060 °C for 30 min	540 °C for 2 h (x2); 560 °C for 2h	59 - 60



Figure 2.5.1 Geometry of the remnant B-pillar flanges used for trimming at SEAT S.A. (the arrow shows the location of the trimming in the sample)

The studied tools consisted in two moving blades (A and B in Figure 2.5.2) and a stationary blade (C in Figure 2.5.2). The cutting edge of punches and die was rounded to 100 - 200 μm and trimming was performed using two different clearances: 5 and 10 % of the sheet thickness. Each set of tools build from the four different tool steels carried out a total number of 10000 strokes with no lubrication.

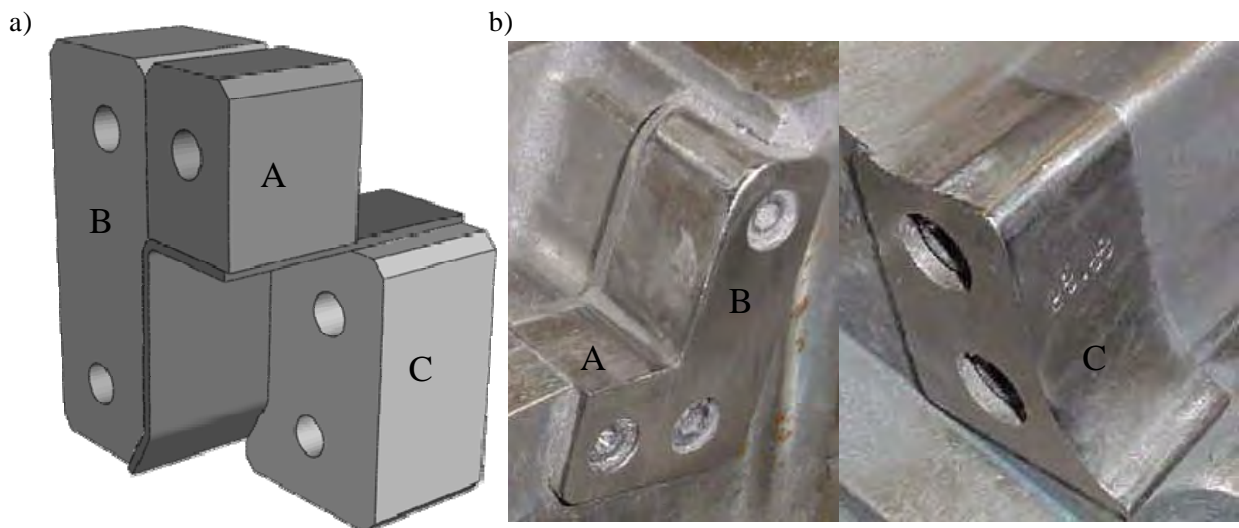


Figure 2.5.2 a) Schema of the trimming process; b) real tools in the press; moving blades A and B, and stationary blade C

Tool wear was assessed by means of the loss of material at the cutting edge, as shown in Figure 2.5.3. Several profiles were measured at different locations of the tool edge by contact profilometry using a spherical tip of 0,5 mm diameter. At each location, three to five different profiles were measured in order to calculate an averaged value of lost material. This analysis was performed in HS6-5-4 and HWS tools since they showed the highest and the lowest hardness values amongst the studied tools (64 and 60 HRC respectively). The profiles were taken at the initial stage, and after 2500 and 5000 strokes.

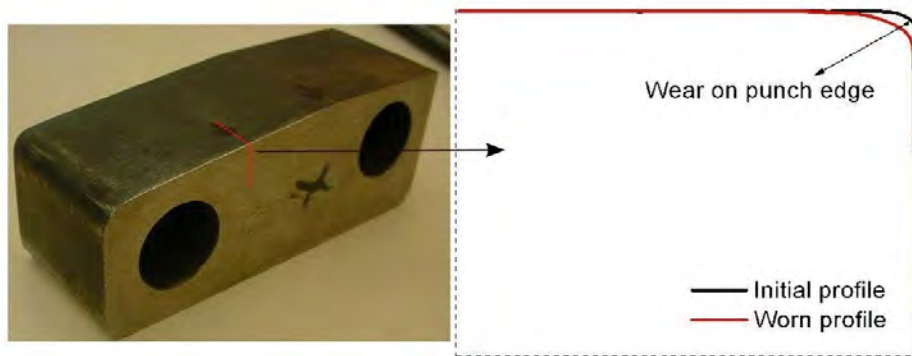


Figure 2.5.3 Profiles at the cutting edge and the estimation of wear

The procedure to estimate the worn area from cutting edge profiles included the following actions:

a) Translation

All the measured profiles were translated so that they coincided within the considered X - Y coordinate system. Translation was performed with respect to a reference zone, which was selected for each profile far from the cutting edge (at a distance of 3 mm). The reference zone permitted to compare the profiles obtained at different numbers of strokes and it was assumed to be not affected by wear. This action was crucial to obtain accurate results since the measure of the worn areas was extremely sensitive to the adjustment of the profiles. Vertical and/or horizontal translations were carried out as shown in Figure 2.5.4.

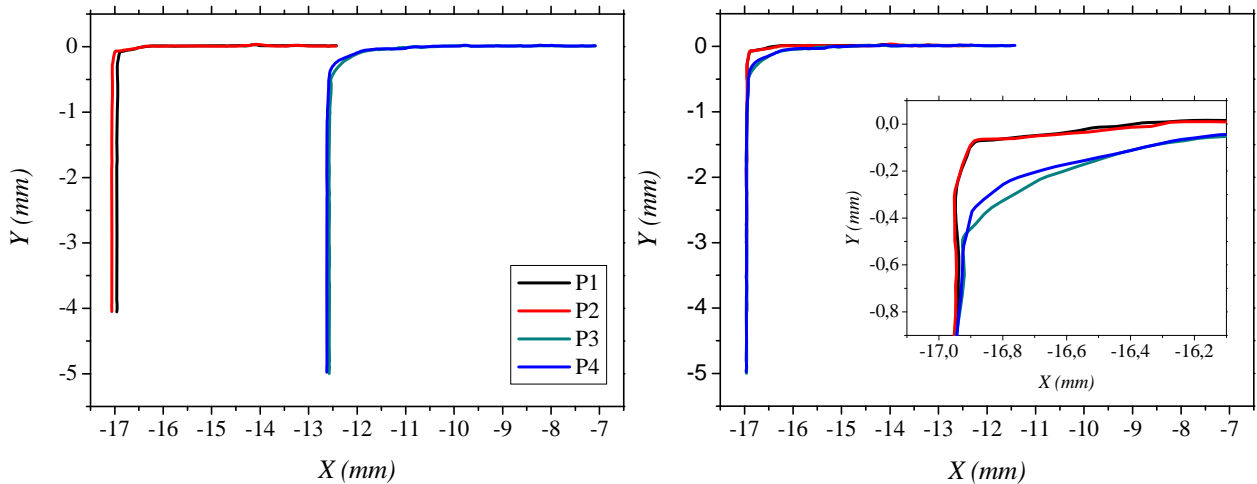


Figure 2.5.4 Translation of P2, P3 and P4 to P1 in the X - Y coordinate system

b) Rotation

A rotation of 45° from their original configuration was applied to the profiles to accurately calculate their areas by integration. It was performed by transforming the profile data from Cartesian (X , Y) to Polar (r ,

θ) coordinate system. The new coordinates $(r, \theta + \pi/4)$ were transformed to Cartesian once again for an easier interpretation of the results (see Figure 2.5.5).

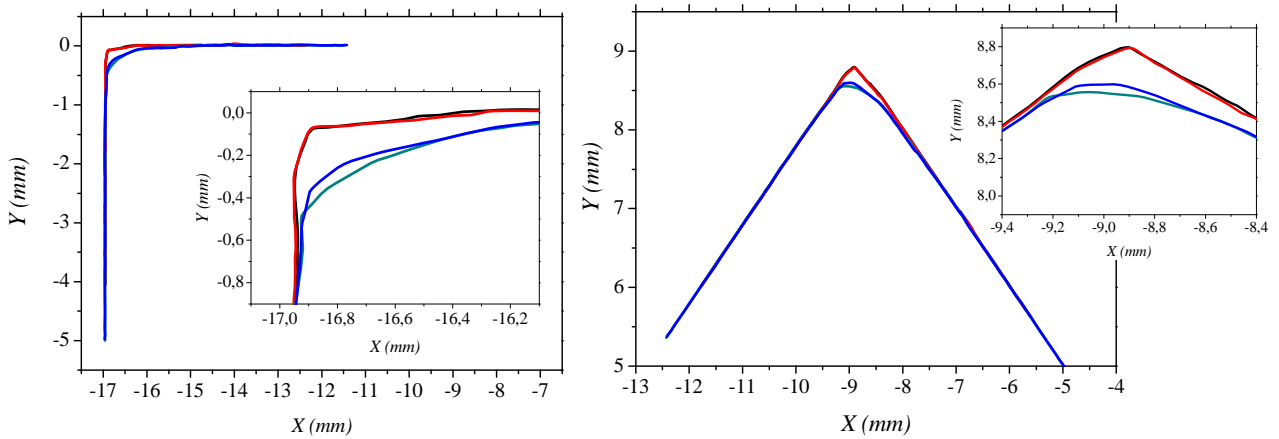


Figure 2.5.5 P1, P2, P3 and P4 rotation

c) Binarization

Numerical calculations were performed to convert each profile plot image to a binary system in black and white. The objective of the binarization was obtaining a mathematic function for each profile. To proceed, each profile was plotted separately and the area was filled in black colour, as shown in Figure 2.5.6. A reference scale window $[(X_{min}, Y_{min}), (X_{max}, Y_{max})]$ was selected and it was employed for all the profiles of a same location. The reference scale window was chosen following the criteria listed below:

- Y_{max} was the maximum Y -value amongst the profiles under consideration.
- The X coordinate corresponding to Y_{max} , named as X_c for its position at the centre of the profiles, determined X_{min} and X_{max} in the following way: $X_{min} = X_c - 0,5$ and $X_{max} = X_c + 0,5$.
- Y_{min} was defined as $Y_{max} - 1$.

The reference scale window was different from one tool to another or from one tool position to another, since it depended on the X, Y coordinates of the measured profiles. However, this deviation was homogenised when binarizing the profile to gray scale (0-255). Thus, it was only imperative that the selected reference scale window had always the same area (e.g. 1 mm^2), and that profiles from the same position measured after different numbers of strokes were plotted using this one, as shown in Figure 2.5.6. The images were saved as .BMP files and their resolution was set to 600 dpi.

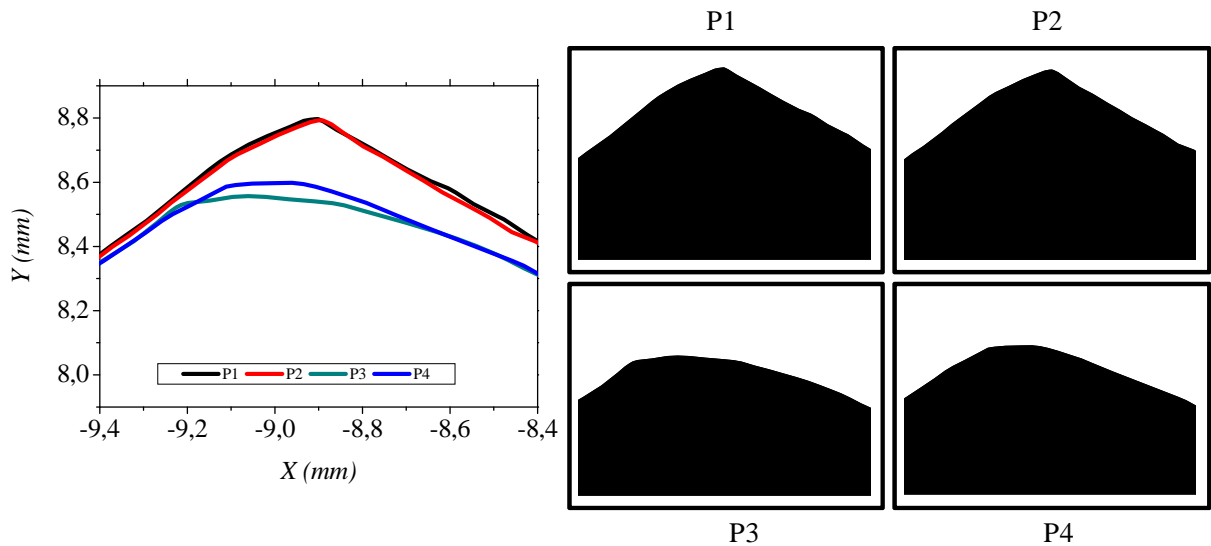


Figure 2.5.6 P1, P2, P3 and P4 in the reference scale window and plotted separately in black and white

For profile plot binarization the software *IMAGEJ* was employed. *IMAGEJ* can be downloaded for free and it converts original black and white images to gray scale versus pixels profiles, as shown in Figure 2.5.7. As the software sets 0 automatically to black and 255 to white, the profile was always inverted.

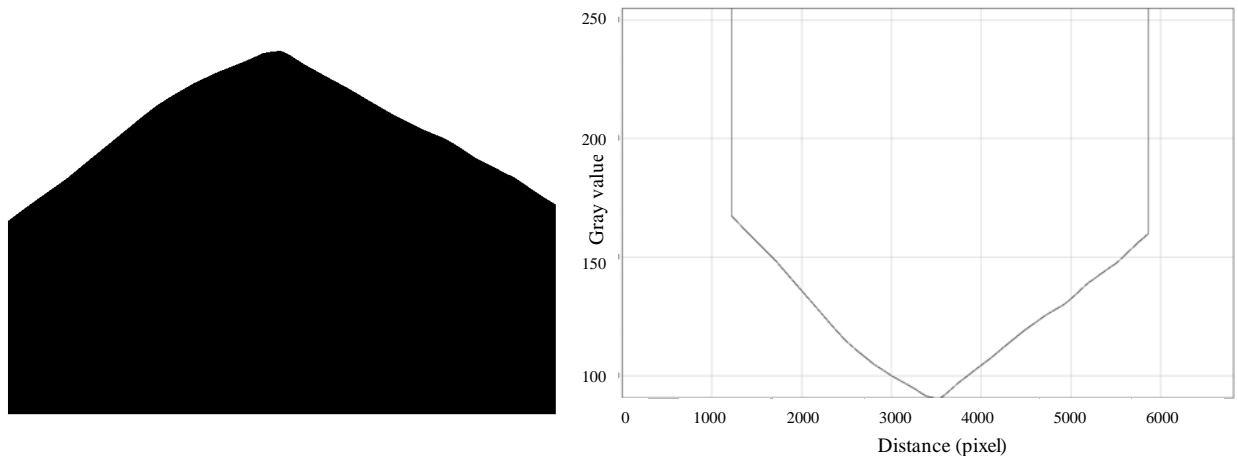


Figure 2.5.7 P1 profile in gray scale vs pixels obtained with *IMAGEJ*

Profile data were stored as .TXT files and these were later exploited in excel. A line of known length was drawn in an empty reference scale window image, so that pixels could be converted to microns. By measuring the height of the image in pixels, gray scale values were transformed into pixels and these could be converted to microns as well, as explained before. At the end of this procedure, all the profiles were rescaled in the same way (see Figure 2.5.8 a)) and thus, they were ready to be compared.

d) Estimation of wear

Wear estimation was performed by measuring the area under each profile (integrating each profile), and comparing the values obtained to determine the amount of worn material when increasing the number of strokes (Figure 2.5.8 b)).

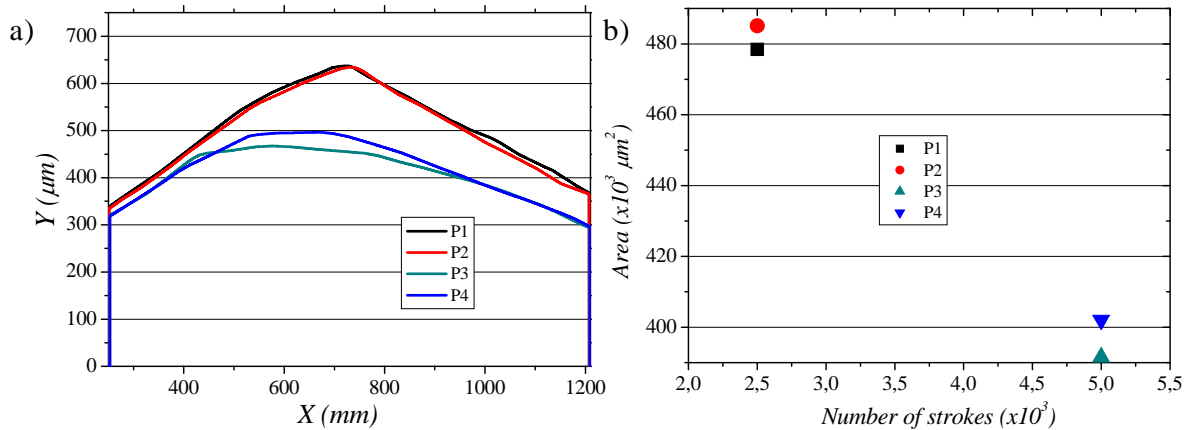


Figure 2.5.8 a) P1, P2, P3 and P4 rescaled in microns after treatment with IMAGEJ; b) calculated areas in correlation with the respective number of strokes

2.5.2.2 Punching of MS-W1200 2 mm thick (at AUTOTECH ENG.)

Punching of MS-W1200 bumpers 2 mm thick was carried out at one of the centres of GESTAMP AUTOMOCIÓN in Spain, by AUTOTECH ENG., and it was studied in this Thesis using different sets of HWS punches and dies heat treated at 62 HRC. Table 2.5.4 shows the mechanical properties of the MS-W1200 sheet.

Table 2.5.4 Mechanical properties of MS-W1200 determined by means of tensile tests

Steel	Thickness (mm)	σ_y (MPa)	σ^R (MPa)	Elongation (%)	n (Hollomon's coefficient)
MS-W1200	2	1110	1226	5,4	0,10

The punching operation is schematically described in Figure 2.5.9 a). There were totally four different sets of HWS punches and dies: the first three worked to 15000, 40000 and 100000 strokes respectively in order to assess the damage evolution at different stages of their lives, while the fourth was coated with CrN-AlCrN to evaluate the effect of the coating on the tool performance. The clearance was 10 % of the sheet thickness and the cutting edge radius of the punch was rounded up to 100 μm. A picture of one of the sets of tools is illustrated in Figure 2.5.9 b).

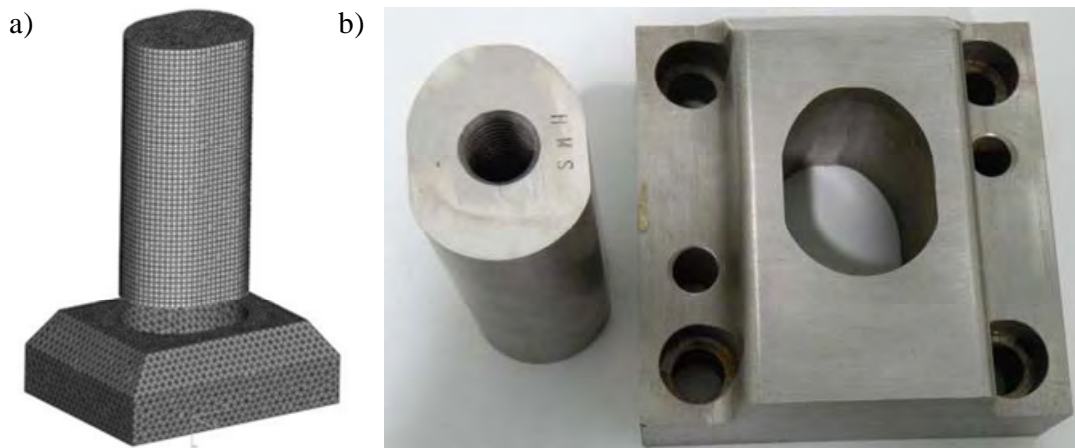


Figure 2.5.9 a) Schematic description of the punching operation; b) picture of one of the sets of tools employed

Fractographic inspection of the surface was performed using SEM. Metallographic analysis of the punches beneath the surface and the coating was carried out as well. Several transverse specimens were extracted from the cutting edge as described in Figure 2.5.10. Six different zones were selected at the cutting edge (Figure 2.5.10 a)) and then specimens were removed by means of EDM (Electro Discharge Machining). Figures 2.5.10 b) and 2.5.10 c) show respectively the punch and the specimen. One of the two transverse faces of the punch (red face in Figure 2.5.10 a)) was mechanically ground and mirror-like polished using colloidal silica. Some of the specimens were etched in order to reveal the martensite and the grain boundaries in the steel. In Figure 2.5.10 d) an image of the microstructure just below the surface of the cutting edge area can be observed.

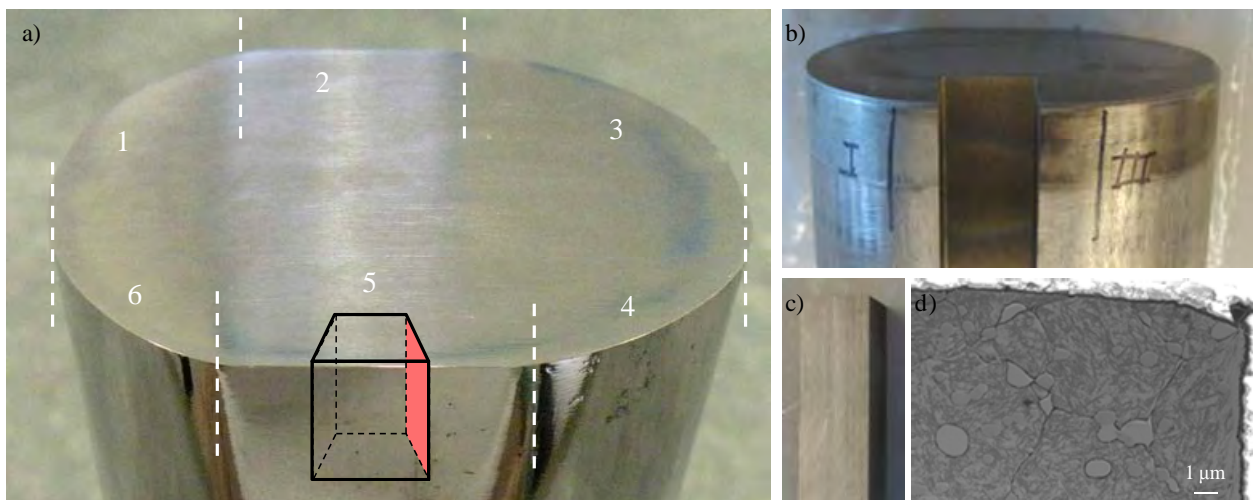


Figure 2.5.10 a) Identification of six different zones along the punches cutting edge, in red the polished face of each specimen; b) punch after the extraction of the specimen; c) extracted specimen and d) image of the microstructure below the cutting edge obtained after polishing the cross sectional face shown in a)

2.5.2.3 “Matriu de Dany Accelerat (MDA)”: forming and punching TRIP800 and DP1000, both 2 mm thick (at TROE S.L.)

The MDA was especially designed and built by the members of the FORMA0 consortium to reproduce several forming and shearing operations and at the same time, accelerate the damaging mechanisms of tools (saving time and material costs). These tests were carried out at TROE S.L., but the die was fully on duty for research purposes. Hereby, any modification regarding the operating process was performed regardless of the quality of the obtained piece and any other limiting factor of mass production manufacturing.



Figure 2.5.11 MDA in TROE S.L.

The die was designed in different modules, as schematized in Figure 2.5.12, and many spare tools were built using 1.2379, UNIVERSAL and HWS, as detailed in Figure 2.5.13. Heat treatments applied to the punches are described in Table 2.5.5. A total number of 9 operations were carried out at the same time, but the focus was paid on the drawing process at step number 4, bending at number 6, and punching at 5, 8 and 9.

2. Experimental procedure

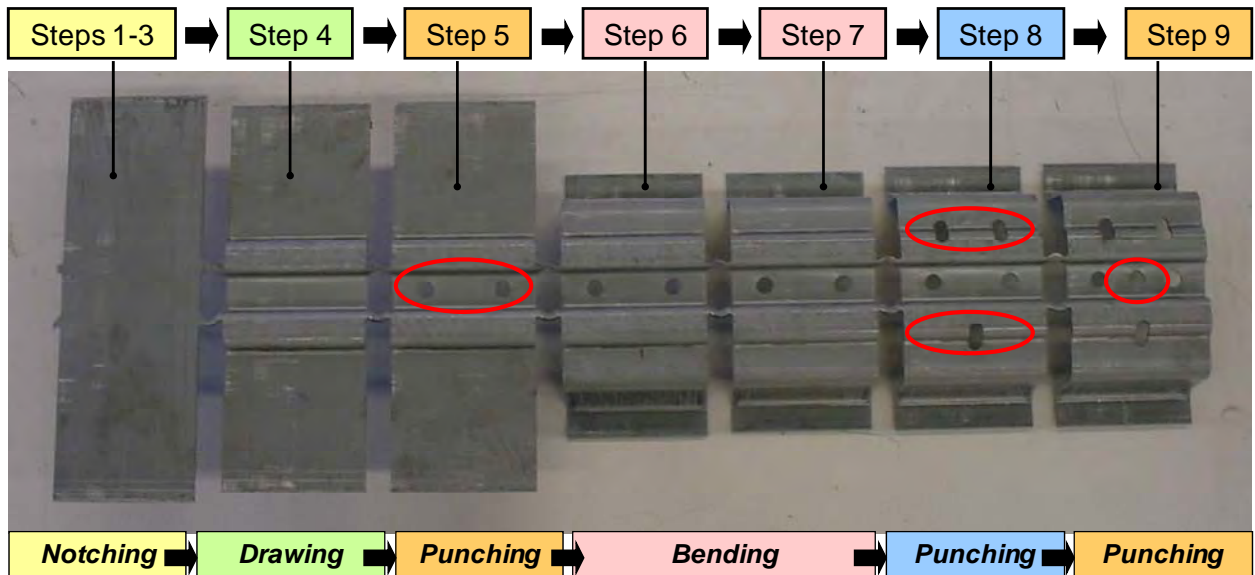


Figure 2.5.12 Description of the forming and shearing process studied in the MDA

STEP	TYPE OF TOOL	NAME	A	B	U	H
			1,2379A	1,2379B	UNIVERSAL	HWS
			60-62HRC	58-60 HRC	61-62HRC	61-62HRC
4	PUNCH	238	238A			238H
	DIE	240	240A			240H
5	PUNCH	917	917A (x7)	917B (x4)	917U (x4)	917H (x8)
	DIE	908	908A (x4)	908B (x4)	908U (x4)	908H (x4)
6	PUNCH	250	250A		250U	
	DIE	253	253A		253U	
8	PUNCH	922	922A (x13)	922B (x6)	922U (x6)	922H (x12)
	DIE	923	923A (x6)	923B (x6)	923U (x6)	923H (x6)
9	PUNCH	917	917A (x6)	917B (x2)	917U (x2)	917H (x4)
	DIE	908	908A (x2)	908B (x2)	908U (x2)	908H (x2)

Figure 2.5.13 Spare tools used in the MDA; step, type, material, hardness and designation of each tool

Table 2.5.5 Heat treatment applied to the punches and attained hardness level

Steel	Austenitizing (quench in oil)	Tempering	HRC
1.2379A	1050 °C for 30 min	530 °C for 2 h (x2)	60 - 62
1.2379B	1050 °C for 30 min	400 °C for 2 h (x2)	58 - 60
UNI	1070 °C for 40 min	540 °C for 2 h (x2); 560 °C 2h	61 - 62
HWS	1060 °C for 30 min	540 °C for 2 h (x2); 560 °C 2h	61 - 62

A total number of 15000 strokes were carried out using TRIP800 2 mm thick, as well as 16000 strokes with DP1000 2 mm thick. However, the tests were stopped at each series of 2000 strokes, so that all materials could be evaluated and damage evolution could be assessed by inspecting the tools. The

clearance for punching was 5 % of the sheet thickness in case of TRIP800, and 10 % for DP1000. Mechanical properties of TRIP800 and DP1000 sheets are scheduled in Table 2.5.6.

Table 2.5.6 Mechanical properties of TRIP800 and DP1000 determined by means of tensile tests

Steel	Thickness (mm)	σ_y (MPa)	σ^R (MPa)	Elongation (%)	n (Hollomon's coefficient)
TRIP800	2	545	835	32,0	0,22
DP1000	2	785	1045	11,6	0,13

Damage evaluation in tools of the MDA consisted in wear analysis of drawing and bending tools as well as fractographic studies of punches using SEM. Wear characterisation was performed by measuring the edge profiles using contact profilometry at different numbers of strokes (Figures 2.5.14 a) and b)), and comparing the radii values as shown in Figure 2.5.14 c).



2.5.14 a) - b) Profile measurement at the tool edge; c) schema of the estimation of material lost by wear (tool radius variation)

2.5.3 Conception, design and construction of a die for laboratory benchmark and tests reproducing the failure mechanisms of industrial tools

As an approach to study the damaging mechanisms of tools for forming and shearing UHSS in laboratory conditions, a die called “Herramienta de Punzonado Continuo (HPC)” was conceived, designed and built for bench testing at CTM. The aim of the HPC was to reproduce the working conditions of industrial tools but under laboratory control and supervision of the investigators. With respect to the tests at the industry, the HPC permitted to easily remove the tools whenever it was necessary with no interferences with the production plan.

2. Experimental procedure

The HPC (Figure 2.5.15 a)) was conceived so that the maximum number of strokes could be performed employing the minimum quantity of sheet material. DP1000 2 mm thick was used (the same as the employed for tests with the MDA) (as shows Figure 2.5.15 b)). Both punching and slitting operations were performed at the HPC, as it can be observed in Figure 2.5.15 c).

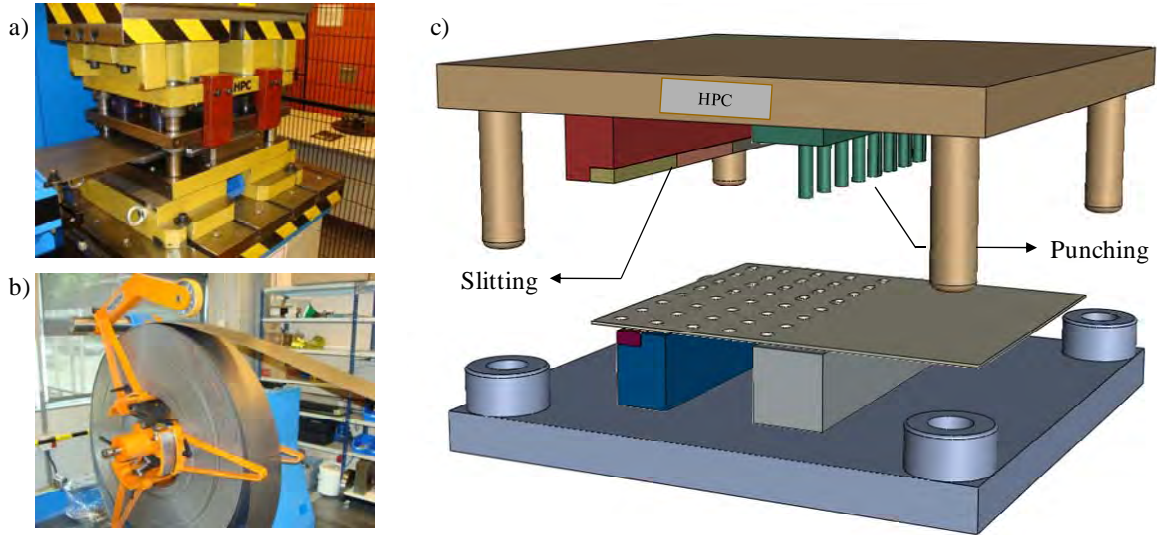


Figure 2.5.15 a) HPC; b) coil of DP1000 2 mm thick used in these tests; c) schematic description of the shearing processes studied in the HPC (punching and slitting)

The same punches used in the MDA were tested in the HPC, as it can be observed in Figure 2.5.16 a). However in the HPC, K360 punches were included to the study. Details on the heat treatment parameters of 1.2379, UNIVERSAL and HWS punches can be found in Table 2.5.5. Heat treatment of K360 punches consisted in the following procedure: austenitizing (quenching in oil) at 1070 °C for 40 min, and two tempering at 530 °C for two hours. The final hardness was 61 – 62 HRC.

The slitting tools (Figure 2.5.16 b)) were built using 1.2379, UNIVERSAL and HWS at 60 HRC as described in Table 2.5.7.

Table 2.5.7 Heat treatment applied to the studied materials and obtained hardness

Steel	Austenitizing (quench in oil)	Tempering	HRC
1.2379	1050 °C for 35 min	525 °C for 1 h (x2)	59 - 60
UNIVERSAL	1070 °C for 40 min	520 °C for 2 h (x3)	60 - 61
HWS	1020 °C for 40 min	520 °C for 2 h (x3)	60 - 61

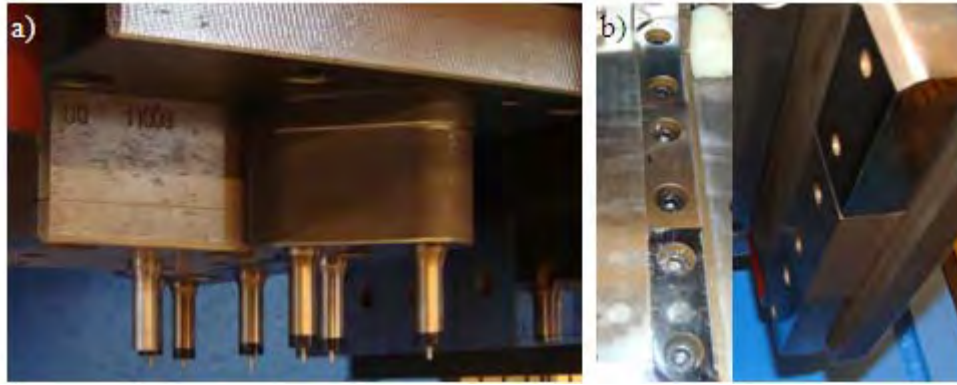


Figure 2.5.16 a) Punches of the HPC; b) slitting tools of the HPC

A total amount of 36000 strokes was performed in the HPC. Different clearances as well as tool radii were employed both in punching and slitting processes in order to evaluate their effects on the mechanical response of tools. Several PVD-coated punches were also tested in the HPC as scheduled in Table 2.5.8, AlTiN and W:C-H coatings were employed. Punches were coated by AIN (Asociación de la Industria Navarra) within the frame of the research project FORMA0.

Table 2.5.8 Name, material, coating type and total number of strokes of the coated punches used in the HPC

Name	Material	Coating	Total number of strokes
917U(3)	UNIVERSAL	W:C-H	12000
917U(5)	UNIVERSAL	W:C-H	1500
917U(7)	UNIVERSAL	AlTiN	5000
917H(3)	HWS	AlTiN	12000
917H(4)	HWS	W:C-H	5000
917H(8)	HWS	W:C-H	1500

The behaviour of the HPC tools was regularly assessed by means of SEM. Additionally, at the end of their lives the microstructure beneath the cutting edge was evaluated by means of metallographic inspection of transverse specimens. Figures 2.5.17 and 2.5.18 describe the procedure to obtain these specimens both for punches and slitting tools. Punches of 1.2379A, 1.2379B and UNIVERSAL were studied by these means, as well as the slitting tools of 1.2379, UNIVERSAL and HWS.

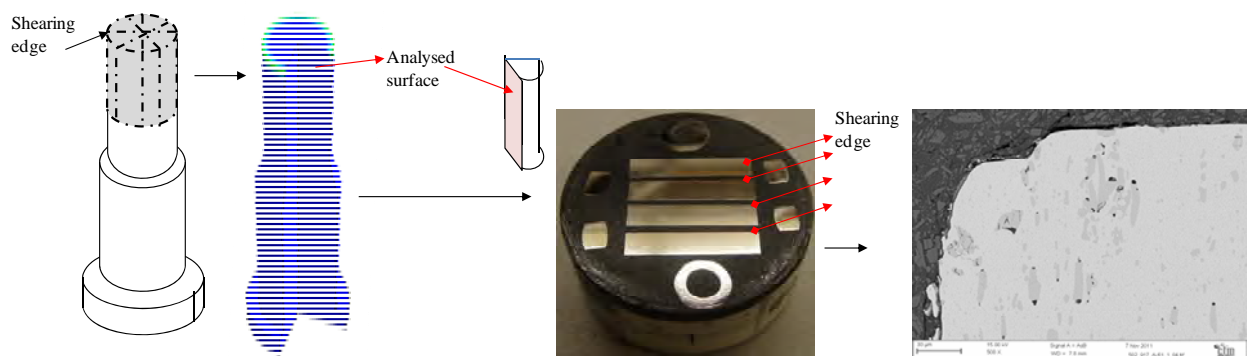


Figure 2.5.17 Transverse specimens of punches to analyse the microstructure beneath the cutting edge

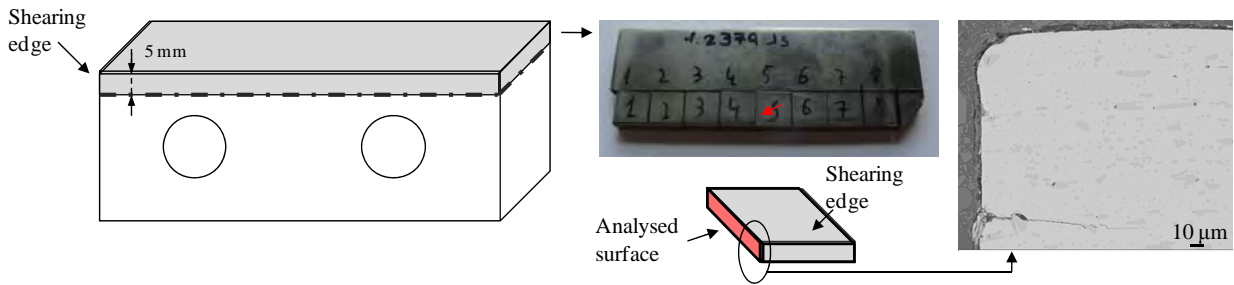


Figure 2.5.18 Transverse specimens of slitting tools to analyse the microstructure beneath the cutting edge

2.5.4 Instrumentation of tools: analysis of cutting loads and displacements

This work was performed in the frame of the stay 3 months long (Sept./Dec. 2010) at the Technische Universität München (TUM) in the Lehrstuhl für Umformtechnik und Gießereiwesen (UTG), nowadays led by Professor Wolfram Volk and at that time at the hands of Professor Hartmut Hoffmann. Both UTG and CTM cooperate together in the “Tailor Tool” project (2009-2012) funded by the European Commission via the 7th Frame European Research Program. The results which will be presented in this section are performed within the frame of the PhD Thesis of Katrin Nothhaft, and the Bachelor Thesis of Christoph Koebler. The author of the present Thesis participated in this work when it was being carried out during the stay at UTG.

A matrix for slitting press hardened flat 22MnB5 sheet steel was conceived, designed and built by UTG (Figure 2.5.19). The press, sensor equipment and test set-up can be observed in Figure 2.5.20 a). The matrix was equipped with exchangeable active elements and offered the opportunity to analyse the load in X and Z directions and the displacement of the upper tool with adjustable cutting clearances (Figure 2.5.20 b)).

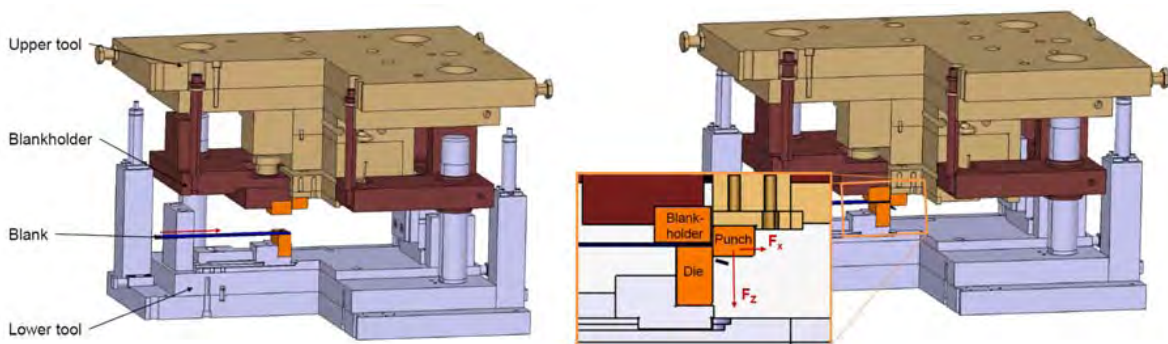


Figure 2.5.19 Schematic description of the matrix used for the cutting tests at UTG

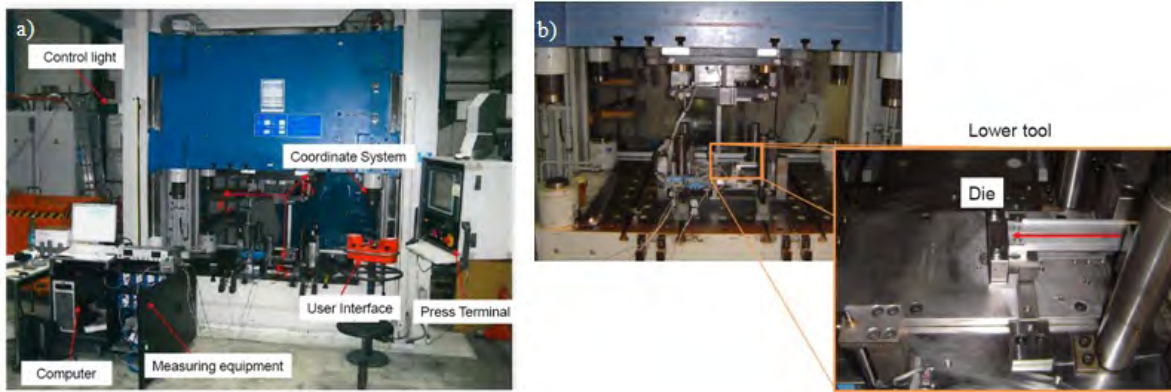


Figure 2.5.20 a) Test facility and sensors set-up; b) adjustable elements to vary the cutting clearance

22MnB5 sheets 1,5 mm thick had an Al-Si coating and were heat treated and quenched at GESTAMP HARDTECH. The tensile stress-strain curve of the totally hardened material can be observed in Figure 2.5.21 a). Cutting tests were run using different parameters (as shown in Figure 2.5.21 b)): clearances, CL , were 5, 10 and 15 % of the sheet thickness and four different punches were built with cutting angles, α , of 0, 2, 7 and 20 ° respectively. Tools were built with 1.2379 60 HRC and their cutting edge radius was rounded to 100 μm .

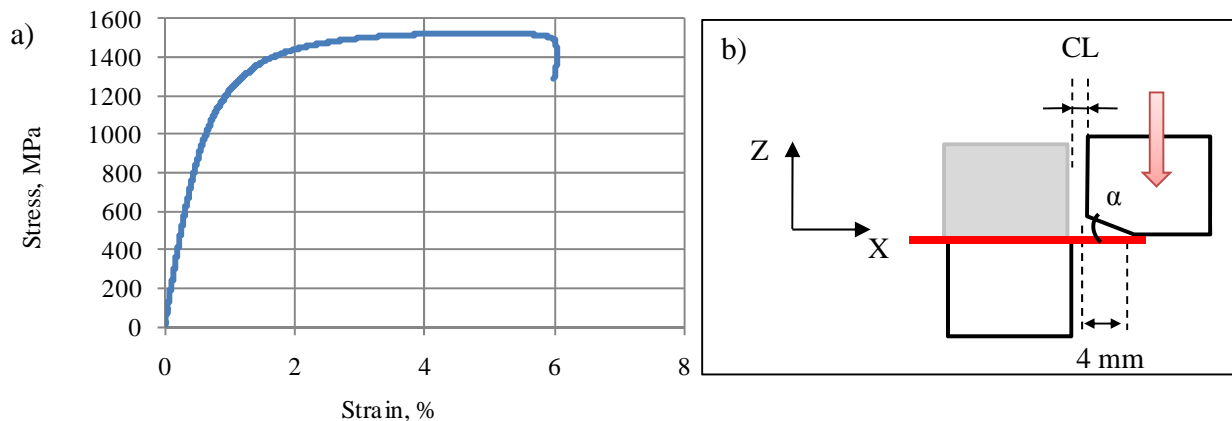


Figure 2.5.21 a) Tensile stress-strain curve of the 22MnB5 material used for the cutting tests; b) schema of the cutting parameters used in the tests

2.5.5 Influence of the shearing process parameters on the tool behaviour and part quality

The critical factor dictating tooling lives is the quality of the sheared parts. Tools are typically replaced when any defect such as burrs, large fracture zones and fracture angles, rollover, etc., are generated at the sheared edges of sheets. These defects may have detrimental effects on the ulterior mechanical behavior of the parts within vehicles. In this part of the Thesis the influence of the cutting parameters, i.e. clearance and tool radius, was analysed on account of both the effects on the mechanical response of tools and the morphology of sheet edges. To carry out these tests, the “Matriz de Tolerancia y Esfuerzos de Corte

(MTEC)” was built. The MTEC had exchangeable elements in order to study punching (MTEC-p, Figure 2.5.22 a)) or slitting processes (MTEC-s, Figure 2.5.22 b)).

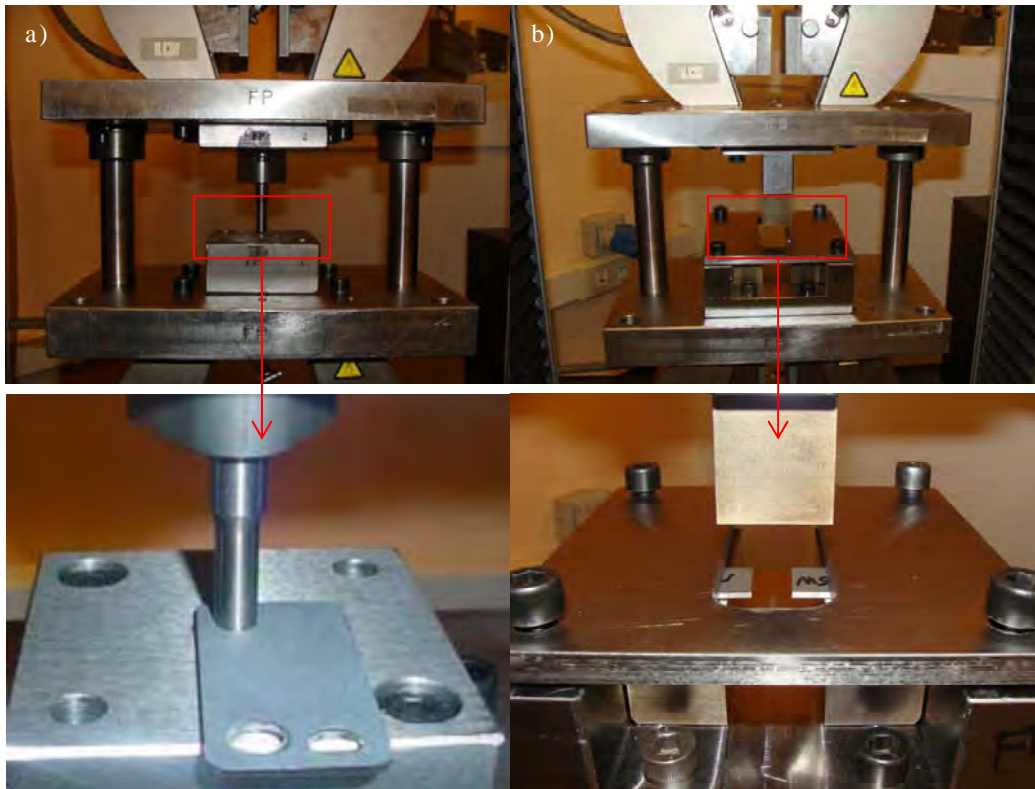


Figure 2.5.22 a) MTEC-p for punching tests; b) MTEC-s for slitting tests

Tests using clearances from 2,5 to 25 % were performed in the MTEC-p by means of dies with different diameters. Punches had the same geometry as those of the MDA and HPC. In the MTEC-s the clearance was adjusted by the relative movement of the lower tools. For each test the clearance was measured by thin gauges. Tools edge radii were varied from 10, 100 to 500 μm .

Shearing of DP1000 and MS-W1200 2 mm thick and press hardened BORON-02 1,8 mm thick was performed in the MTEC. The load-displacement curves corresponding to each test were registered and the maximum loads were determined for each combination of shearing parameters. The sheared specimens were prepared for metallographic inspection at LOM in order to evaluate the quality of the edges. Sample preparation consisted first in mounting the sheet in cold resin and then cutting very carefully the area aimed at being studied. The samples were finally ground, polished and etched with Nital in order to reveal their microstructure.

2.5.6 Stress distribution in cold forming and shearing tools

Computational analysis using FEM was performed to determine the stress distribution of the studied tools using the formulation of ABAQUS 6.8-1 commercial software. These results belong to the background of CTM in computer simulation and the tasks were carried out by Ricardo Hernández within the frame of his Doctoral Thesis (in course). The results obtained from computer simulations were used as driver to understand and rationalize the damaging mechanisms acting in tools, but purely developing FE-models was not a target of the present work.

Tools were modelled assuming linear elastic behaviour while the sheet was considered elasto-plastic. The blank holder's action was replaced by 200MPa constant pressure. Further information about the parameters set in the FE-model is summarized in Table 2.5.9.

2. Experimental procedure

Table 2.5.9 Summary of the system conditions and parameters used in the FE-simulations

Section	Type of operation	Sheet material; thickness	System dimension	ABAQUS formulation	Tool mat. properties E (GPa)	Sheet material properties σ_y / σ^R (MPa)	Boundary conditions	Contact method; friction coefficient	Size of elements
2.5.2.1	Trimming	22MnB5; 2mm	3D	Explicit	240	1150 / 1500	Displ. constraint at hole's clamping	Kinematic; 0,15	0,01 mm all surfaces
2.5.2.2	Punching	MS-W1200; 2 mm	3D	Explicit	210	800 / 1260	Displ. control at sheet and punch	Kinematic; 0,15	0,01 mm all surfaces
2.5.2.3	Drawing	TRIP800; 2 mm	2D (plane strain)	Implicit	210	450 / 680	Displ. constraint at blank holder and punch	Surface to surface; 0,1	0,1 mm all surfaces
2.5.2.3	Bending	DP1000; 2 mm				600 / 1119			
2.5.2.3	Punching	TRIP800; 2 mm DP1000; 2 mm	3D	Explicit	Rigid	450 / 680 600 / 1119	Displ. control at sheet and punch	Kinematic; 0,15	Tool edge 0,1 mm Sheet 0,05 mm
2.5.3	Punching	DP1000; 2 mm MS-W1200; 2 mm BORON-02; 1,8 mm	2D (axisymmetric)	Implicit	210	600 / 1119 800 / 1260 1150 / 1500	Displ. constraint at outer surface & displ. control up. part of the punch	Node to surface; 0,15	Tool edge $5 \cdot 10^{-4}$ mm Sheet $5 \cdot 10^{-5}$ mm
2.5.3	Slitting	DP1000; 2 mm MS-W1200; 2 mm BORON-02; 1,8 mm	2D (plane strain)	Implicit quasi-static	240	600 / 1119 800 / 1260 1150 / 1500	Displ. constraint at outer surface & displ. control up. part of the punch	Node to surface; 0,15	Tool edge $5 \cdot 10^{-3}$ mm Sheet $5 \cdot 10^{-4}$ mm